


Spring 5-15-2017

Nuclear Spin Alignment in Optically Pumped Semiconductors

Matthew M. Willmering
Washington University in St. Louis

Follow this and additional works at: https://openscholarship.wustl.edu/art_sci_etds

 Part of the [Optics Commons](#), and the [Physical Chemistry Commons](#)

Recommended Citation

Willmering, Matthew M., "Nuclear Spin Alignment in Optically Pumped Semiconductors" (2017). *Arts & Sciences Electronic Theses and Dissertations*. 1156.
https://openscholarship.wustl.edu/art_sci_etds/1156

This Dissertation is brought to you for free and open access by the Arts & Sciences at Washington University Open Scholarship. It has been accepted for inclusion in Arts & Sciences Electronic Theses and Dissertations by an authorized administrator of Washington University Open Scholarship. For more information, please contact digital@wumail.wustl.edu.

WASHINGTON UNIVERSITY IN ST. LOUIS

Department of Chemistry

Dissertation Examination Committee:

Sophia E. Hayes, Chair

Parag Banerjee

Alexander Barnes

Bryce Sadtler

Jacob Schaefer

Nuclear Spin Alignment in Optically Pumped Semiconductors

by

Matthew M. Willmering

A dissertation presented to
The Graduate School
of Washington University in
partial fulfillment of the
requirements for the degree
of Doctor of Philosophy

May 2017

Saint Louis, Missouri

copyright by
Matthew M. Willmering
2017

Table of Contents

List of Tables	v
List of Figures	vi
Acknowledgments	viii
Abstract	xiii
1 Introduction	1
2 Basic Concepts	4
2.1 Nuclear Magnetic Resonance	4
2.1.1 Spin Quantum Number	4
2.1.2 NMR Hamiltonian	5
2.1.3 Spin Precession and Detection	10
2.2 Semiconductors	12
2.2.1 Charge Carriers	12
2.2.2 Band Diagram	13
2.2.3 GaAs	14
2.2.4 CdTe	16
3 Theory of Optical Pumping in Semiconductors	18
3.1 History	18
3.1.1 Optical Pumping in General	18
3.1.2 Optical Pumping in Semiconductors	19
3.2 Spin Orientation and Polarization	20
3.2.1 Thermal Polarization	20
3.2.2 Non-equilibrium Polarization	22
3.3 Optical Pumping of Electrons	23
3.3.1 Excitation with Circularly Polarized Light	24
3.3.2 Electron Polarization	24
3.4 Nuclear Polarization	25
3.4.1 Hyperfine Interaction	26
3.4.2 OPNMR Profiles	27

4	NMR Hardware and Optical Equipment	29
4.1	Janis Horizontal Cryostat	29
4.2	Optical Equipment	32
4.3	Pre-existing NMR Hardware	34
4.4	Two-Channel Probe Design	35
4.4.1	Design of Probe Backbone	35
4.4.2	Electronic Circuit	40
4.4.3	Performance and Testing	42
	two-channel OPNMR Pulse Sequences	43
	Experimental	46
5	Magnetic Field Dependence of Light Hole Transition via OPNMR	49
5.1	Introduction	49
5.2	Experimental	52
5.2.1	OPNMR at NHMFL	54
5.2.2	OPNMR and Polarized PLE at WUSTL	55
5.2.3	Procedure	55
5.3	Results and Discussion	58
5.3.1	OPNMR Profiles as a Function of Magnetic Field	58
5.3.2	Light Hole Transition Field Dependence	61
5.4	Conclusions	65
6	Optically Pumped NMR of CdTe	67
6.1	Introduction	67
6.2	Experimental	68
6.2.1	CdTe Samples	68
6.2.2	Experimental Methods	68
6.3	Results and Discussion	70
6.3.1	Photoluminescence Measurements	70
6.3.2	Relaxation (T_1) and Optical Pumping Rates	72
6.3.3	OPNMR Profile Variability Between Samples	75
6.3.4	OPNMR Profile Asymmetries and Enhancements	77
6.4	Conclusions	79
7	Characterization of Isolated ^{113}Cd-^{125}Te Nuclear Spin Pairs in CdTe Using Optical Pumping	80
7.1	Introduction	80
7.2	Experimental	84
7.3	Results and Discussion	87
7.3.1	OPNMR Cross Polarization	87
7.3.2	OPNMR SEDOR Experiments	93
7.4	Conclusions	96

8	OPNMR Investigation of an Al₂O₃-GaAs Interface	98
8.1	Introduction	98
8.2	Experimental	100
8.2.1	Al ₂ O ₃ -GaAs Interface Sample	100
8.2.2	OPNMR Methods and Sequences	101
8.2.3	Thermal Strain	103
8.2.4	Strain Induced Quadrupolar Splitting	104
8.3	Results and Discussion	104
8.3.1	OPNMR Signal From a Buried Interface	104
	Coated and Uncoated Spectra Comparison	105
	Optical Excitation Wavelength Dependence on Interface Signal	110
	Laser Helicity Dependence	112
8.3.2	OPNMR Hyperpolarization at an Interface	112
	OPNMR Nutation Dependence	115
	Polarization Dependence on Multiple Parameters	117
8.4	Conclusions	122
9	CASTEP Calculations of NMR Parameters in Amorphous Alumina	123
9.1	Introduction	124
9.2	Experimental	126
9.2.1	Molecular Dynamic Simulations of Structures	126
9.2.2	CASTEP Simulations of NMR Parameters	127
9.2.3	Synthesis and NMR Acquisition of Al ₂ O ₃ Thin Films	128
9.3	Results and Discussion	129
9.3.1	Amorphous Structures of Aluminum Oxide	129
9.3.2	NMR Parameters of Amorphous Structures	132
9.3.3	Comparison of Calculated and Experimental NMR Lineshapes	134
9.4	Conclusions	140
10	Conclusions and Future Directions	142
10.1	Conclusions	142
10.2	Future Directions	143
Appendix A	2 Channel Probe Drawings	145
References		163
Vita		175

List of Tables

2.1	GaAs NMR parameters.	16
2.2	CdTe NMR parameters.	17
6.1	^{113}Cd T_1 relaxation time constants for CdTe samples at 6 K and 4.7 T.	73
6.2	^{113}Cd Optical pumping time constants for CdTe samples at 6 K and 4.7 T.	74
6.3	^{113}Cd OPNMR profile parameters for CdTe samples at 6 K and 4.7 T.	78
8.1	Satellite peak parameters acquired by deconvolution of interface signal.	109
9.1	CASTEP derived NMR parameters for amorphous alumina.	133

List of Figures

2.1	Basic vector model of NMR illustrating a 90° pulse.	11
2.2	Band diagram for a direct gap bulk semiconductor.	15
3.1	Atomic state approximation for direct gap GaAs and CdTe.	20
3.2	Sample OPNMR profile for si-GaAs.	28
4.1	Experimental setup for the combined OP/ODNMR apparatus.	30
4.2	Designs for the top cap and baffles of the two-channel probe.	37
4.3	Designs for the probe head of the two-channel probe.	38
4.4	The full two-channel probe.	39
4.5	two-channel probe circuit.	40
4.6	Basic two-channel OP sequences for probe testing.	45
4.7	two-channel probe decoupling test.	46
4.8	two-channel probe cross-polarization test.	47
5.1	Quantum well atomic-like state approximation.	51
5.2	Quantum well sample for light hole transition measurements.	53
5.3	Basic OPNMR Pulse sequence.	57
5.4	OPNMR profiles of GaAs quantum well as a function of magnetic field.	59
5.5	Light Hole transition field dependence.	62
5.6	Energy separation between $\sigma+$ and $\sigma-$ polarized light transitions for the light-hole transition.	64
5.7	Comparison between $\mathbf{k}\cdot\mathbf{p}$ perturbation theory calculations and experimental results for the light-hole transition.	66
6.1	Photoluminescence measurements of bulk CdTe samples.	71
6.2	OPNMR profiles of bulk CdTe samples.	76
7.1	OP-CP and SEDOR sequences for CdTe.	85
7.2	CdTe CP short contact time spectra	88
7.3	CdTe OP-CP NMR contact time contour plot.	89
7.4	^{113}Cd OP-CP NMR central peak as a function of contact time.	90
7.5	^{113}Cd OP-CP NMR satellite peaks as a function of contact time.	92
7.6	CdTe structure with important angles noted.	93
7.7	OP SEDOR data of ^{113}Cd - ^{125}Te spin pairs.	95

8.1	Sample and experimental configuration for optical pumping of the Al ₂ O ₃ -GaAs interface sample.	101
8.2	OPNMR sequence for observation of polarized interface.	102
8.3	Comparison between thermally polarized and optically pumped GaAs with and without Al ₂ O ₃ film.	106
8.4	⁷⁵ As OPNMR of the alumina-coated GaAs showing the deconvolution of spectrum using Gaussian peaks.	108
8.5	⁷⁵ As OPNMR spectra of Al ₂ O ₃ -GaAs interface sample at various wavelengths.	111
8.6	Laser helicity dependence of the interface signals in the Al ₂ O ₃ -GaAs interface sample.	113
8.7	Nutation of a hyperpolarized quadrupolar split interface signal.	116
8.8	Model for nutation of a hyperpolarized weakly-quadrupolar-split interface signal.	118
8.9	Polarization dependence of excitation wavelength of Al ₂ O ₃ -GaAs interface sample.	119
8.10	Local Polarization at interface as a function of optical pumping time.	121
9.1	NMR spectra of amorphous alumina.	129
9.2	Partial RDFs of alumina as a function of temperature from MD simulations.	130
9.3	Bond angle distributions in alumina as a function of temperature from MD simulations.	131
9.4	CASTEP calculated spectra for amorphous alumina.	135
9.5	Comparison between calculated and experimental spectra for amorphous alumina.	136
9.6	Comparison between Gaussian isotropic and extended Czjzek models for amorphous alumina.	138
9.7	Example unit cells for amorphous alumina.	140

Acknowledgments

While my graduate career is coming to an end, I must acknowledge all of those who have made this journey possible.

To begin, if it was not for support from my family and friends, this never would have been possible. Foremost, my parents have always supported me and pushed me to reach for the best I could be. Through their support and encouragement, I have been able to push my previously perceived boundaries, and will be able to continue to do so. In addition, the constant encouragement and support from my sister and Natalie have been crucial to make it this far. Not to mention, the understanding by Natalie, when it comes to the amount of work a graduate level program requires, was greatly appreciated since she never held any of my time commitments against me. As for the friends, many have shown interest in my work and have help supported me through these 5 years, especially Sean, Eric, and Adam.

As for the Washington University faculty, many have helped in numerous ways. First, I must thank the annual committee members of Drs. Hayes, Barnes and Schaefer. The committee meetings were always full of helpful and intriguing conversations related to my research and any difficulties I may have encountered. The help is greatly appreciated. In addition, I appreciate Drs. Sadtler and Banerjee for joining my defense committee and their future input on this dissertation.

Many of my projects included collaborations with others outside of my graduate research lab. Dr. Conradi helped in many ways by taking part in numerous science discussions and

assisting in the design and fabrication of the two-channel OPNMR probe. Dr. Loomis was always open to discussion when it came to semiconductor physics and had many valuable inputs when it came to my research. The research group of Dr. Stanton from the University of Florida was a large help with their calculations of semiconductor band structures and with input on the modeling of the light hole transition. Also from the University of Florida, the group of Dr. Bowers was instrumental in allowing me the opportunity to travel to the NHMFL, making many of the measurements for the light-hole chapter, and in obtaining time at the NHMFL. Speaking of the NHMFL, many of the researchers and lab space were crucial to our research, especially Drs. Reyes, Kuhns and McGill. For the use of their facilities and their expertise, I must thank the NHMFL in Tallahassee, FL. Thank you to Dr. Conley and Ms. Jenkins from Oregon State University for the alumina film preparation and deposition via ALD. Without the sample, much of my research would not have been able to be completed. Lastly, Drs. Persson and Aykol of Lawrence Berkeley National Laboratory were a large help for calculation of the amorphous structure of alumina thanks to their MD simulations. The computational discussions with them were always helpful, especially with their expertise in the field.

My graduate schooling was largely shaped by the fellow graduate students and postdoctoral associates in the Hayes lab with me. In particular, both Zayd and Erika were imperative to me coming up to speed on the OPNMR hardware, experiments, and theory. They greatly influenced and improved my abilities to be the scientist I am today. In addition, brief overlap with Dustin was useful for my understanding of the more in-depth theory governing the spin physics in OPNMR. More recently, the new graduate student on the project, Ike, has helped by providing stimulating discussions about my results and his future experiments. As for the other graduate students in the Hayes lab, I'm thankful for the many informative

discussions, ideas, and inputs from Katie, Andy, Jeremy, Blake, Robert, Chia-Hsin, Jinlei, Yvonne, Daphna, and Jason.

With the large overlap in the Hayes and Conradi labs, I must also thank and acknowledge the help of the students and postdoctoral associates in the Conradi lab. Sam, whom I've had the most interactions with, has provided valuable insight from the mind of a trained physicist, which is extremely helpful for experiments which overlap many disciplines. In addition, Eric and Hongyang have also been of help when discussing NMR. Coming from a school rich in NMR has also allowed me to interact with many other NMR groups on campus. Both the Schaefer and Barnes groups have provided a lot of insight into NMR and hyperpolarization methods from different perspectives, which is an amazing help when trying to understand and optimize my own experiments. Lastly, many other fellow graduate students from the chemistry department and other disciplines have provided input which has been very useful.

Of course, none of this would have been possible without Sophia. Coming in as an inorganic/material science focused student, I knew I wanted to work on solid state material projects. With the OPNMR project, a very small portion of the research was focused on studying semiconductors. This caused me some panic and uncertainty in my abilities to learn and perform research in the OPNMR field. However, with Sophia's help and support, I was able to prove to myself that I can expand to other fields and make an impact. While Sophia was always present for any questions I may have had, her "hands off" approach to mentoring allowed me to flourish in essence as an independent researcher, designing and completing my own experiments as I deemed important. In addition, Sophia has provided me with useful information and professional guidance in order to reach my goals.

On the technical side, without the Chemistry Department Machine Shop, my designs for the parts of the two-channel probe would have been nothing besides designs. Thanks to them, the fabrication and use of the two-channel probe was truly a huge success.

All of the above is only possible though thanks to Washington University in St. Louis, The Graduate School, and the Department of Chemistry. If it was not for them accepting me, giving me the chance to study, learn, and prove myself, none of this would have been possible. In addition, I would like to thank the Chemistry Department and The Graduate School for their support in allowing us to present our scientific findings to the community. Also, thankfully, I was awarded the Dean's Dissertation Fellowship, allowing me to focus on writing this dissertation and related publications. It allowed for a much easier and simpler wrapping up of my research projects and the subsequent transfer to the more recent graduate students.

Lastly, I must acknowledge the agencies which provided the financial support in order for me to research these projects. The main grant which supported my research was from the National Science Foundation, Division of Material Research, grant #1206447. The NHMFL is supported by the National Science Foundation Cooperative Agreement, Division of Material Research, #1157490. In addition, for the computational works, the National Science Foundation provided support via the Data Infrastructure Building Blocks, grant #1640899.

Matthew M. Willmering

Washington University in Saint Louis
May 2017

Dedicated to my parents, Mike and Ginny Willmering.
Without their constant help, support, and motivation,
I would not have been able to push my perceived limitations.

ABSTRACT OF THE DISSERTATION

Nuclear Spin Alignment in Optically Pumped Semiconductors

by

Matthew M. Willmering

Doctor of Philosophy in Inorganic Chemistry

Washington University in St. Louis, May 2017

Research Advisor: Professor Sophia E. Hayes

Nuclear magnetic resonance (NMR) has shown its ability to be a very informative analytical technique due to the ability to measure very small changes in the energy splittings due to the nuclei's local environment. However, this ability is hindered by the low sensitivity of the experiment. Many methods have been postulated and implemented to enhance the sensitivity of NMR experiments; one of which is optically pumped NMR (OPNMR). In this dissertation, the usefulness and potential applications of OPNMR are presented. First, a doubly resonant OPNMR probe was fabricated in order to complete more advanced NMR techniques while optically pumping the semiconductor sample. OPNMR was then shown to be very beneficial and accurate for measuring light hole transitions in semiconductors, which are typically difficult to observe using traditional techniques. The optical pumping behavior of a sample (CdTe) has been debated, but was measured here in order to obtain the expected trends and behavior. Discussion of the potential uses of optically oriented isolated spins pairs is presented and the characterization of such spin pairs is implemented, which included the first experimental report of a postulated NMR sequence (a version of

spin echo double resonance). An $\text{Al}_2\text{O}_3/\text{GaAs}$ interface was studied by OPNMR in order to observe the properties for the first time and the measured polarization was much higher than previously reported. Lastly, molecular dynamic and density functional theory calculations were used collaboratively to provide an accurate model for amorphous alumina.

Chapter 1

Introduction

Nuclear magnetic resonance (NMR) was discovered in 1938 by I. I. Rabi [1] and has since become one of the most commonly used analytical techniques. The technique is unique in that it provides nuclear isotope specific information on the atomic level. While NMR is most commonly performed on solution samples, solid-state NMR has seen many advancements which have led to the ability to determine chemical structures, bond distances, motion and many other molecular properties [2, 3]. However, the signal-to-noise ratio, especially for the typically broader solid-state NMR lineshapes (some more than 100 times broader than liquid-state spectra), has limited NMR to bulk samples with at least $\approx 10^{17}$ nuclear spins (i.e., magnetic moments).

The NMR signal-to-noise ratio is governed by the energy level splitting between nuclear spin states. Nuclear spin states are separated into different energy levels in a magnetic field based primarily on the Zeeman interaction. The populations of these states are dictated by Boltzmann statistics; because the energy splittings are small (typically 10–900 MHz), the population difference between the states (and thus the signal-to-noise ratio) is extremely small.

$$\uparrow/\downarrow = e^{(\gamma\hbar B_0/kT)} \quad (1.1)$$

describes the population ratio of two nuclear spin states (\uparrow and \downarrow) separated by the Zeeman interaction where γ is the magnetogyric ratio, B_0 is the applied external magnetic field, and T is the sample temperature [2]. The most common methods of increasing signal is with manipulation of the Boltzmann polarization by increasing the energy splitting (i.e., higher magnetic fields) and/or decreasing the sample temperature. The polarization of a spin- $\frac{1}{2}$ nuclei is defined as $P = \frac{\uparrow-\downarrow}{\uparrow+\downarrow}$, where \uparrow and \downarrow are the populations of the nuclear spins when they are aligned or counter-aligned with the magnetic field. However, these methods, which rely on a Boltzmann distribution, have not been able to achieve polarizations in the tens of percents yet, due to technological limitations.

Many other NMR based techniques have been developed to achieve nuclear spin polarization values much greater than the Boltzmann polarization, most of which take advantage of the electron spin states Zeeman splittings which are (typically) much larger than the nuclear spin state Zeeman splittings. One technique specifically is optically pumped NMR (OPNMR). OPNMR, which has been implemented in many different nuclear spin systems, relies on laser excitation of electron states. By taking advantage of the optical selection rules, extremely high polarizations of the electrons can be achieved on the nuclei through the hyperfine interaction, allowing for faster NMR detection or detection of fewer nuclear spins (due to less signal averaging needed and faster growth of the polarization). Optical pumping has typically been implemented on noble gases and semiconductors [4]. The focus here is on the optical pumping of electronic states in semiconductors.

OPNMR in semiconductors has been investigated thoroughly since its first discovery in 1968 by George Lampel [4, 5, 6, 7, 8, 9, 10, 11, 12, 13, 14, 15, 16, 17, 18, 19, 20, 21, 22]. Recently, our lab has focused on attempting to understand the spin physics underlying OPNMR phenomena by applying the technique to samples which have not yet been studied

by OPNMR. This dissertation will cover the design and fabrication of the two channel OPNMR probe used for most of the research presented here. In addition, OPNMR studies on a GaAs quantum well, a variety of CdTe samples, and an Al₂O₃-GaAs interface will be presented and discussed. Lastly, calculations of the NMR parameters for amorphous Al₂O₃ were completed with potential to be used in future OPNMR studies.

Chapter 2

Basic Concepts

2.1 Nuclear Magnetic Resonance

Nuclear magnetic resonance (NMR) uses magnetic fields to split degenerate nuclear energy states into two or more energy levels for nuclear isotopes that have a magnetic moment. The z -component of the spin states align either parallel or anti-parallel with an external magnetic field and are then manipulated via radio-frequency (RF) pulses. The resulting signal contains chemical and physical information about the observed nuclear spin. A brief overview of the theory of NMR will be covered in this section but for a more in depth review in NMR, please refer to books by C. P. Slichter and others [2, 3].

2.1.1 Spin Quantum Number

As mentioned, NMR requires the nuclear isotopes of interest to have a magnetic moment. This magnetic moment, or spin, determines how the nuclear energy levels interact with magnetic fields via the Zeeman interaction. Nuclei with spin have a non-zero spin quantum

number, I (which determines the number of nuclear spin states). For a nuclei with spin I , there will be $(2I+1)$ energy levels in a magnetic field; $m_I = -I, -I+1, \dots, I-1, I$. Each of the m_I spin states have a different energy, where

$$E_{m_I} = -m_I \hbar \gamma B_0 \quad (2.1)$$

is the energy of the m_I spin state due to the Zeeman interaction which depends on the magnetogyric factor (γ) and the external magnetic field (B_0). γ is a constant value which is nuclear isotope specific. The separation of spin state energy levels due to the (typically) dominant Zeeman interaction is determined by

$$\Delta E = \hbar \gamma B_0 \quad (2.2)$$

for the allowed single quantum transitions (i.e., $\Delta m_I = \pm 1$). NMR is able to probe these energy splittings using RF pulses. Note that quadrupolar nuclei ($I > 1/2$), will have multiple allowed transitions, but will all be at the same energy, if only the Zeeman interaction is considered.

2.1.2 NMR Hamiltonian

If only the Zeeman interaction were considered, we would observe one peak per nuclear isotope, making it difficult to obtain information about the chemical compound. However, there are many other interactions perturbing the Zeeman interaction which allow the extraction of more chemical and physical properties. The total NMR Hamiltonian ($\hat{\mathcal{H}}_{NMR}$) is the sum of multiple, interaction-specific Hamiltonians which shift and sometimes even further split the nuclear spin energy levels and thus, change the allowed transition energies. The full nuclear

OPNMR Hamiltonian can be described by

$$\hat{\mathcal{H}}_{NMR} = \hat{\mathcal{H}}_Z + \hat{\mathcal{H}}_D + \hat{\mathcal{H}}_{CS} + \hat{\mathcal{H}}_J + \hat{\mathcal{H}}_Q + \hat{\mathcal{H}}_{HF} + \hat{\mathcal{H}}_{RF}. \quad (2.3)$$

The first term in the full OPNMR Hamiltonian, $\hat{\mathcal{H}}_Z$, is the Zeeman interaction responsible for breaking the degeneracy of the nuclear energy states, as discussed above. It is typically the dominant interaction present and thus determines the precession frequency, known as the Larmor frequency. The Zeeman Hamiltonian is [3]

$$\hat{\mathcal{H}}_Z = -\gamma\hbar B_0 \hat{I}_Z, \quad (2.4)$$

where \hat{I}_Z is the spin operator in the z -direction. The energy resulting from the Zeeman interactions is thus the same as shown in equation 2.1.

The dipolar Hamiltonian ($\hat{\mathcal{H}}_D$) describes the through space magnetic interaction between two nuclei. When the nuclei are different isotopes, they are denoted I and S . The heteronuclear ($I \cdot S$) dipolar interaction Hamiltonian is given by [2],

$$\hat{\mathcal{H}}_D = \frac{\gamma_I \gamma_S \hbar^2}{r^3} (1 - 3 \cos^2 \theta) \hat{I}_Z \hat{S}_Z \quad (2.5)$$

to first order, where r is the distance between the two nuclei, γ_I and γ_S are the magnetogyric ratios for isotope I and S (respectively), θ is the orientation of the internuclear axis with respect to the magnetic field, and I_Z and S_Z are the spin operator in the z -direction for each isotope. The strength of the dipolar coupling interaction in rad/sec is [23]

$$\omega_D(\theta) = \pm \frac{\gamma_I \gamma_S \hbar}{2r^3} (3 \cos^2 \theta - 1). \quad (2.6)$$

For the experiments presented here, heteronuclear dipolar coupling will be much stronger than homonuclear coupling because in our samples, where there are two types of atoms, the atoms of one type are surrounded by atoms of the other type. Thus the $1/r^3$ dependence greatly decreases the strength of the homonuclear dipolar interactions. In the samples studied by OPNMR here, the heteronuclear dipolar interaction causes a splitting of the energy levels, and because this interaction is usually the dominant mechanism, the broadening of the NMR spectra is typically governed by this interaction.

The third term in equation 2.3, $\hat{\mathcal{H}}_{CS}$, describes the chemical shift interaction. A common way to think about chemical shifts is by the amount of magnetic shielding the electrons surrounding the nucleus provide based on the molecular surroundings. The shielding due to the electrons, σ , is a second rank tensor (designated by the use of two bars) and thus leads to an orientation dependence of the chemical shift interaction with respect to the external magnetic field. The new effective external magnetic field experienced by the nucleus is [2]

$$\overline{B_{eff}} = \overline{B_0} - \overline{\overline{\sigma}}\overline{B_0}. \quad (2.7)$$

The shielding will have an isotropic and anisotropic portion. If $\sigma_{xx} = \sigma_{yy} = \sigma_{zz}$ as found in the cubic crystals studied here by OPNMR, the chemical shift anisotropy is zero. The isotropic portion of the shielding determines the shift in resonance frequency. In OPNMR, the NMR spectra are typically not referenced since the structure and chemical shifts of the samples are already well known and are comprised of a single nuclear site.

Similarly, the fourth term, $\hat{\mathcal{H}}_J$, is a second rank tensor and describes the J- (or indirect) coupling between two nuclear spins. This coupling mechanism occurs through the bonding electron spins between two nuclei rather than directly through space [2]. The J-coupling

contains an isotropic and an anisotropic component [24]. The anisotropic portion (also known as the pseudo-dipolar interaction) has an identical $(1 - 3 \cos^2 \theta)$ angle dependence to the dipolar interaction, making it difficult to distinguish between these two interactions, which lead to line splittings. The change in the nuclear spin state energies due to the J interactions is [25]

$$\Delta E = \left[\frac{1}{3} \left(2\bar{J}_\perp + \bar{J}_\parallel \right) - \frac{1}{3} \left(\bar{J}_\parallel - \bar{J}_\perp \right) \left(1 - 3 \cos^2 \theta \right) \right] m_S \hbar \quad (2.8)$$

where m_S is the spin state of the J-coupled nuclei, J_\parallel is the J interaction strength along the bond, and J_\perp is the J interaction strength perpendicular to the bond. This results in a splitting of the lineshape that is resolvable if the J-coupling is relatively strong compared to the other non-Zeeman interactions, which is typically only the case in solution NMR. J-coupling has proven to be important in one of the systems studied here, and thus will be discussed with and without optical pumping in chapters 6 and 7.

The fifth term in equation 2.3, $\hat{\mathcal{H}}_Q$, corresponds to the quadrupolar interaction for nuclei with spin $I > 1/2$. A nuclear quadrupole moment interacts with an electric field gradient (EFG) according to [26]

$$\hat{\mathcal{H}}_Q = \frac{1}{3} \omega_Q \{ 3\hat{I}_Z^2 - I(I+1) \} \quad (2.9)$$

$$\omega_Q = \frac{3}{4} \frac{e^2 q Q}{2I(2I-1)\hbar} (3 \cos^2 \beta - 1 + \eta \sin^2 \beta \cos 2\alpha) \quad (2.10)$$

to first order, where ω_Q is the quadrupolar coupling frequency where eQ is the nuclear specific electric quadrupole moment; $eq = V_{ZZ}$, the largest component of the EFG; η is the asymmetry of the EFG; and β and α are angles describing the orientation of the EFG with respect to the magnetic field. For the zincblende structures studied here, $V_{XX} = V_{YY} = V_{ZZ} = 0$ for the perfectly symmetric zincblende unit cell. However, any perturbations to the

cubic crystal structure will result in a non-spherical EFG and thus a non-zero quadrupolar interaction as discussed in Chapter 8.

$\hat{\mathcal{H}}_{HF}$, the hyperfine interaction, describes the coupling between unpaired electron spins and nuclear spins. In a perfect semiconductor, all electrons are spin paired, resulting in no hyperfine interactions. However, when the semiconductor is illuminated with laser light, an unpaired electron is created in an excited state from which it can couple to nuclei through the hyperfine interaction. The hyperfine interaction is composed of two parts, a Fermi contact portion and a through-space dipolar portion. The full Hamiltonian is [12]

$$\hat{\mathcal{H}}_{HF} = \left[-\frac{8\pi}{3}\hbar^2\nu_0\gamma_I\gamma_S|\psi(r)|^2\bar{\mathbf{I}}\cdot\bar{\mathbf{S}} \right] + \frac{\mu_0\gamma_I\gamma_S\hbar^2}{4\pi r^3} \left[\frac{3(\bar{\mathbf{I}}\cdot\bar{\mathbf{r}})(\bar{\mathbf{S}}\cdot\bar{\mathbf{r}})}{r^2} - \bar{\mathbf{I}}\cdot\bar{\mathbf{S}} \right]. \quad (2.11)$$

The first portion of the equation describes the Fermi contact interaction which depends on the unit cell volume (ν_0) and most importantly, the expectation value of the electron wave function at the nuclear site ($|\psi(r)|^2$). The second portion of equation 2.11 is the dipolar term and is similar to that described in equation 2.5. The Fermi-contact hyperfine interaction is believed to be the dominant interaction for excited electrons in s-orbital-type states while the dipolar hyperfine interaction is believed to be the dominant mechanism for non-s-type states [5].

The last interaction in the NMR Hamiltonian is one of the most important since it describes how the nuclear spins interact with applied RF pulses ($\hat{\mathcal{H}}_{RF}$). NMR utilizes RF pulses to perturb the nuclear spin system and acquire the NMR signal. The RF Hamiltonian is [2]

$$\hat{\mathcal{H}}_{RF} = -\gamma_I\hbar B_1 e^{-i\omega_z t \hat{I}_z} \hat{I}_X e^{i\omega_z t \hat{I}_z}. \quad (2.12)$$

The strength of the magnetic field, B_1 , from the RF pulse will cause the nuclear spins to precess about the direction of B_1 for duration t at a precession frequency of ω_Z . This is typically done on resonance ($\Delta E = \hbar\omega_{RF}$) to the energy splitting by sending RF pulses through a wire coil surrounding the sample.

2.1.3 Spin Precession and Detection

According to the vector model of NMR, the magnetic moment vector will rotate about the effective magnetic field vector it experiences, keeping a constant angle between the two [3]. At equilibrium, the individual magnetic moments sum to create a bulk magnetization (dependent on the number of nuclei and the polarization of the spins), which aligns with the external magnetic field vector, B_0 , defined along the z -axis as shown in Figure 2.1. Typically, strong (with respect to the non-Zeeman interactions) B_1 pulses are applied perpendicular to the magnetic moment in order to rotate the nuclear spin in a single plane (the xy -plane); these pulses are known as 90° pulses. After excitation, when the spins are in the xy -plane, pulses may be applied along the magnetic moment in order to hold the magnetic moment in place and thus not precess about weaker fields (known as spin-locking). The applied RF pulses result in precession of the magnetic moment at a frequency (in Hz) relative to the effective magnetic field applied, B_{eff} according to [3]

$$\nu_0 = -\frac{\gamma B_{eff}}{2\pi}, \quad (2.13)$$

where B_{eff} can be dominated by B_0 (in the z -direction) or B_1 (xy -plane). The typical NMR experiment uses an RF pulse resonant with the precession frequency due to B_0 (i.e., Larmor frequency) to cancel B_0 and create a large B_{eff} in the xy -plane. B_{eff} will then be in the

xy -plane and rotate the spin during the pulse length, typically until the bulk magnetization is rotated 90° into the xy -plane.

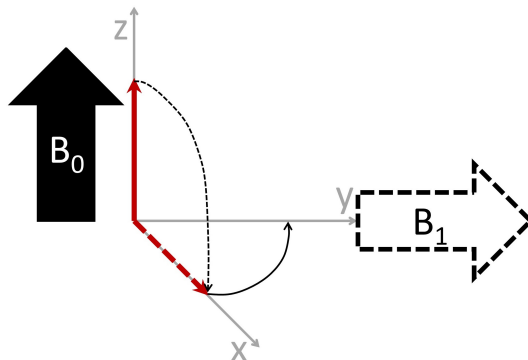


Figure 2.1: Basic vector model of NMR illustrating a 90° pulse after reaching equilibrium. The solid red arrow on the z -axis represents the bulk magnetization at equilibrium. When an on resonance pulse is applied, the spin precesses about B_1 at a constant angle, following the thin dashed arrow to the dashed red arrow on the x -axis. After the B_1 pulse has stopped, the spins will then precess about B_0 .

Once the spins are in the xy -plane, the RF pulse is typically stopped (B_1 is removed) and B_0 again becomes the dominant magnetic field. The spin will then precess about B_0 at its characteristic frequency (typically tens to hundreds of MHz, depending on the nuclear isotope and the magnetic field strength given by the Hamiltonian in equation 2.3). The precession of the magnetic moments in the sample induces a current in the coil surrounding the sample which is then detected by a spectrometer as a function of time resulting in a signal known as the free induction decay (FID). The spectrometer mixes the frequency of the pulse from the FID (in a simplified manner), indicating an on-resonance signal will have a frequency of 0 Hz. The FID is then Fourier transformed into the frequency domain resulting in the typical observed NMR spectra.

2.2 Semiconductors

Semiconductors are materials which lie between conductors and insulators in terms of their ability to conduct electricity. A materials ability to conduct electricity is dependent on the structure of the electron energy levels in the sample. An isolated atom has the well known $1s, 2s, 2p, 3s, \dots$ electron energy levels. However, when atoms are brought into close proximity with each other, the well-known energy levels are split due to the Pauli exclusion principle [27]. When multiple atoms are brought close to each other as in a crystal, the isolated atomic levels are split/broadened into a continuum of electron energy levels, known as energy bands. The electrons fill in the energy bands from lowest energy to highest energy similar to the case of isolated atoms. For semiconductors, this results in a highest occupied electron energy band (similar to the HOMO in molecular orbital theory) and a lowest unoccupied electron energy band (similar to the LUMO) which are separated by $\approx \leq 4 \text{ eV}$, known as a band gap [27]. The filled band is known as the valence band and the unfilled band is known as the conduction band. For insulators, the band gap is larger while in metals (conductors), the conduction band is partially filled.

2.2.1 Charge Carriers

In order to conduct electricity, charge must be able to be moved by particles known as charge carriers. The most well known charge carrier, the electron, has already been discussed above; however, there is another charge carrier present in semiconductors known as a hole. A hole is simply a lack of an electron where an electron should exist if the semiconductor were in its lowest energy state. Holes act similarly to electrons and both can move throughout the crystal lattice of the semiconductor. The main difference is a hole has a positive charge rather

than the negative charge of the electron. Electrons and holes play an important role when it comes to semiconductor devices as well as in the theory of optical pumping as discussed in Chapter 3.

Since excitation of electrons has been mentioned previously, it is important to note that a hole will be created when an electron is excited to a higher energy band. The electron and hole will remain in the same area of the crystal, coulombically bound to each other as an exciton, unless additional energy or potentials are applied. Many semiconductor devices apply voltages to separate the electron and hole and move them through the crystal. In addition, “hot” electrons (electrons excited with energy greater than the band gap) can be created. These “hot” electrons also have momentum, which needs to be considered for OPNMR research. How these charge carriers move through the crystal is described by electron energy band diagrams.

2.2.2 Band Diagram

Solid-state physicists have developed the $k \cdot p$ theory to describe energy bands, excitations, and momentum of the charge carriers as a function of crystal direction. In order to do so, the Hamiltonian which includes kinetic energy of the charge carriers, a local periodic crystal potential, and a spin-orbit interaction must be taken into account [28]. The simplest calculations are completed in k -space (reciprocal space) using wavevectors to derive the energy of a single band [28]:

$$E_n(k) = E_n(0) - \frac{\hbar^2 k^2}{2m_{eff}}, \quad (2.14)$$

where $E_n(0)$ is the original energy of band, k is the wavevector, and m_{eff} is the effective mass of the charge carrier. The band energy as a function of k thus forms a parabola which

depends on the original energy of the band. The curvature of the band is determined by the effective mass of the charge carrier present in that energy band.

In reality, there are multiple energy bands rather than a single band. The bands typically of interest are known as the split-off hole band, light-hole band, heavy-hole band, and conduction band (see Figure 2.2). For the direct-gap semiconductors studied in this dissertation, all four bands are aligned in k -space at $k = 0$, also known as the Γ -point of the Brillouin zone in k -space as shown in Figure 2.2. The valence bands are separated from the conduction band by the band gap energy and the split-off-hole band is separated from the degenerate heavy-hole and light-hole bands by the split-off energy. Also, since the light holes have a smaller effective mass than the heavy holes (due to the spin orbit interactions of the different energy states), there is a much larger curvature for the light-holes as a function of k . Excitations of electrons from the valence band into the conduction band away from $k = 0$ must be from equal but opposite values of k due to the conservation of momentum (i.e., the “hot” electron and “hot” hole must have equal amounts of momentum but in opposite directions).

2.2.3 GaAs

In this work, two semiconductors were studied via OPNMR; the first being GaAs. It is known as a III-V semiconductor due to its composition of column III and column V atoms in the periodic table. GaAs has a cubic zincblende crystal structure with a lattice constant of 5.65 \AA and a bond length of 2.45 \AA . The zincblende structure places both Ga and As in tetrahedral geometries ($\approx 109.5^\circ$ bond angles), bonded to four of the opposite nuclei.

GaAs is a direct gap semiconductor. At room temperature (300 K), the band gap is 1.42 eV but increases to 1.52 eV at the temperatures discussed in this work ($\approx 6 \text{ K}$) [29]. Split-off

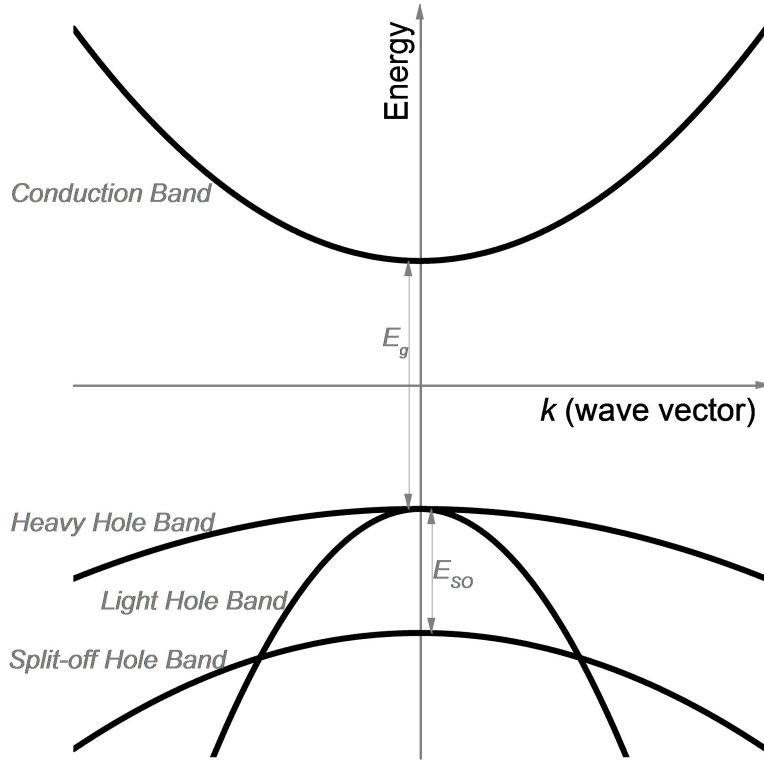


Figure 2.2: Band diagram for a direct gap bulk semiconductor. E_g is the band-gap energy and E_{SO} is the split-off energy.

energy (E_{SO}) is typically ignored for OPNMR experiments due to the much larger photon energies required to excite from the split-off band (0.34 eV additional energy [30]).

To observe the semiconductors and understand the spin physics governing the optical pumping, the NMR parameters for the isotopes to be studied via NMR will be necessary. The parameters of interest can be seen in Table 2.1. Notice that 100% of Ga and As nuclei have magnetic moments and are thus NMR active. They are also all quadrupolar nuclei, with ^{75}As coupling the strongest to electric field gradients. All the magnetogyric ratios in GaAs are positive; the largest being ^{71}Ga .

Table 2.1: GaAs NMR parameters.

Isotope	Spin I	Abundance (%)	Magnetogyric Ratio, γ ($\times 10^{-7}$ rad/(T s))	Quadrupole Moment, Q ($\times 10^{28}$ /m ²)
⁶⁹ Ga	$3/2$	60.4	6.4389	0.17
⁷¹ Ga	$3/2$	39.6	8.1812	0.11
⁷⁵ As	$3/2$	100	4.5961	0.29

2.2.4 CdTe

The second semiconductor studied via OPNMR was CdTe. It is composed of column II and column VI atoms and thus is a II-VI semiconductor. Thus, the bonds in CdTe are more ionic than those in GaAs. CdTe also has a cubic zincblende crystal structure with a lattice constant of 6.48 Å and a bond length of 2.81 Å. Identical to GaAs, the zincblende structure places each Cd and Te nuclei in a tetrahedral bonding geometry with four of the opposite nuclei.

CdTe is also a direct gap semiconductor. At room temperature (300 K), the band gap is 1.51 eV and increases to 1.60 eV at our temperatures [29]. The split-off energy (E_{SO}) for CdTe is 0.93 eV [30].

The NMR parameters of interest in CdTe can be seen in Table 2.2. Notice the small percentage of nuclei with a spin. Less than 25% of Cd and 8% of Te nuclei are NMR active. They are also all spin- $1/2$ nuclei and thus do not have a quadrupolar moment. In contrast to GaAs, all the magnetogyric ratios in CdTe are negative; indicating alignment with the field in the opposite direction when compared to GaAs.

Table 2.2: CdTe NMR parameters.

Isotope	Spin I	Abundance (%)	Magnetogyric Ratio, γ ($\times 10^{-7}$ rad/(T s))	Quadrupole Moment, Q ($\times 10^{28}$ /m ²)
¹¹¹ Cd	1/2	12.6	-5.7046	—
¹¹³ Cd	1/2	12.3	-5.9609	—
¹²³ Te	1/2	0.87	-7.0576	—
¹²⁵ Te	1/2	6.99	-8.5087	—

Chapter 3

Theory of Optical Pumping in Semiconductors

With a general understanding of both NMR and semiconductors, we can now discuss the theory behind the optical pumping of semiconductors. This theory will cover historical experiments, polarization, optical pumping to create hyperpolarized electrons, and finally the transfer of polarization to nuclei.

3.1 History

3.1.1 Optical Pumping in General

Optical pumping (OP) was first defined in 1950 by A. Kastler in reference to production of non-equilibrium populations (with respect to thermal equilibrium) in atomic states [31]. The definition originated for the atomic absorption of circularly polarized light where the angular momentum of a photon is encoded into the excited electron. Since then, optical

pumping has expanded to encompass semiconductors and other samples. The findings from Kastler, that polarized light allows selective excitation in Zeeman states, resulted in a Nobel Prize in physics in 1966 [4]. Optical pumping research began to expand into two major categories (noble gases and semiconductors), once G. Lampel showed the ability to use circularly polarized light to create non-Boltzmann populations in silicon in 1968 [32].

3.1.2 Optical Pumping in Semiconductors

Since the first OP experiment on semiconductors, performed by Lampel, further work has been done to understand the theory and apply it to semiconductors other than silicon. OPNMR has since been studied on GaAs, GaAs quantum wells, InP, CdS, and CdTe [12]. While semiconductor electron energies are described by bands, two approaches have been used to understand the optical pumping physics using atomic-like states near the Γ -point ($k=0$). The first approach uses excitation into impurity centers due to dopants and other defects which would capture the spin-oriented electrons in atomic-like states [33]. However, this method requires an understanding of the defect state(s) and its energy level(s) with respect to the energy bands. The second approach, which is the focus of this dissertation, assumes the optical excitation from valence to conduction bands will occur close to the Γ -point where the bands can be modeled as atom-like states [31]. The results from this assumption can be seen in Figure 3.1.

By exciting selective transitions and with different transition probabilities, electron spin polarizations well above the Boltzmann equilibrium can be established. The theory leading to the polarization will be discussed in Section 3.3.

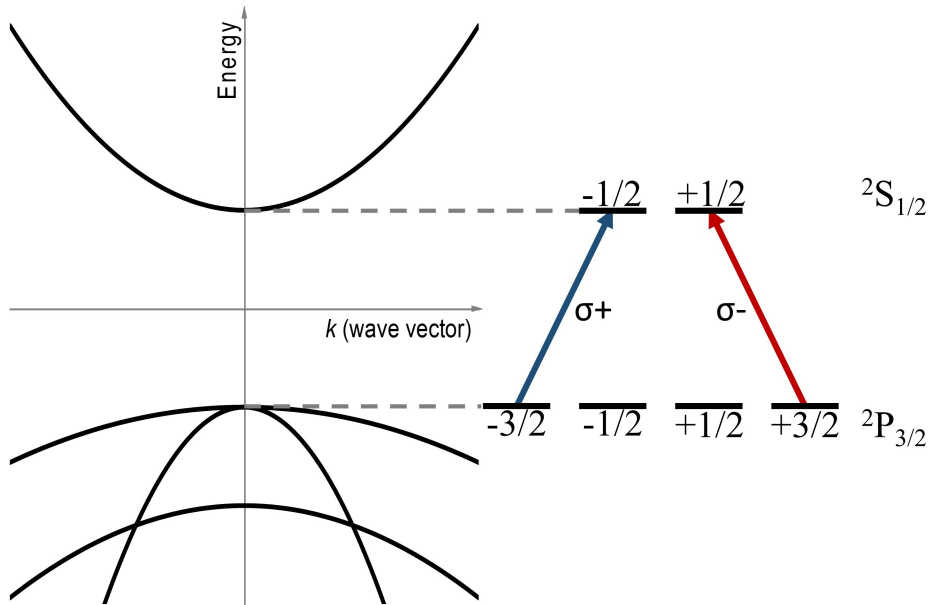


Figure 3.1: Atomic state approximation for direct gap GaAs and CdTe. At $k=0$ of the band diagram, the conduction band states are approximated as $^2S_{1/2}$ states and the degenerate valence band as $^2P_{3/2}$ states. The blue and red arrow illustrate the $\Delta m_j = \pm 1$ selection rule of σ (circularly) polarized light.

3.2 Spin Orientation and Polarization

Spin polarization is a description of the orientation of the magnetic moments, and thus populations of the spin states, with respect to the magnetic field. In order to comprehend the effect of the optical pumping, an understanding of the unperturbed system must be established first.

3.2.1 Thermal Polarization

The term “thermal” polarization refers to the nuclear or electron spin polarization matching Boltzmann statistics at the experimental temperature. At thermal equilibrium (for both

electron and nuclear spins), the resulting spin state populations are described by [2]

$$\frac{N_\beta}{N_\alpha} = e^{-\gamma\hbar B_0/kT}, \quad (3.1)$$

where N_β and N_α refer to the number of spins in the higher and lower Zeeman spin states (following the allowed $\Delta m_s = \pm 1$ between spin states). The populations of the spin states are thus modeled by an exponential with more spins in the lower energy spin state(s). Other interactions in the full OPNMR Hamiltonian (Equation 2.3) are very small compared to the Zeeman interaction, resulting in negligible changes in the spin state populations with their inclusion.

Since the Zeeman energy splitting is small in NMR experiments (300 MHz=1.24 μeV), kT of the system will need to be similar in order to reach high polarizations. However, at $T = 6$ K for the experiments presented here (≈ 60 MHz=0.25 μeV), kT is still 517 μeV . This equates to the lower energy state having 1.000 48 times the population of the higher energy state (4.8 more spins for every 10,000 spins). The small difference in populations is ultimately one of the biggest factors limiting the sensitivity of NMR.

In order to make the population differences a single comparable value, polarization must be defined. Since high polarizations can be achieved via OPNMR, we can not use the standard “high-temperature approximation” to describe polarization. (The “high-temperature” approximation assumes a linear distribution for the populations of spin states). Instead, polarization for a Zeeman dominated interaction will be [34]

$$P = B_I \left(\frac{\hbar\omega_0}{kT} \right), \quad (3.2)$$

where B_I is the Brillouin function for spin I . For spin $1/2$ electrons and nuclei, $B_{1/2} = \tanh x/2$ which leads to

$$P = \tanh\left(\frac{\hbar\omega_0}{2kT}\right). \quad (3.3)$$

For the example given above ($T = 6$ K and $\omega_0 \approx 2\pi 60$ MHz), the nuclear polarization would be 0.024 % in a spin- $1/2$ system.

3.2.2 Non-equilibrium Polarization

Nuclear and electron spin polarizations can be perturbed to non-equilibrium distributions. This deviation from equilibrium can be after any perturbation to the spin system such as an RF pulse or optical pumping. The spin systems will then approach the thermal equilibrium with a time constant of T_1 , known as the spin-lattice relaxation time. No matter the initial polarization, the z-magnetization (proportional to polarization and number of nuclei) will recover to equilibrium according to [3]:

$$M_Z(t) = [M_Z(0) - M_Z^0]e^{-t/T_1} + M_Z^0. \quad (3.4)$$

In this equation, $M_Z(0)$ is the initial magnetization immediately after perturbing the spin system and M_Z^0 is the equilibrium magnetization.

For spin- $1/2$ particles, polarization can be defined as [12]

$$P = \frac{\uparrow - \downarrow}{\uparrow + \downarrow} \quad (3.5)$$

where \uparrow and \downarrow describe the number of spins with such an orientation with respect to the magnetic field. While Equation 3.5 is convenient, it becomes impossible to use on spins with

$I > 1/2$ due the presence of more than two possible spin states. Instead, one approach is to assume the populations of the $2I+1$ energy levels are still described by an exponential with a nuclear spin temperature, T_N , different than that of the sample [35]. T_N can then be used to describe polarization by substituting for T in Equation 3.2. It is important to realize this approach only describes the average spin polarization of the observed nuclei and fails if the spin state populations cannot be approximated by an exponential.

3.3 Optical Pumping of Electrons

In optical pumping, electrons are the source of hyperpolarization (polarization above that of thermal polarization). Thus, understanding the origin of the electron polarization is essential to understand the resulting nuclear polarization. Basic theory assumes the semiconductor electron energy bands are atomic-like states at $k=0$ as shown in Figure 3.1. Thus, for the samples studied here, the valence band is comprised of $m_J=\pm 3/2$ and $\pm 1/2$ states, while the conduction band is comprised of $m_J = m_S = \pm 1/2$ states. Excitation with unpolarized (or linearly polarized, $\Delta m_j = \pm 0$) laser light between these states will result in equal populations of spin up and spin down conduction electrons. When the populations are equal, known as saturation (no bulk magnetization) of the unpaired electrons, it can result in nuclear spin polarization enhancement via the optical Overhauser effect [6, 31, 32], where the maximum nuclear polarization enhancement is proportional to γ_e/γ_N .

3.3.1 Excitation with Circularly Polarized Light

While unpolarized light and linearly polarized light result in enhanced signal, the use of circularly polarized light can achieve higher electron polarizations by taking advantage of selection rules and transition intensities. Circularly polarized light, $\sigma+$ and $\sigma-$, carry plus or minus one unit of angular momentum, respectively. The carried momentum impart selection rules of $\Delta m_j = +1$ for $\sigma+$ and $\Delta m_j = -1$ for $\sigma-$ [4, 5, 12, 31].

For example, with $\sigma+$ light shown in Figure 3.1, excitations can only occur from the $m_j = -3/2$ (heavy hole) and $-1/2$ (light hole) states to the $m_S = -1/2$ and $m_S = +1/2$ states of the conduction band. However, it is important to note, the heavy hole-to-conduction band transition has a three times higher transition intensity than the light hole-to-conduction band transition [5]. The result is three electrons in an $m_S = -1/2$ for every one in an $m_S = +1/2$ state in the conduction band, resulting in -50% polarization according to Equation 3.5. The same logic can be applied for $\sigma-$ light, resulting in 50% polarization. However, this theory only works at $k=0$ and assumes no perturbations to the energy bands such as magnetic field, quantum confinement, strain, etc.

3.3.2 Electron Polarization

While the transition intensities can provide an estimate of the instantaneous polarization, the recombination of the electrons with holes and the spin-lattice relaxation of the conduction electrons must also be considered to determine the steady-state mean electron spin value,

$\langle S_Z \rangle_{\sigma\mp}$. The expression for the expectation value is [12, 36]

$$\langle S_Z \rangle_{\sigma\mp} = \frac{\langle S_Z \rangle_0}{1 + \frac{\tau_e}{T_{1e}}} + \frac{S_0}{1 + \frac{T_{1e}}{\tau_e}} \quad (3.6)$$

where $\langle S_Z \rangle_0$ is the mean electron spin value after excitation, S_0 is the conduction electrons' mean thermal-equilibrium spin value, τ_e is the time constant for electron-hole recombination, and T_{1e} is the conduction electron spin-lattice relaxation time constant. Since electrons are spin- $1/2$, the polarizations are equal to $2 \times \langle S_Z \rangle_0$, $2 \times \langle S_Z \rangle_{\sigma\mp}$, and $2 \times S_0$. In addition, $\langle S_Z \rangle_0$ is equal to ± 0.25 for $\sigma\mp$ light using the theory above.

Additional perturbations (such as magnetic field, strain, and more) result in a much more complicated $\langle S_Z \rangle$, which can be calculated using sample specific parameters and experimental conditions, as a function of photon energy. In addition, excitation not at $k=0$, where the atomic-like states model is no longer applicable, can also occur and must be accounted for, leading to a photon-energy dependent $\langle S_Z \rangle$, as shown previously by our group [22]. The calculations of $\langle S_Z \rangle$ are difficult and time consuming due to the inclusion of the magnetic field induced Landau levels [14] and electron energy band mixing [37]. These calculations show $\langle S_Z \rangle_0$ is not a constant ± 0.25 , as predicted by the simple theory for an ideal system presented earlier. In fact, the electron polarization can be seen to vary between $\pm 100\%$ polarization, depending on the sample and experimental parameters [14, 17, 37].

3.4 Nuclear Polarization

Ultimately in OPNMR, we detect the nuclear spins and their polarization dependent signal intensity. However, thus far, only hyperpolarization of the electrons has been discussed.

The polarization of the electrons transfer to the nuclei via the hyperfine interaction. Two different models have been developed to explain the process of polarization transfer between the hyperfine coupled electron and nuclei [12].

3.4.1 Hyperfine Interaction

The first model relies on donor impurity states, with a shallow well potential, and defects in the crystal lattice to trap the excited polarized electrons. The electrons thus become localized and transfer their polarization to the nuclei coupled strongly by the Fermi-contact portion of the hyperfine interaction (Equation 2.11). The bulk of the semiconductor then becomes polarized through nuclear spin diffusion and the weaker dipolar portion of the hyperfine interaction. Due to the slower spin diffusion rate and dipolar coupling strength, the optical pumping time would be limited by their time constants.

The second model relies on mobile electrons. Since the electrons are mobile, the electron wavefunction overlaps with a given nuclei for a short period of time, diminishing the strength of the Fermi-contact portion of the hyperfine interaction. This ultimately leads to a weaker time-averaged coupling between the polarized conduction electrons and the nuclei and thus, a slower signal build-up as a function of optical pumping time. This model does not rely on a second mechanism to transfer the polarization to the semiconductor throughout the irradiated volume since the time-averaged coupling strength would be the same for all irradiated nuclei.

Both methods are plausible and have been shown to exist in a variety of different samples [12, 38, 39]. The results appear to be sample dependent and potentially a competition between the two effects; the dominant one being determined by sample parameters.

3.4.2 OPNMR Profiles

To help understand the spin physics governing the optically pumped enhancement of NMR signals, integrated NMR signal intensities, for a given laser power, are plotted as a function of photon energy, known as an “OPNMR profile” [12]. An example OPNMR profile can be seen for a typical semi-insulating (si, nominal free charge carriers) GaAs semiconductor in Figure 3.2. The two circularly polarized light excitations result in signals opposite in phase due to the opposite polarization of the electrons illustrated above. At energies below the band gap energy (E_g), large signal enhancements are observed due to the low absorption coefficients for excitations at the onset of absorption and to shallow defects. The low absorption coefficient allows the laser to penetrate fully through the semiconductor and polarize a large number of nuclei. At the band gap, absorption increases greatly, limiting the penetration depth of the laser and polarization, resulting in a smaller number of polarized nuclei and a diminished NMR signal. Above the band gap, oscillations are observed due to the oscillatory absorption created by Landau levels, where the electrons form cyclotron orbits, affecting their energy levels [12, 14]. Overall, the OPNMR profile allows for some understanding of the physics governing the NMR enhancement.

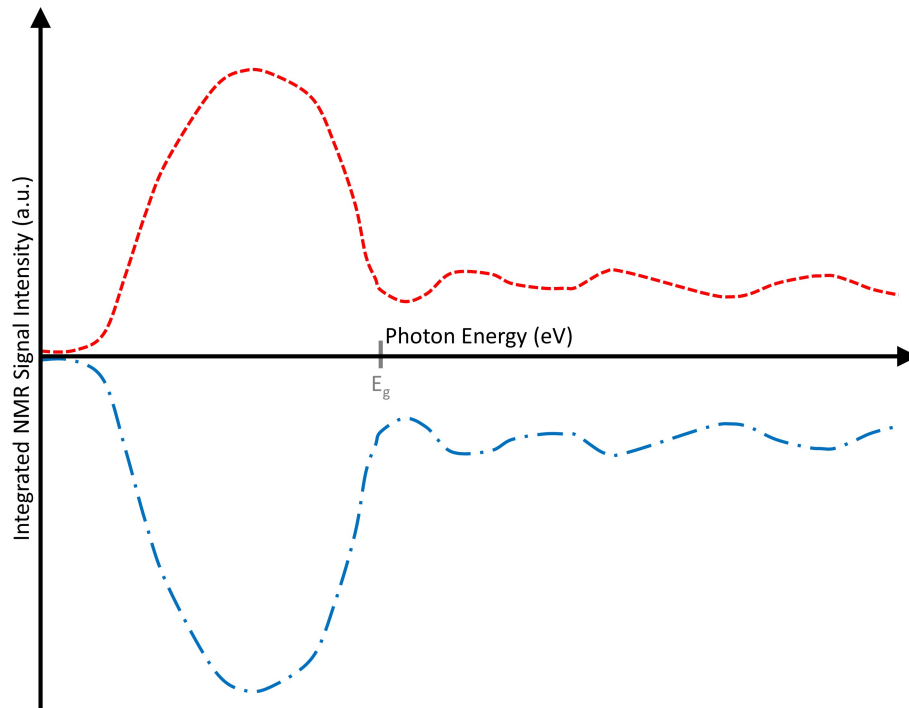


Figure 3.2: Sample OPNMR profile for a typical semi-insulating (si) GaAs semiconductor wafer. The red dashed line represents the $\sigma-$ NMR signal intensity and the blue dash-dot line represents the $\sigma+$ NMR signal intensity. The characteristic trends are discussed in Section 3.4.2.

Chapter 4

NMR Hardware and Optical Equipment

In order to run OPNMR experiments, a large assortment of equipment is necessary. The entire apparatus for simultaneous OPNMR and ODNMR detection can be seen in Figure 4.1. The laser/optics table, cryostat, NMR magnet, NMR spectrometer and single-channel OPNMR probe were designed and built by previous graduate students. The optics table, cryostat, NMR magnet and probe were designed in a single horizontal plane in order for easier alignment of the laser and collection of photoluminescence from electron-hole recombination.

4.1 Janis Horizontal Cryostat

For optimal OPNMR enhancement, the sample space needs to be cooled to very low temperatures (typically less than 10 K). By doing so, we increase the relaxation times of the excited electrons and nuclei, as well as “freeze-out” phonon modes. To do this, we employ a helium recirculating cryostat which allows for continuous experiments without the need for

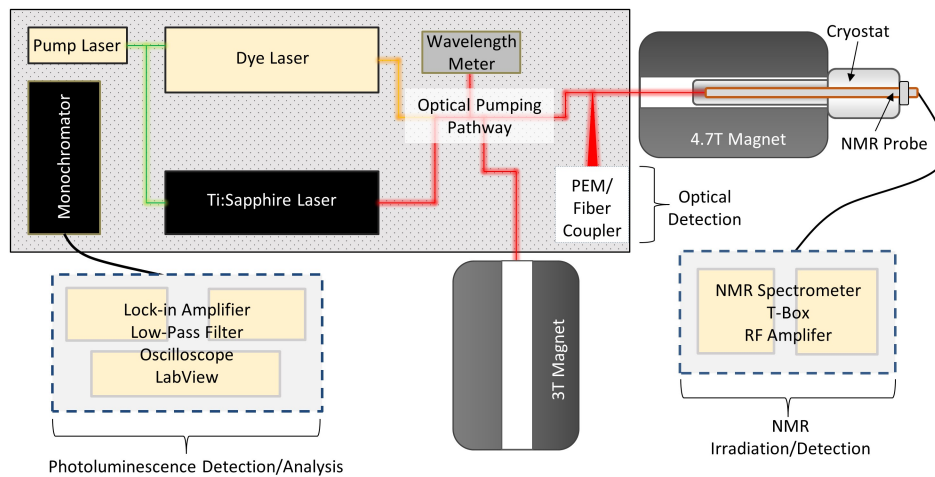


Figure 4.1: Experimental setup for the combined OP/ODNMR apparatus. The optical control and detection is completed on a non-magnetic aluminum laser table. Measurements at two magnetic fields are possible via Oxford superconducting magnets. The cryostat and probe can be moved between the two magnetic fields where a Tecmag spectrometer is able to control the RF and measure the NMR signals.

liquid helium. Temperature is regulated during experiments through the use of a Lakeshore 340S temperature controller coupled with a Janis SHI-950 exchange gas cryostat utilizing a Sumitomo cold-head (RDK-415D, 1.5 W cooling power at 4.2 K). Exchange gas cryostats work by mounting a sample into a evacuated chamber which is then filled with helium gas to form a thermal link between the sample/probe and the refrigerator to exchange heat. The Janis SHI-950 system is connected to a helium compressor via insulated gas lines that run to the attached cold head on the cryostat, forming a closed loop circuit. The water-cooled compressor first pressurizes the helium gas, before the cold head expands the gas to cool the sample space. The expanded gas then returns to the compressor to repeat the process. A copper strap is attached to both the sample space and the cold head, thermally connecting the two, allowing the sample space, exchange gas, and thus the sample to reach the desired temperature.

Temperature stabilization of ± 0.02 K was routinely achievable at a temperature of 6 K for low to medium laser powers ($P_{\text{laser}} < 200$ mW) under continuous-wave irradiation over periods of tens of minutes and up to hours. The Lakeshore 340S temperature controller employed a Cernox thin film resistance sensor to detect the temperature, which is unaffected by magnetic fields and has options to reach down to 100 mK. The temperature controller was capable of varying the temperature of the sample space (with the NMR probe in place) over a range of 5.5–300 K through the use of a resistive heater embedded in the side of the probe chamber. The sample/probe chamber was kept thermally isolated by vacuum chambers and with metallized biaxially-oriented polyethylene terephthalate (polymer) sheeting to provide radiation shielding for the cryocooler as described in the Janis product catalog for the SHI-950 series refrigerator systems.

The end of the cryostat inserted into the magnet bore was fitted with a series of three windows to provide optical access to the sample. The innermost window was epoxy-mounted strain-free in a flange which was clamped with an indium wire seal to the body of the inner chamber. The middle and outermost windows not in contact with the sample space were mounted using O-rings, as they were isolated from cryogenic temperatures. A vacuum pressure of less than 30 μ torr in the outer vacuum chamber was required to achieve a temperature of 5.5 K. To obtain these pressures, the system was evacuated using a Varian V-70 turbo molecular pump backed by a Varian SH-110 oil-free scroll pump.

Cool down of the Janis cryostat requires ~ 3 h to attain the desired temperature after evacuation in the horizontal orientation. Sample changes were possible while the system was running, by flowing helium gas over the top of the probe chamber to nominally prevent air from entering. The internal temperature must be raised to ~ 170 K before the probe could be removed, to prevent solidification of gaseous contaminants on the probe body and in the sample space. However, re-cooling the system only requires about an hour subsequently. Occasionally, a small amount of condensation built up on the outer optical window at the end of the cryostat, from the outer cryostat body conductively cooling over periods of hours. To prevent this from occurring, a continuous stream of dry compressed air is flowed into the bore of the magnet aimed at the window whenever the cryostat was in operation.

4.2 Optical Equipment

The optical path originates with a Spectra-Physics Millennia diode laser which outputs 532 nm light up to 12 W of power. The Millennia is used to pump two separate ring lasers, a Coherent 899-21 Ti:Sapphire laser (used for most experiments here) and a Sirah Matisse DS laser. The

ring laser used in an experiment is selected by a flipping mirror to direct the laser into one of the two continuous-wave lasers. A power of 10 W was typically used to pump the two continuous-wave lasers, resulting in ≈ 2 W of power for a fully aligned laser. The Coherent 899-21 allowed for a tunable wavelength range of 725–1000 nm with an unlocked linewidth of 30 GHz (not locked to the reference cavity). The Sirah Matisse laser has a wavelength range of ≈ 550 –1000 nm with an unlocked linewidth of ≈ 20 MHz depending on the dye used in the laser.

From the two continuous-wave lasers, which are linearly polarized, the laser beam is directed through a half-wave plate to change the orientation of the linear polarization with respect to the beam splitter cube the laser beam is directed into. The fraction of linear light polarized in the vertical direction is directed to a Bristol wavelength meter to determine the energy of the photons, while the other fraction of linear light polarized in the horizontal direction continues on towards the sample. The combination of the half-wave plate and beam splitter cube allows for control of the laser power reaching the semiconductor. The optical path continuing towards the sample then goes through a focusing lens in order to have an ≈ 2 mm beam diameter at the sample. A shutter controlled by TTL pulses from the NMR spectrometer allow for control of timing for when the laser can optically pump the sample. Lastly, the linear polarized light passes through a quarter wave plate or a liquid crystal retarder (LCR, which can be controlled by the spectrometer as well) in order to change the linear polarization to one of the circular polarizations or an intermediate elliptical polarization.

4.3 Pre-existing NMR Hardware

Two horizontal-bore magnets (98 mm bore) from Oxford Instruments are used individually in experiments to probe the external magnetic field dependence (B_0) at 3.0 and 4.7 T fields. The field homogeneity is rated to less than ± 10 ppm over a cylinder 80 mm long and 50 mm in diameter (± 3.75 ppm over 80 mm along the field axis). These sizes are much larger than the samples size (even more so for the irradiation volume) of the semiconductor, and the field is sufficiently homogeneous using cryogenic shimming. For example, ^{11}B NMR was acquired for $\text{BF}_3 \cdot \text{O}(\text{Et})_2$ (*l*) in the 4.7 T magnet (Larmor frequency of 64.22 MHz) with this setup and had a Lorentzian shaped resonance with a full-width half-maximum value of 65.1 Hz (≈ 1 ppm). In addition, the magnets are both actively shielded, bringing the “5 Gauss line” (for safety) at or inside the footprint of the magnets. This allow the other components affected by magnetic fields (such as the Faraday rotators in lasers and the liquid crystal variable retarder) on the optical setup to be located much closer to the magnets than without the shielding.

All the NMR hardware was controlled with a Tecmag Apollo spectrometer. The Tecmac Apollo uses its own software, NTNMR, to communicate with a computer. The spectrometer is able to control the RF amplifiers, the RF pulses (timing, phase, intensity, and shape), the helicity of light following the LCR, the laser shutter being open or closed, and the signal acquisition. A variety of amps (500–1000 W) and RF filters were used depending on the experiment and nuclei of interest.

A single-channel tank circuit OPNMR probe was originally built for use with the cryostat. It employed a typical 6–8 turn solenoid coil with a split between the middle turns to allow for optical access to the sample. The primary limit to B_1 power was the breakdown and arcing of the tunable capacitors in the helium gas atmosphere. These issues could be overcome

with more robust capacitors, however, B_1 fields of ≈ 35 kHz (greater than necessary for our typical OPNMR experiments) were able to be reached for the entire range tested of ≈ 28 – 63 MHz. With the probe in place, the cryostat reached a base temperature near 5.5 K in approximately 3 h and could be operated with a 200 mW laser load at a constant sample temperature setting of 6.00 ± 0.02 K for many weeks at a time.

4.4 Two-Channel Probe Design

A two-channel static NMR probe was designed and built for use at cryogenic temperatures (< 6 K) in conjunction with laser irradiation for optically-pumped NMR (OPNMR). Since the single-channel probe was able to reach the desired temperatures, many of the design concepts were carried over to the two-channel probe. A single NMR cable will be used to send the RF down to the doubly resonant circuit in order to limit the thermal connection to room temperature. Pulse sequences for the two-channel probe were configured to test the probe performance and in order to take advantage of the polarization from optical pumping while measuring various NMR spectra. Example two-channel OPNMR experiments include decoupling and cross polarization on ^{113}Cd and ^{125}Te in a crystalline CdTe wafer.

All of the designs for each piece of the probe can be seen in Appendix A.

4.4.1 Design of Probe Backbone

The top of the two-channel probe was designed using the blank 3 ” stainless steel sanitary tube solid end cap to insure a proper seal at the top of the cryostat (Figure 4.2). Four $\frac{1}{8}$ ” NPT threaded holes were added in a 1 ” square for the accommodation of up to 4 tuning rods

and their respective knobs using Swagelok Ultra-Torr connectors. In the middle of the top cap, a fifth $\frac{1}{8}$ " NPT threaded hole was added for the addition of an optical fiber or electrical connections for future experiments. One of the outer NPT holes and the middle NPT hole are closed with NPT plugs since they are not necessary for the circuit presented in this paper which only requiring three tunable capacitors. Outside of the NPT holes, two hermetically sealed BNC adapters were added (only one of which is necessary). On the bottom face of the top cap, four threaded holes were added in a $1\frac{1}{4}$ " square pattern for the long brass support rods to screw in.

Brass support rods ($\frac{1}{8}$ " diameter) were fabricated to reach the "sweet spot" of the magnet. The brass support rods screw into the top cap. The bottom portion of the rods are also threaded in order to use nuts to hold the probe head in position (the portion of the probe with the RF circuit). Due to the small diameter of the brass rod, 4 support rods are included in the design in order to support the weight.

Six brass baffles were added to prevent the convection of the cold helium gas toward the top cap and to add support to the probe. All six brass baffles are hard soldered in place above the cold strap of the cryostat, separated by roughly 3". Four extra holes and a slot were cut out to allow passage of the tuning rods, the NMR coaxial cable, and any future additions that will run the length of the probe. The baffles are rotated with respect to each other to prevent a straight radiation path to the top cap. Directly below the brass baffles (and still above the cold strap of the cryostat) is a G10 fiberglass baffle to provide a tighter seal. Similar to the brass baffles, the G10 baffle has four holes for the support rods and four holes for the tuning rods. Instead of a slot, a $\frac{1}{5}$ " hole was cleared for any cable or wire passing through to the probe head.

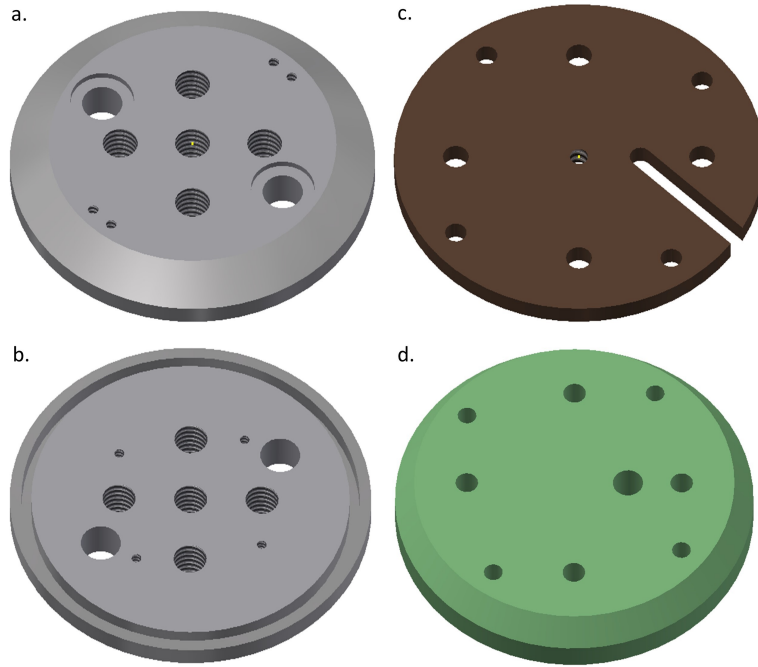


Figure 4.2: Designs for the top cap and baffles of the two-channel probe. a. The top of the top cap. b. The bottom of the top cap. c. The brass baffles. d. The G10 baffle.

The probe head, shown in Figures 4.3 and 4.4, consists of four main parts: a top copper block, a G10 fiberglass block, a bottom copper block, and a copper can that encases these blocks. A copper can slides over the entire probe head in order to protect the electronics and make the probe more robust. Screws are used to clamp the copper can to the top and bottom copper blocks. The G10 portion is a ring in the probe head to allow capacitors to float from ground. Another option for the capacitors is in the bottom copper block which would ground them. The bottom of the sample mount holders are attached by a screw into the bottom copper block, facing away from the top cap. Each sample mount holder has two portions (a top and bottom) which are specifically designed to hold our sapphire sample mounts. The bottom and top portions of the sample mount holder are used to clamp the sample mount in place. The sample rods are cylindrical on one side and a half cylinder on

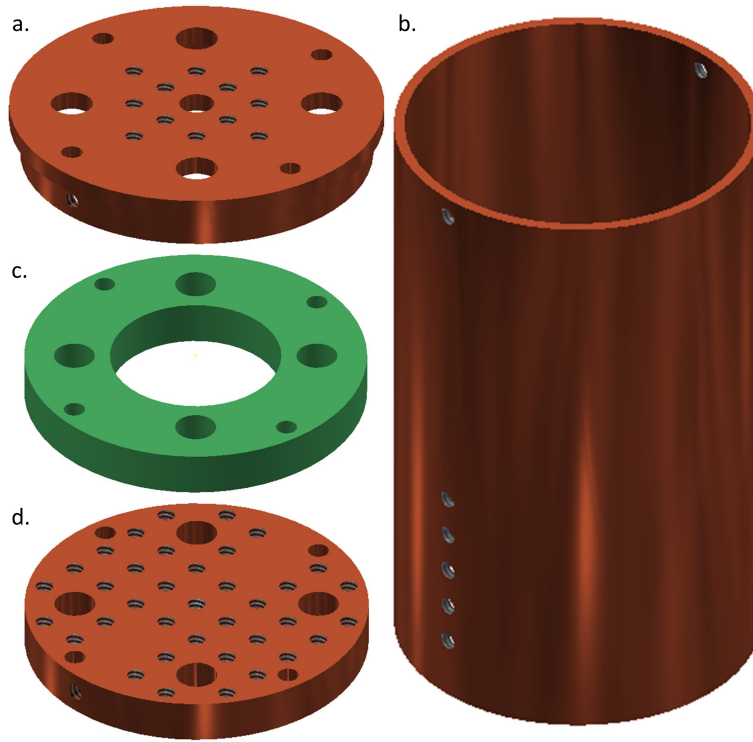


Figure 4.3: Designs for the probe head of the two-channel probe. a. The top copper block. b. The outer copper can. c. The G10 block. d. The bottom copper block.

the other (to provide a flat surface to mount the sample). These mounts force the sample to be normal to the magnetic field and laser.

In order to tune the resonance circuit at the bottom of the probe, a variable capacitor with a tuning knob/rod assembly is necessary. Short brass rods were fabricated to pass through and be sealed by the Swagelok Ultra-Torr vacuum fittings in the top cap. Small tuning knobs were added to the top of the brass rods outside of the probe for easier turning of the capacitor. The bottom of the brass rods are then fastened to the G10 tuning rods using brass couplers. The couplers are small brass cylinders bored out to fit the short brass rod, the G10 tuning rods, and the capacitors and are set in place using set screws. Two lengths of tuning rods are necessary due to the different lengths from the top cap to the G10 and

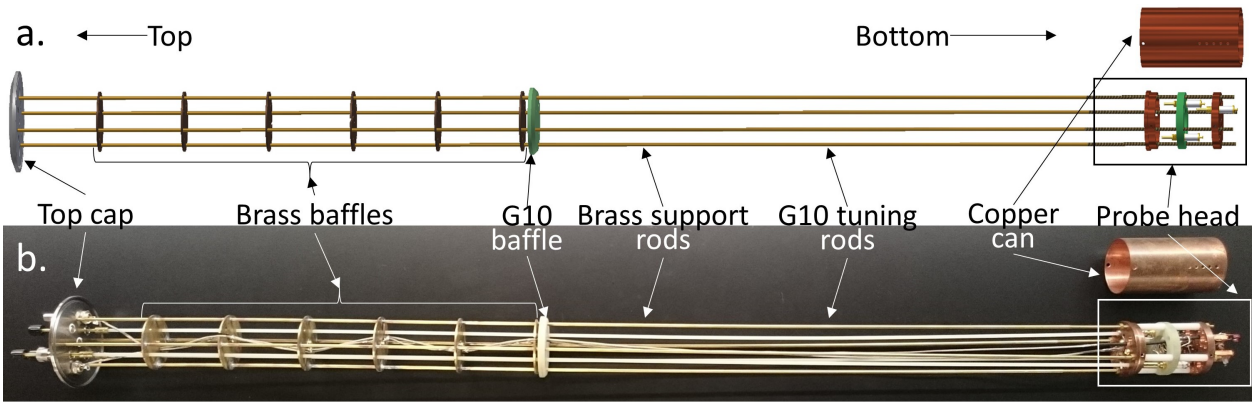


Figure 4.4: The full two-channel probe. a. The final design with the parts assembled. Parts not shown include the capacitor tuning assembly and the sample mounts. b. The finished product with all components including the circuit.

bottom copper blocks. The tuning rods were made out of G10 fiberglass to help reduce the cooling load and eliminate a thermal path to room temperature outside the cryostat. The bottom of the tuning rods were machined to fit into the tuning groove of the Voltronics 2 kV cryogenic capacitors (1.5–40 pF, NMAT40HVEK) to prevent the capacitor from slipping in the brass couplers when turning the tuning rods.

The probe head is attached by sandwiching the top and bottom copper blocks with nuts on the support rods. The copper and G10 blocks are kept apart by plastic spacers on the support rods. This design is able to reach temperatures below 6 K with the Janis recirculating cryostat even in the horizontal orientation. The final drawing and probe can be seen in Figure 4.4.

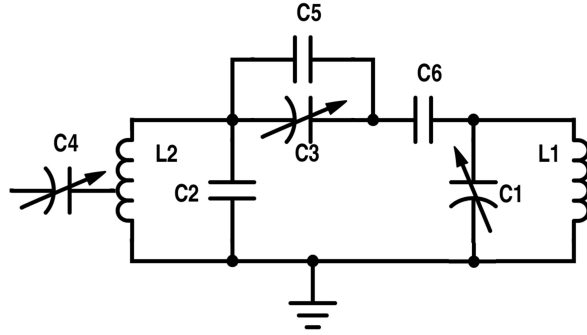


Figure 4.5: The two-channel NMR circuit located in the probe head. L1 is the NMR coil and L2 is the idler coil. The two inductors form LC circuits with their corresponding capacitors. The LC circuits are capacitively coupled by the C3-C5-C6 network. C4 is the matching capacitor tapped to the idler coil.

4.4.2 Electronic Circuit

The two-channel circuit (Figure 4.5) is based on a previously reported design[40, 41]. The circuit has two LC circuits resonant at the higher frequency of the probe. One of the LC circuits contains the NMR coil (L1) while the other uses an idler coil. The NMR coil is a ≈ 0.5 cm solenoid coil with a ≈ 2.5 mm gap in the middle to allow the laser to pass for a total length of ≈ 0.75 cm. A variable capacitor (C1) across the NMR coil (L1) was used for more precise tuning of the higher frequency and to adjust for any changes due to cooling. The capacitors in the two LC circuits (C1 and C2) are connected through a floating tunable coupling capacitor section (C3, C5 and C6). The tunable coupling capacitor (C3) in the C3, C5, C6 section controls the frequency separation of the lower frequency ($\nu_{high} - \nu_{low}$) resonance. The C5 and C6 capacitors were added to decrease the voltage drop across the more expensive tunable capacitor. Because the voltage drop across capacitors in series is inversely proportional to the capacitance, adding a fixed capacitor in series will split the voltage drop between the capacitors. The fixed capacitor in parallel (C5) is added to increase the net capacitance of C3 and C5 and increase the voltage drop across C6. The matching capacitor

(C4) is used in combination with the tap location on the idler coil (L2) to match the two frequencies. The two floating tunable capacitors (C3 and C4) are thus located on the G10 block while the grounded tunable capacitor (C1) is mounted on the bottom copper block.

One of the main design philosophies was the use of a single coaxial cable to deliver the RF for both channels. This requires only one of the BNC connections installed in the top cap. For RF to reach the tank circuit, a thin 50Ω cable (originally shielded by a magnetic metal sleeve) was reshielded with a braided non-magnetic metal sleeve and connected to the C4 matching capacitor. The top of the cable is soldered to the bottom of the hermetically sealed BNC adapter in the top cap of the probe. The cable passes through the six brass baffles, the G10 baffle, and the top copper block. Along the path of the cable, the braided metal sleeve is soldered to the six brass baffles and fanned out at the top of the probe head where it is clamped to the top copper block with a screw and washer. The metal sleeve blocks noise from reaching the 50Ω cable by grounding it to the probe body.

In order to setup the circuit for two nuclei, the first step is to make both of the LC circuits resonant with the desired high frequency. The frequency of these circuits can be measured with the use of an inductively coupled sniffer loop. Once the two separate LC circuits are created, the addition of the coupling capacitor section (C3, C5, and C6) and ground, as described above, should be added. The coupling capacitor section then needs to be tuned in order to form both the symmetric and anti-symmetric mode of the circuit. The two modes will have different frequencies which allows for tuning to the lower frequency. At this point, the circuit is resonant with the two desired frequencies.

The next step is to connect the circuit to the probe and thus allow the user to drive the circuit with RF. This can be completed by finding a tap position on the idler coil which provides approximately the same amount of coupling to the two frequencies (unless equal

coupling of the two frequencies is not desired). This can be difficult as the tap position onto the idler coil will likely change as a function of temperature. Therefore, a few iterations may be necessary in order to find the tap position with equal couplings to both frequencies. The matching capacitor can then be soldered in place between the $50\ \Omega$ cable and the idler tap. The tuning of the matching capacitor is then able to maximize the coupling to the two frequencies. At this point, the probe can then be used as desired.

When using this two-channel probe design in the typical two-channel setup with two amplifiers, a BNC Tee adapter at the top of the probe can be used to run cables to both amps. However, this generates a problem of signal possibly going along the other line, away from the receiver, as well as noise from the secondary amp possibly swamping the signal. We have found the use of two high power filters on both lines near the probe, a low power filter after the spectrometer but before the secondary amp, and another low power filter after the t-box but before the pre-amp removes both of the potential problems. This is especially necessary when running NMR sequences which require the second channel to be on during the acquisition, such as during decoupling.

4.4.3 Performance and Testing

This probe design, while simpler and less expensive than published alternatives[42], does not provide isolation between the RF channels. The isolation is added before the two RF channels meet at the probe with the use of factory-made high-power and/or home-made coaxial RF filters. Home-made coaxial filters can be made by using shorted and open coaxial traps to affect the impedance of one frequency more than the other. In this case, with ^{113}Cd (44.406 MHz) and ^{125}Te (63.078 MHz), greater than 45 dB of isolation, with less than 2 dB

of insertion loss for the other channel, was obtainable using a stack of 2 home-made filters only.

The use of only external filters carries both pros and cons when it comes to the experiments. The downside is the necessity of multiple traps and/or filters in each channels' line. However, the filters and traps can be inexpensive and homemade if basic isolation is needed. The amount of isolation required depends on the experiment (i.e., if one uses high-power decoupling during the acquisition) and the amount of signal. The main problem encountered with low isolation was saturation of the pre-amp by white noise from the opposite channels' power amplifier. The performance of this design is very dependent on the voltage rating of the capacitors (for max power before arcing when cold, which will always be an issue in He gas atmospheres) and the filters used on the input lines (for max isolation). Larger B_1 fields can be reached when operating at room temperature without the He gas atmosphere, however, it does not mimic the conditions needed for OPNMR. Example probe performance can be seen below (Figures 4.7 and 4.8) for this probe with appropriate filters for ^{113}Cd and ^{125}Te and 500 V to 2 kV rated capacitors.

two-channel OPNMR Pulse Sequences

Two-channel OPNMR pulse sequences have been designed to demonstrate the performance of the probe design. OPNMR sequences can be thought of as three separate parts: the saturation of the nuclear spins, the optical pumping of the nuclear spins, and finally, the detection of the nuclear spins. The saturation portion relies on an RF pulse comb to fully destroy any net magnetization of the nuclear spins. The optical pumping portion is governed by the laser excitation physics of semiconductors and the hyperfine interaction which results in polarization of the nuclear spins[4, 12]. The pulse-acquire portion has typically used a

pulse $\leq 90^\circ$ or spin echoes (Hahn, quadrupolar, and solid) (Figure 4.6a). The laser has been left on during the acquisition in some previous experiments, allowing conduction electrons to affect the line-shape and frequency of the peak(s) as shown in Figure 4.6. For the performance testing shown here, the light was shuttered during the acquisition period.

The most simple addition to transform a single-channel pulse sequence to a two-channel pulse sequence is decoupling (Figure 4.6b). Decoupling of the “Y” nuclei with the dominant broadening/splitting can be used during the acquisition on the second channel in order to narrow the “X” spins being detected. Narrower resonances are ideal when measuring frequency shifts to reduce the error. Also, “OPNMR profiles” [12] could be obtained faster/more accurately due to the increased signal to noise ratio. This sequence demonstrates the ability to isolate the decoupling and acquisition channels with the use of external filters.

The next two-channel sequence implemented was optically pumped cross-polarization (OP-CP) as seen in Figure 4.6c. After optical pumping, saturation of the observed nuclei is implemented in order to avoid any effects of CP transferring to an already hyper-polarized nuclei. A 90° pulse on the non-observed nuclei is then followed by two Hartmann-Hahn lock pulses on both nuclei to allow the transfer of polarization[43]. We implement spin-temperature alternation pulse phasing[44] in order to remove potential artifacts. Due to limited isolation from our filter selection, a z -store pulse sequence ($\tau_{z-store} \approx 5$ ms) was used to allow recovery of the pre-amp after the long contact pulses on the second channel. Without the z -store sequence, baseline errors were observed due to the recovery of the receiving pre-amplifier during the acquisition. This sequence provides enhancements different from those typically achieved by standard cross polarization, due to the enhancement being dependent on the non-observed nuclear spin temperature, which is affected by the optical pumping process. However, since the magnetogyric ratios of nuclei typically observed in

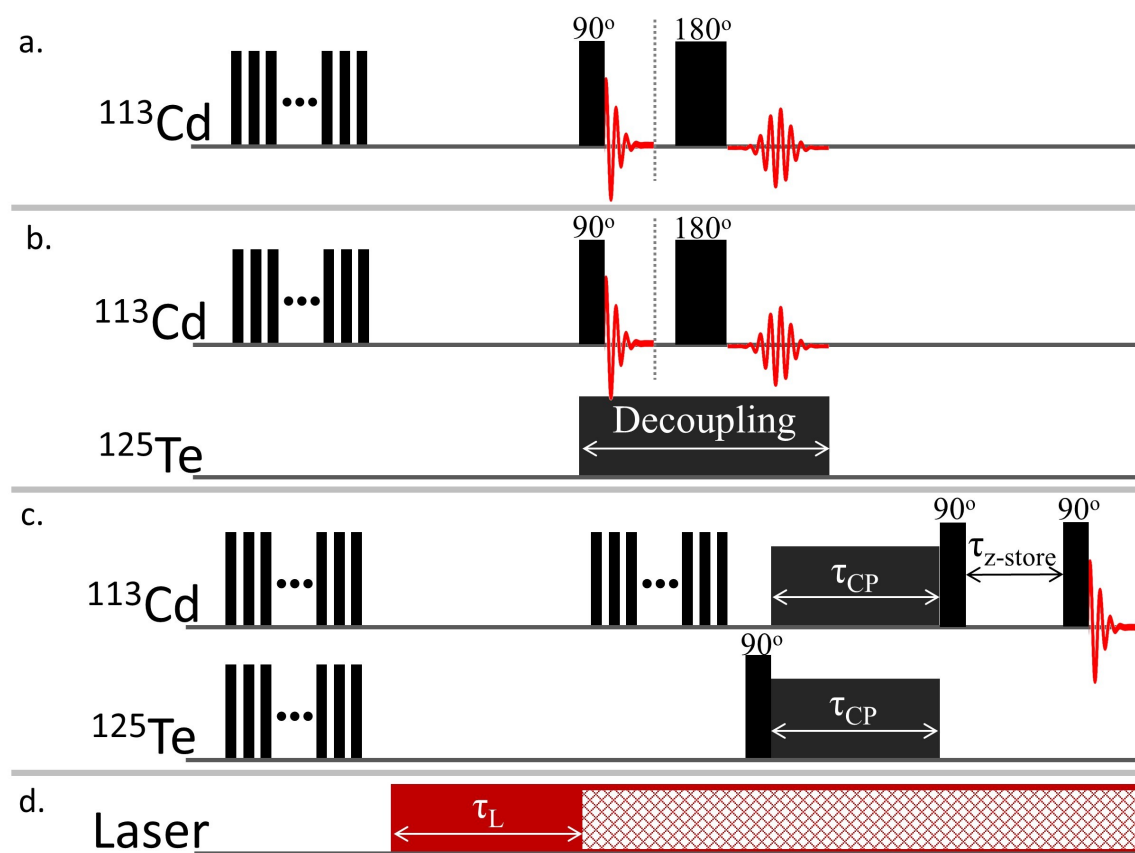


Figure 4.6: The a. OP Bloch decay and echo pulse sequence, b. OP Bloch decay/echo with decoupling sequence, c. OP-CP sequence and d. laser irradiation for all sequences. The laser filled with a cross stitch pattern represent the option of both full and zero intensity. The Bloch decay/echo sequences have a vertical dashed line illustrating the optional echo portion of the sequence. Note: The sequences are not drawn to scale with respect to the time axis.

OPNMR are similar, and a single nuclear spin temperature will be reached at equilibrium, the enhancement of the unobserved nuclei would be similar with and without the use of the CP sequence. Instead, this sequence is more of interest for spectral editing or analyzing CP curves for sample specific parameters including coupling strength and $T_{1\rho}$. This sequence demonstrates the ability to pulse on both channels simultaneously while maintaining the Hartmann-Hahn condition.

Experimental

A high resistivity wafer of CdTe was obtained from Marketech. The wafer is approximately 0.5 mm thick and was cut into a 2 mm by 4 mm rectangle. For initialization of the nuclear states, the sample was optically pumped at 805 nm at 7.0 ± 0.5 K. The RF powers for both nuclei (^{113}Cd and ^{125}Te) were adjusted in all experiments to obtain between 7 and 8 μs 90° pulses (~ 33 kHz). The ^{113}Cd abundance is 12.26 % and the ^{125}Te abundance is 6.99 %. All data shown were acquired with the laser only on during the τ_L period (off during the acquisition) in order to simplify the experiments in these demonstrations.

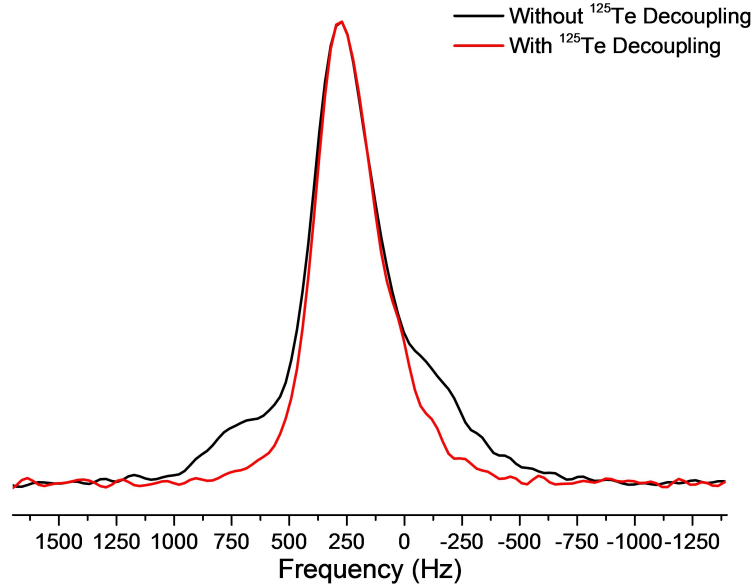


Figure 4.7: Normalized ^{113}Cd spectra without (black) and with (red) $^{125}\text{Te} \approx 10$ kHz decoupling power. The decoupling removes the line splitting caused by the nearest ^{125}Te isotopes. No noticeable increase in the noise is observed. The zero of the frequency axis is arbitrary.

CdTe NMR is known to have line splitting due to the coupling of the nearest nuclei[25]. The coupling strength is due to both dipolar and J -coupling interactions. When observing a single nucleus, such as ^{113}Cd which is tetrahedrally coordinated to four Te neighbors, both

the dipolar and J -coupled and the weakly dipolar coupled nuclei will be seen, as shown in Figure 4.7. The central peak is primarily ^{113}Cd directly bonded to only NMR-inactive Te isotopes (i.e., not ^{125}Te or ^{123}Te), and the satellites are primarily due to ^{113}Cd bonded to one ^{125}Te or ^{123}Te . Of all ^{113}Cd spins, 75 % have no ^{125}Te neighbors, and 22 % have exactly one. The remaining 3 % of ^{113}Cd sites have 2, 3, or 4 ^{125}Te neighbors. When decoupling ^{125}Te during the acquisition of ^{113}Cd spectra, the splitting is removed, and all nuclei appear to be uncoupled. As seen in the figure, decoupling can be executed at these strengths (≈ 10 kHz for ^{125}Te) without a noticeable increase in the noise using this probe with a single high-power filter on the ^{113}Cd channel (≈ 45 dB of isolation at the ^{125}Te frequency).

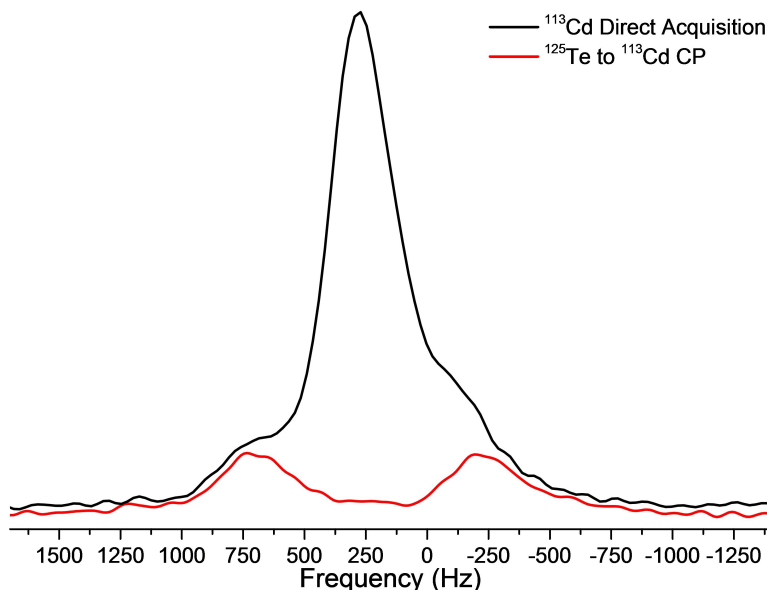


Figure 4.8: ^{113}Cd NMR spectra of bulk CdTe. Black line shows results of typical OPNMR pulse-acquire sequence. Red line shows results of OP-CP sequence with a τ_{CP} value of 1 ms. The OP-CP sequence with a 1 ms contact time allows for excitation of only the $^{113}\text{Cd}/^{125}\text{Te}$ spin pairs.

Since we are able to spectrally resolve between lone ^{113}Cd site (zero ^{125}Te neighbors) and ^{113}Cd - ^{125}Te spin pairs, crystalline CdTe is an excellent test case for showing the benefits of combined OPNMR and cross-polarization (CP). The transfer rate of polarization in CP is

dominated by the total coupling strength of the two isotopes. The central ^{113}Cd peak does not have a nearest ^{125}Te in the first shell, limiting the maximum coupling strength to that of the next-nearest ^{125}Te . The satellite peaks are separated by ≈ 1000 Hz, correlating to a much higher coupling strength than that of the central resonance. We can exploit the difference in coupling strength to observe only the coupled spin pairs as seen in Figure 4.8. Thus, we can use CP to eventually measure coupling strengths and spectrally edit to observe specific nuclei. Here, the CP Hartmann-Hahn condition was met at >25 kHz RF power (with 30–80 dB of isolation by the use of traps and high powered filters on each channel). It is important to note that traditional CP dynamics (using a thermodynamic model) relies on an abundant spin bath to act as a reservoir, which is not present here.

In conclusion, a relatively inexpensive two-channel probe with the ability for future additions was designed and constructed for use in OPNMR experiments. The probe can be easily altered to work in most cryogenic setups at temperatures less than 7 K. The probe itself has little isolation but isolation can be achieved with in-line filters. The probe is able to complete decoupling, cross-polarization, and more experiments with the use of standard high-power filters on each channel. The use of two-channels affords an increase of possible experiments which will lead to a better understanding of the optical pumping phenomena.

Chapter 5

Magnetic Field Dependence of Light Hole Transition via OPNMR

In collaboration with the National High Magnetic Field Laboratory, another OPNMR group (Dr. Bowers from University of Florida), and a semiconductor band structure theory group (Dr. Stanton from University of Florida), we attempted to further measure the light-hole transitions via OPNMR as a function of magnetic field.

5.1 Introduction

The electronic energy band structures of semiconductors is relatively well understood and has been studied in the past. For semiconductors with a cubic crystal structure, the valence band has two energy bands (light hole and heavy hole) which are degenerate in energy at $k=0$. These two band states have different effective masses, separating the energy bands when $k \neq 0$. An electron can be excited from valence band states to the conduction band states by a laser with energy greater than or equal to the energy separation, known as the

bandgap. These states can be taken advantage of in OPNMR by using allowed transitions to polarize the electron spins. The electron spins transfer polarization to the nuclei through a Fermi contact hyperfine interaction. The increased nuclear polarization is then detectable by solid-state NMR.

Common OPNMR experiments involve recording NMR spectra at different wavelengths (i.e., photon energy) of the excitation laser. Each NMR spectrum is then integrated or fit to a Gaussian in order to calculate the area of the signal, which is proportional to the nuclear spin polarization and the volume of the polarized nuclei. The signal is plotted against photon energy to determine the energy of the transition (termed an OPNMR profile as in Figure 3.2). While other factors, such as penetration depth, can affect the total nuclear polarization, resolved spin oriented transitions can be seen as “peaks” and “valleys” in the overall nuclear polarization when plotted against laser energy. The “peaks” and “valleys” are dependent on the band structure of the semiconductor and the allowed transitions between the energy bands, allowing one to determine the band structure such as Landau levels [4, 14].

Since spin oriented electrons lead to increased nuclear polarization, it is important to understand the processes behind OPNMR that lead to electron polarization. For bulk GaAs, two valence bands (heavy hole and light hole) are degenerate in energy at $k=0$ and have m_j values of $\pm\frac{3}{2}$ and $\pm\frac{1}{2}$, respectively. The conduction band has an m_j value of $\pm\frac{1}{2}$. When illuminating with circular polarized light ($\sigma+$ or $\sigma-$), each photon carries with it either +1 or -1 unit, respectively, of angular momentum which gives rise to particular interband transitions. For quantum wells (studied in this experiment), the confinement in the z -direction induces an energy separation for the heavy and light hole bands at $k=0$. Therefore, it would take a higher photon energy to excite from the light hole band to the bottom of the conduction band than from the heavy hole band, shown schematically in Figure 5.1.

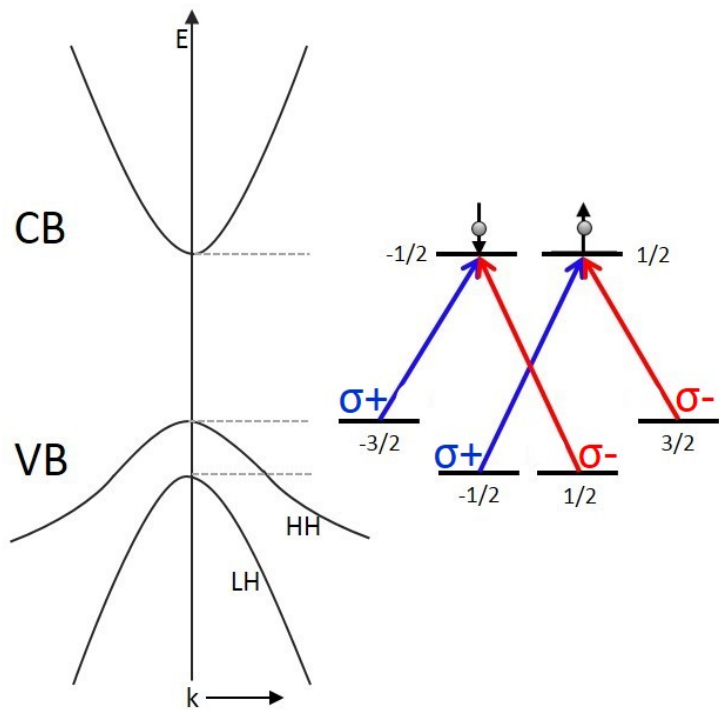


Figure 5.1: Conduction (CB) and valence band (VB) schematic showing the transitions from the heavy hole (HH) and light hole (LH) to the bottom of the conduction band using circularly polarized light. Allowed $\sigma+$ light transitions are represented by blue arrows while $\sigma-$ is represented by red arrows.

The polarization of the light determines the allowed transitions from the valence band. The LH transition for σ^- (where the photon carries -1 unit of angular momentum), connects the LH $|+\frac{1}{2}\rangle$ state to the CB $|-\frac{1}{2}\rangle$ state. Conversely, σ^+ light, carrying +1 unit of angular momentum connects the LH $|-\frac{1}{2}\rangle$ state with the CB $|+\frac{1}{2}\rangle$ state. The resulting electron polarization when excited from these light hole states is opposite of the heavy hole states if the circular polarization of the light remains constant.

When a magnetic field is applied, the bands form subband Landau levels which can be detected with OPNMR [37]. Allowed interband (valence band to conduction band) transitions are now not only limited by $\Delta m_j = \pm 1$ but also by the change in the subband Landau levels. The allowed interband transitions depend on the orientation of the sample in the field and the Poynting vector (direction of the energy flux density from the laser). The goal of these measurements is to further prove OPNMR can measure the light hole-to-conduction band transition, by performing OPNMR profiles, on the same sample, with completely different equipment and comparing to previous published data and theory. Polarized photoluminescence excitation (PLE) was also performed to corroborate both the newer and older OPNMR data. Multiple external magnetic fields (B_0) were applied to look at the magnetic field dependence of light hole-to-conduction band transition.

5.2 Experimental

OPNMR experiments were performed at both the National High Magnetic Field Lab (NHMFL, Tallahassee, FL) and Washington University in St. Louis (WUSTL). Polarized photoluminescence excitation (PLE) was performed at Washington University in St. Louis as well. An identical sample was studied at both locations and was grown on a single crystal bulk GaAs

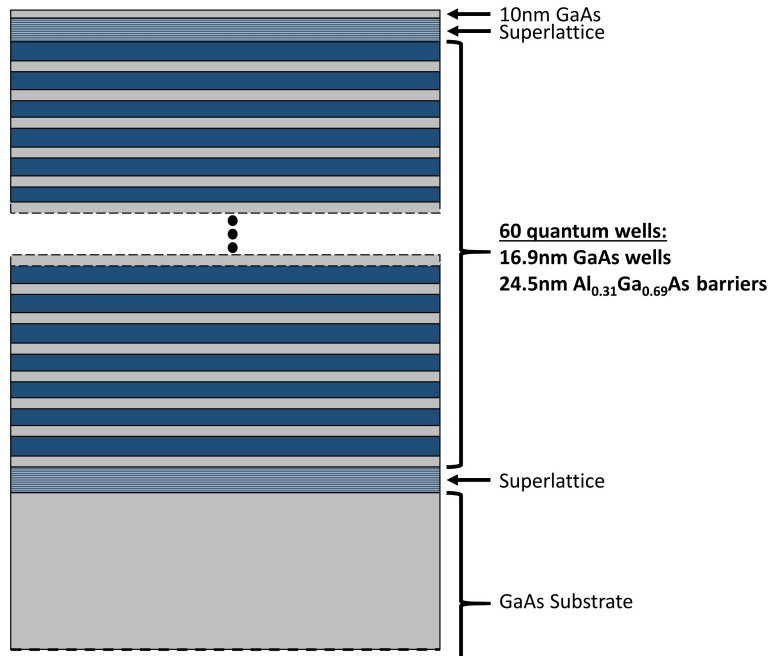


Figure 5.2: Quantum well sample for light hole transition measurements. Gray areas indicate the GaAs portions of the sample. Blue areas indicate $\text{Al}_{0.31}\text{Ga}_{0.69}\text{As}$ barriers. The portion of the sample studied is the 60 quantum wells between the two superlattice structures.

base substrate using molecular beam epitaxy (MBE) at the Ruhr Universität in Bochum, Germany. The sample contained 60 GaAs quantum wells separated by $\text{Al}_{0.31}\text{Ga}_{0.69}\text{As}$ barriers. The GaAs quantum wells were 16.9 nm thick with 24.5 nm barriers. The set of 60 quantum wells and barriers were sandwiched between superlattices (alternating quantum wells/barriers confined to < 5 nm). The sample was topped by a 10 nm GaAs capping layer. The total sample, including the substrate, was approximately 1 mm thick and can be seen in Figure 5.2.

At both locations, the sample was mounted to a piece of sapphire to act as a heat sink, using Apiezon grease. Temperature was monitored using a Lakeshore 340 temperature controller, and homebuilt single-channel NMR probes were used to acquire the NMR data. The probe and sample were inserted into a space which was evacuated then back-filled with a small

amount of helium gas. In both experimental setups, the plane of the quantum well was perpendicular to the magnetic field, which is parallel to the laser propagation direction.

5.2.1 OPNMR at NHMFL

The National High Magnetic Field Lab (NHMFL) employs a vertical variable superconducting magnet that can reach up to 17.5 T. The magnet has a sealed cold bore which provides the cooling to hold the sample space at 4.5 ± 0.5 K. ^{71}Ga NMR measurements at low magnetic fields (51.9–129.8 MHz) were acquired while ^{69}Ga NMR was obtained for the highest field (120.6 MHz) due to the tuning frequency range of the probe. The NMR spectra were recorded on a homebuilt spectrometer using a PTS 3200 frequency synthesizer and a CPC MRI Plus amplifier. Four transients were recorded for each spectrum using a four step phase cycling (CYCLOPS [3]).

A Coherent Verdi laser (at 4 W) was used to pump a Coherent Ti:Sapphire Mira 900 laser with an approximate linewidth of 0.4 meV at these wavelengths. The beam was focused to have an approximate 3 mm beam diameter at the sample. The wavelength of the laser was monitored using a 0.7 m McPherson monochromator with a 600 grooves/mm grating and a charge-coupled device (CCD) camera. The laser power was held at 200 mW (2.8 W/cm^2) and was measured before entering the bore of the magnet. The power was measured using an Ophir Nova Power Meter. A quarterwave retarder was used to create circularly polarized light. The sample was irradiated for 30 s (τ_L) for each scan.

5.2.2 OPNMR and Polarized PLE at WUSTL

The Washington University in St. Louis lab employs two horizontal superconducting magnets with magnetic fields of 3.0 T and 4.7 T. A helium recirculating cryostat made by Janis (SHI 950) is used to keep the sample at 6.0 ± 0.3 K. The NMR spectra were recorded on a TecMag Apollo spectrometer. A single transient was acquired at each wavelength used for optical pumping. ^{69}Ga NMR was obtained for all points.

A Spectra-Physics Millennia X laser (at 10 W) was used to pump a Coherent Ti:Sapphire 899-21 ring laser with an approximate linewidth of 30 MHz. The beam was focused to have an approximate 2 mm beam diameter at the sample. The sample was irradiated for 60 s (τ_L). The wavelength of the laser was monitored using a Bristol 521 Wavelength Meter which has a 0.01 nm resolution. The laser power was held at 100 mW (3.2 W/cm^2) for the 4.7 T profile and 200 mW (6.4 W/cm^2) for the 3 T profile. The power was measured before the magnet bore using a Coherent FieldMate Power Meter. The laser passed through a quarterwave retarder in order to create circularly polarized light. Polarized photoluminescence was collected by passing through a photoelastic modulator (PEM) (Hinds Instruments PEM-100) and a beam splitter cube before reaching the monochromator (Acton SpectraPro-2750; 0.75 m path length) and being detected by an avalanche photodiode (APD) detector. A lock-in amplifier (Stanford Instruments SR-830) and a low-pass filter (Stanford Instruments SR-640) were used to lock on to the PEM frequency and measure the total light emission, respectively.

5.2.3 Procedure

The gallium isotope measured by NMR was first saturated using a standard saturation pulse sequence to destroy any magnetization that has built up between experiments (due

to relaxation processes). Thus, the recycle delay (1 s) was irrelevant since any recovered magnetization is destroyed at the start of the experiment. This was followed by a period of time (τ_L) where the polarized laser pumped the sample. Even though the two locations used a different τ_L time and power density, no affect on the transition energy measurement is expected. A longer pumping time would not shift electron energy states but will result in more signal (until saturated). More signal (i.e. greater $\%N$ of the NMR spectra) results in smaller error bars for the points in the OPNMR profile and should have no effect on the energy levels of the bands. A higher power density increases the number of polarized electrons in the conduction band which can increase the polarization rate (if not saturated) and thus require a shorter τ_L to achieve a certain $\%N$). Both locations used power densities low enough to avoid sample heating and electron-electron correlation effects which could affect the energy levels. A $\pi/2$ RF pulse ($6 \pm 1 \mu\text{s}$ with both setups at all fields) was applied prior to acquisition. The probes were tuned at each external field and comparable impedance matches were obtained. This allowed for similar B_1 strengths (only dependent on the RF amplifiers frequency dependency gain curve) and thus a consistent pulse length can be used without sacrificing signal. The $\pi/2$ pulse length was optimized under optical pumping conditions at the photon energy which provided the largest signal intensity. The optical pumping conditions polarized the nuclei to a detectable limit. The standard $\pi/2$ RF pulse calibration was completed following the optical pumping for each pulse length acquisition. The pulse sequence can be seen in Figure 5.3.

A thermally relaxed spectrum was first acquired with an inspection pulse after allowing the nuclear T_1 process to occur for a given amount of time (typically overnight). No laser was used to optically pump the sample in order to obtain a Boltzmann thermally polarized spectrum. This spectrum is phased up to be absorptive. The phase angle used for each OPNMR spectrum was the same phase used to make the thermal signal purely absorptive

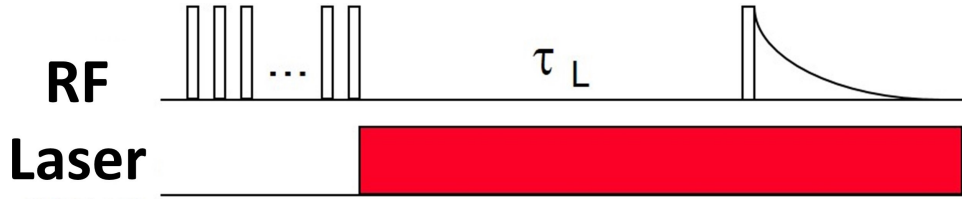


Figure 5.3: Pulse sequence used to obtain OPNMR data. The top RF portion shows a train of saturation pulses followed by a delay (τ_L) before the inspection pulse and acquisition. The bottom laser portion shows the laser is pumping the sample during the τ_L time period, the inspection pulse, and acquisition.

at each OPNMR setup. Each ^{69}Ga and ^{71}Ga spectrum was then fit with a Gaussian line shape in order to extract the area of the peak. We choose to use areas of a fitted function rather than peak intensity to account for any fluctuations in linewidth. The areas of the NMR signals were then plotted as a function of photon energy in an OPNMR profile (Figure 5.4).

The apparent deviation in the profile attributed to the light hole transition [18, 37] was then fit to a Gaussian as a guide to the eye (see Figure 5.4) in order to extract the energy of the peak maximum for this feature as a function of photon energy. Lorentzian and Gaussian fits produce similar results and trends. However, Gaussian line shapes fit the data better which could signify a broadening mechanism at play.

For the polarized PLE experiments at Washington University in St. Louis, photoluminescence from the sample was directed through a PEM (at 50 kHz) and a beam splitter cube. The PEM transformed the circularly polarized light to into either vertically or horizontally polarized light depending on the helicity of the luminescence. In our setup, only the horizontally polarized light is allowed to pass through the beam splitter cube into the monochromator. The PEM switches between converting the $\sigma+$ and $\sigma-$ photoluminescence as horizontally polarized light. The lock-in amplifier uses the PEM frequency of 50 kHz to measures the

difference between the intensities of $\sigma+$ and $\sigma-$ photoluminescence. The difference can be normalized by the total photoluminescence measured by the low pass filter resulting in the percent polarization of the luminescence.

For detecting the PLE, the monochromator was positioned to the low energy side of the luminescence feature (i.e., observe the heavy hole). The signal was averaged for 10 s at multiple excitation energies in order to map out the light hole transition. Similarly to the OPNMR data, the inverted peak which crosses through zero polarization is fit with a Gaussian line shape in order to determine the peak maximum.

5.3 Results and Discussion

5.3.1 OPNMR Profiles as a Function of Magnetic Field

OPNMR profiles were obtained for a region of energies around the expected light hole-to-conduction band transition. The resulting OPNMR profiles notably have resonances with both positive and negative peak amplitudes and concomitant areas. NMR signals for $\sigma-$ were found to be largely positive (“absorptively phased” spectra) except for the region in which the light hole transition appears. Similarly, all of the $\sigma+$ NMR signals were negative (“emissively phased” peaks) except where the transition occurs. The OPNMR profiles from the NHMFL measurements at various fields (4–11.8 T) and the fits to the light hole transition can be seen in Figure 5.4.

In an earlier publication [18], we reported on the inversion through zero intensity and thus a change in the sign of nuclear magnetization when optically pumping at the light hole

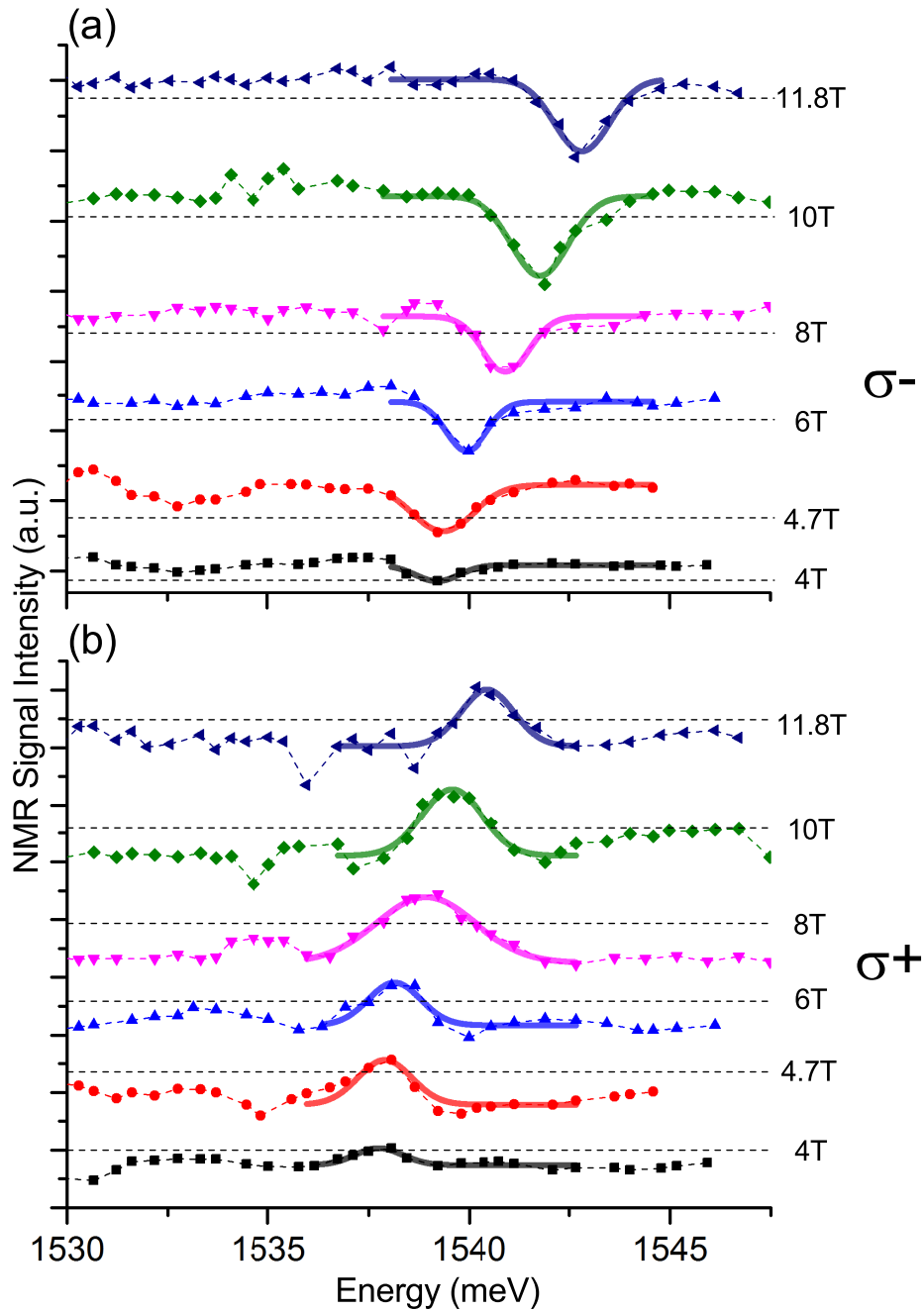


Figure 5.4: ^{71}Ga and ^{69}Ga OPNMR profiles of AlGaAs/GaAs quantum wells at the magnetic fields indicated in the legend (4–11.8 T) for (a) σ^- laser irradiation and (b) σ^+ laser irradiation. All profiles were taken at NHMFL. Profiles are offset for clarity. The black dashed line shows where 0 NMR signal is for each plot. The superimposed Gaussian peak on each plot is meant to be a guide to the eye.

to conduction band transition (hereafter “LH transition”). Through modeling [37], this assignment was confirmed for $B_0=4.7$ T while other fields ($B_0=3.0$ T) are not yet perfectly modeled due to band mixing. We have sought to extend our experiments to additional B_0 fields in an effort to examine the B_0 dependence of this interband transition. The OPNMR profiles extracted from data recorded at NHMFL are depicted for external magnetic fields (B_0) of 4–11.8 T. Figure 5.4a shows these OPNMR profiles with σ^- laser irradiation, and Figure 5.4b are those with σ^+ irradiation. Note the data crossing the black dashed line which indicates zero signal intensity. Superimposed onto each are Gaussian functions fit to the peak where signal inversion occurs, meant to be a guide to the eye. As expected, the LH transition shifts to higher photon energies as B_0 is increased, for both helicities of light. For σ^- irradiation at the LH transition, the magnetization of the OPNMR resonance becomes inverted (or much closer to zero for lower fields), exhibiting negative magnetization. For σ^+ , the opposite is true: once the LH transition is irradiated, the signals adopt the opposite phase, such that the signals exhibit positive magnetization.

In Figure 5.4, the LH transition appears much stronger and thus inverts the nuclei to a greater degree at higher fields. While not quantitative, this trend is notable since higher fields increase the splitting between the energy levels. The combination of quantum confinement (to separate the LH and HH bands) and higher magnetic field could reduce the amount of HH character in the LH band due to band mixing. The same trend has been observed in the Washington University in St. Louis data [18, 37].

5.3.2 Light Hole Transition Field Dependence

Using the peak position of the transition attributed to the LH-to-conduction band, a plot of that transition energy versus external magnetic field has been constructed, shown in Figure 5.5. We include data from both WUSTL (OPNMR and PLE) and from the NHMFL (OPNMR), as indicated in the legend. Notably, data were collected at 4.7 T at both labs, and the OPNMR data show excellent agreement in the LH transition energy, which lends confidence that small differences between equipment types and the resulting measurement have not affected the physical interpretation of the data. Also, both OPNMR and PLE data was acquired at 3 and 4.7 T at WUSTL. The 3 T PLE/OPNMR data matches very well, showing both electron and nuclear measurements of the light hole transition energy lead to the same conclusion. The 4.7 T PLE $\%N$ is much smaller, introducing more error in the determination of the peak maximum.

Circularly polarized light excites transitions only from specific valence band Landau level subbands to the lowest-lying conduction band Landau level. For the LH-to-conduction band transition, σ^- light would originate from the $n = 0$ or $n = 1$ hole Landau level (creating a spin down conduction electron) while the σ^+ light would originate from the $n = -1$ or $n = -2$ hole Landau level (creating a spin up conduction electron) in the Faraday geometry [45]. Consequently, the σ^+ and σ^- transitions will therefore occur at different energies due to dissimilar initial states. The Zeeman interaction also splits the σ^+ and σ^- transitions but in only a linear fashion. More importantly, each transition will also exhibit a dissimilar dependence on magnetic field.

σ^- irradiation shows an approximate linear dependence of the LH transition with respect to the external magnetic field. Such a linear dependence has been observed for high magnetic

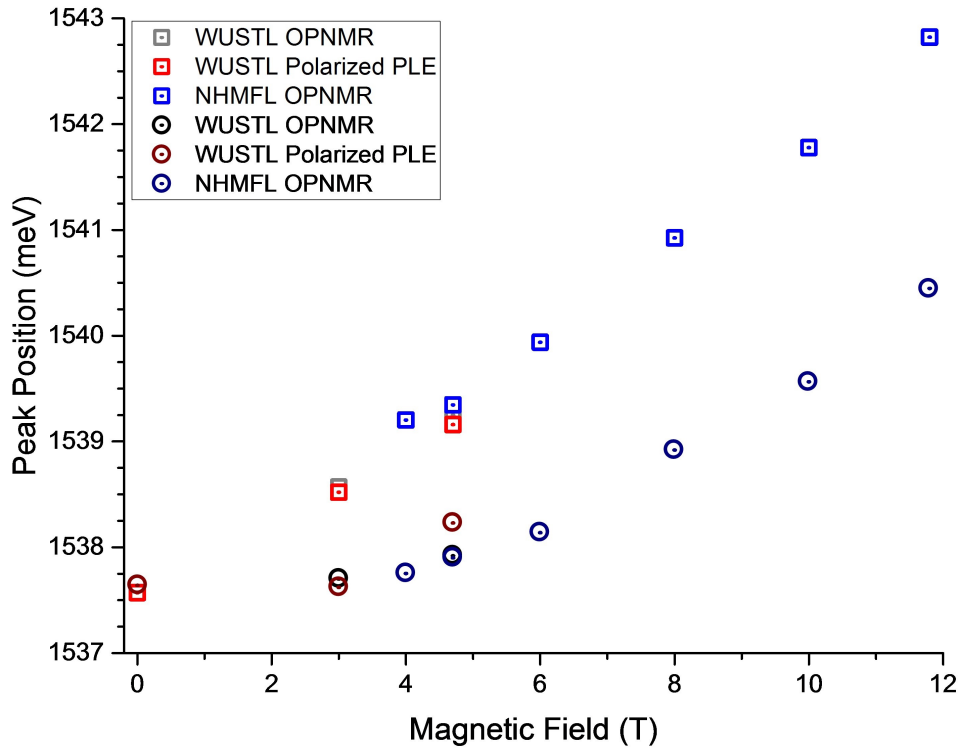


Figure 5.5: Light hole-to-conduction band transition energies for $\sigma+$ (darker circles) and $\sigma-$ (lighter squares) polarized light as a function of external magnetic field. Blue points represent OPNMR data taken at the NHMFL, black/gray points represent OPNMR data from WUSTL, and red points represents PLE data acquired at WUSTL. Overlapping 4.7 T OPNMR data at both locations are shown and demonstrate the consistency of the measurement even with different setups.

fields [46, 47], and similar linear trends have been observed before in reports of calculated and experimental measurements of absorption and photoluminescence data using circularly polarized light [45, 48, 49]. Similarly, $\sigma+$ irradiation also shows a linear dependence at high external magnetic fields ($B_0 = 6-12$ T), but curves to a smaller slope until reaching the zero field energy.

Spin splitting of the conduction band and valence band (light hole) states is expected, and is not equivalent for both helicities. For the conduction band, the subband Landau levels are linear with field, which would not induce any curvature in the transition energy, as it appears in Figure 5.5. In contrast, the valence subband levels do possess curvature. Similar results for field-dependent Landau level transitions have been modeled by Broido [46] and have shown curvature as a function of magnetic field where the onset and sharpness of the curvature depends on the Landau level of the electron and its spin orientation in the magnetic field. Since we are looking at the transition from the valence band light hole state to the conduction band state, we have to take into consideration how the magnetic field affects both bands in order to know the transition energy.

Furthermore, circularly polarized light can only excite from specific valence band Landau levels to the lowest lying conduction band Landau level depending on the helicity of the polarized light and selection rules [45]. Since our final state is the bottom of the conduction band, the allowed light hole transitions for $\sigma-$ and $\sigma+$ light must originate from different Landau levels, causing each transition to now have a dissimilar dependence on the magnetic field.

By plotting the difference in energy of the $\sigma-$ and $\sigma+$ light hole transitions for each field, a non-linear dependence to the magnetic field can be seen. This can be seen in Figure 5.6

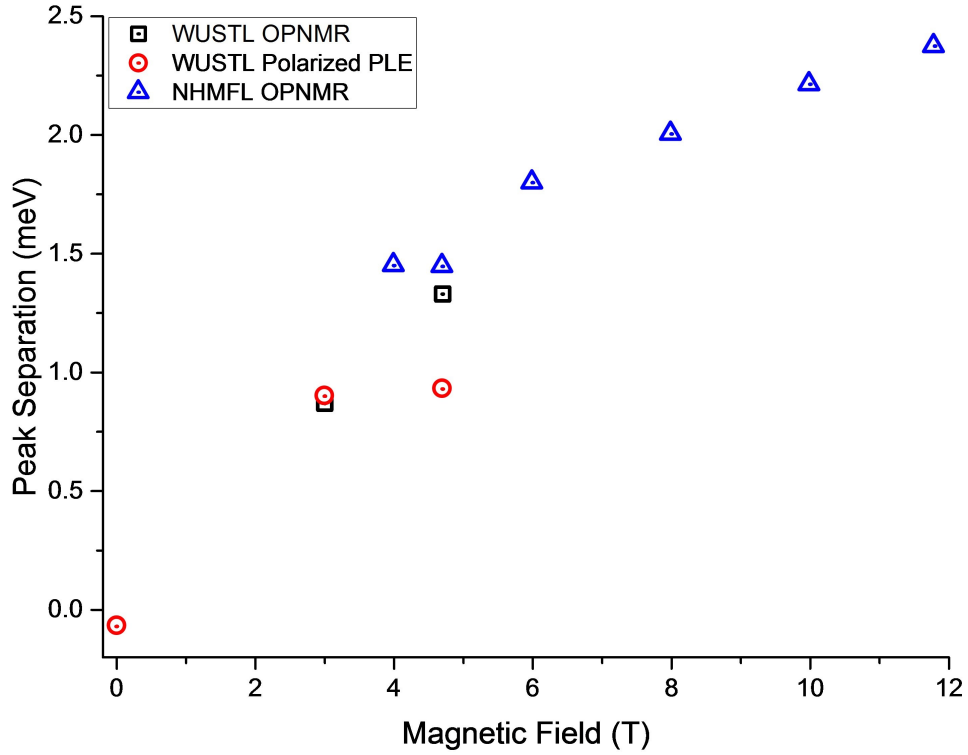


Figure 5.6: Energy difference between the σ^- and σ^+ light hole to conduction band transition as a function of applied magnetic field. The color of the dot represents which set of data produced the difference.

for all three sets of data. Thus, the separation between the two spin states of the light hole transition is not split by a pure Zeeman interaction as previously explained.

Previous calculations for the transition energy do not fit well to the data as seen in Figure 5.7. The bands above the line break are the conduction bands while the bands below the line break are the valence bands. Four valence bands are colored, showing which are the highest energy valence bands to have dominant LH character at our fields. Two bands originate from the light hole and thus initially have light hole character and two originate from the heavy hole and initially have heavy hole character. The bands from the HH and LH end up mixing between 3–6 T where they swap dominant character (i.e., the bands originating from the HH

start with HH character before having a more dominant LH character at higher fields). The allowed transition energies from these valence bands to their respective conduction band can be seen in Figure 5.7b. While the general shape of the calculated transition energies match the data, the zero field LH transition energy and slope of the transition energy as a function of magnetic field are not accurate. Complicated effects, including the Coulombic interaction, may need to be included into the $\mathbf{k}\cdot\mathbf{p}$ perturbation theory of band diagrams to fully model the observed behavior. However, the agreement between three different measurements with unlike equipment lends confidence to the use of OPNMR as a technique to model transition energies at multiple fields.

5.4 Conclusions

In conclusion, OPNMR was used to map out the lowest-energy allowed light-hole transition, resulting in oppositely polarized conduction electrons when compared to other excitation energies. Previous studies were completed on a single setup at two different fields. We were able to reproduce the early results on a completely different OPNMR set-up, showing the robustness of the experiment in measuring transition energies. In addition, a much larger range of magnetic fields were able to be studied in order to help improve theoretical calculations. Comparison to calculation results in the observation of band mixing as a function of magnetic field. The calculations obtain a qualitative match to the shape of the light-hole transition's magnetic field dependence but not for the slope or zero field transition. This can be potentially explained by some perturbation to the band structure not being included, such as the Coulombic interaction.

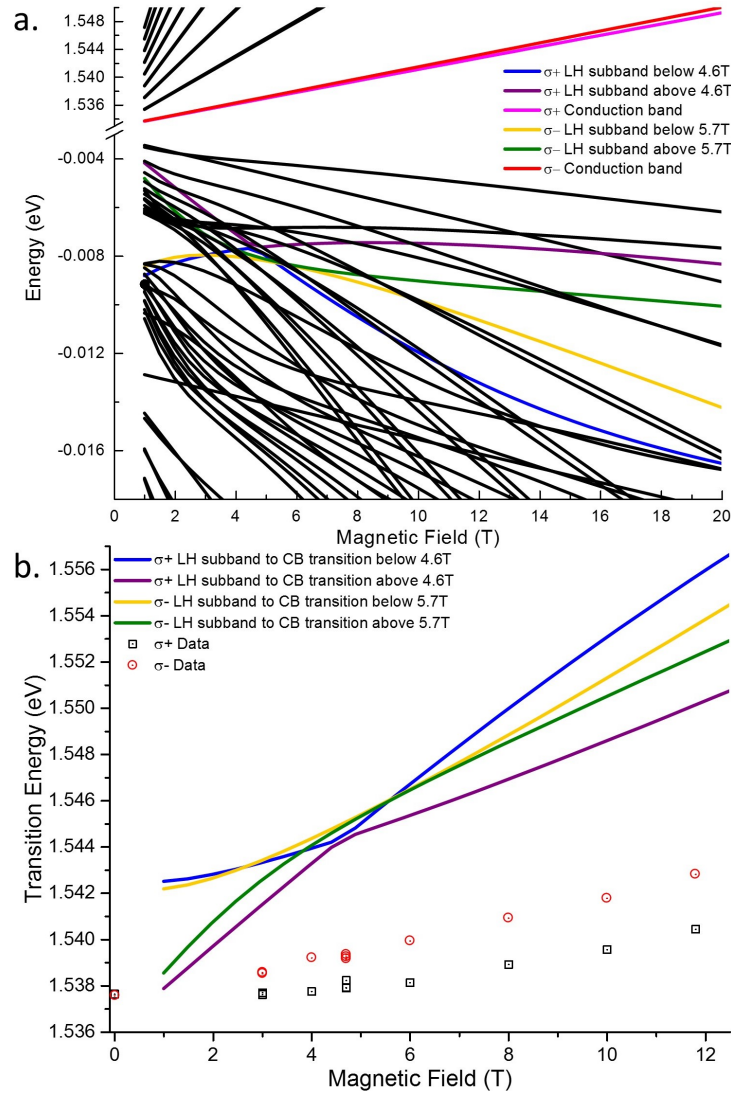


Figure 5.7: Comparison of calculations to the obtained OPNMR and polarized PLE light hole data. a. Calculations of the band energies for all subbands with the those of interest colored. The lowest ($n = 0$) spin split conduction bands are red and magenta. The four highest energy bands with dominant light hole character for our fields are colored blue, purple, yellow and green. The blue and purple valence bands can be excited with $\sigma+$ to the $n = 0$ conduction bands while green and yellow valence bands require $\sigma-$ light. The blue and yellow colored valence bands originate from the light hole and thus have light hole character until mixing with the the green and purple valence bands originating from the heavy hole. After mixing, the dominant band character is swapped. b. The calculated transition energies from the valence bands to their respective conduction bands depending on the helicity of excitation light. The dots represent the OPNMR and polarized PLE data obtained for comparison.

Chapter 6

Optically Pumped NMR of CdTe

6.1 Introduction

OPNMR studies of direct gap semiconductors have primarily focused on GaAs [4, 6, 7, 14, 15, 17, 18, 22, 35, 37, 38, 50, 51, 52], with the second most common material being InP [8, 9, 20, 21, 22, 53, 54]. However, CdTe, a semiconductor of large interest to the solar cell community, has only been reported to be studied by OPNMR twice with opposing conclusions [13, 39]. Leung et al. claims to observe maximum signal enhancement just below the band gap due to direct polarization from the optically oriented electrons. Dong et al. claims to see consistent enhancements for above bandgap excitation with no laser helicity ($\sigma+$ versus $\sigma-$) dependence due to surface spin-dependent recombination. Overall, the trends and mechanisms provided by the two previous studies are in stark contrast with each other, leaving a large uncertainty in the optical pumping of CdTe samples. The goal of this study was to investigate a large variety of CdTe semiconductor samples in order to determine the most common OPNMR profile trends and potentially make sense of the two opposing claims.

6.2 Experimental

6.2.1 CdTe Samples

In total, five different samples of CdTe from two separate manufactures were studied in depth. All five samples were approximately 1–2 mm thick. From the first manufacturer (Marketch), a poly-crystalline high-resistivity sample was studied. From the second manufacturer (University Wafer), two single crystal and two poly-crystalline samples were investigated. Of the two single crystal samples, one was without dopants while the other contained Zn dopants to form $\text{Cd}_{0.931}\text{Zn}_{0.069}\text{Te}$. Of the two poly-crystalline samples from the second manufacturer, one was without dopants while the other contained Zn dopants to form $\text{Cd}_{0.94}\text{Zn}_{0.06}\text{Te}$. The selection of samples allows for a wide array of variables to be studied in an attempt to observe as many possible trends in their OPNMR profiles.

6.2.2 Experimental Methods

While the previous studies primarily focused on the OPNMR profiles and optical pumping properties, in this work, additional experiments including photoluminescence and thermal relaxation were conducted in order to observe other potential differences. All experiments were completed in a magnetic field of 4.7 T with a stable temperature of 6 ± 1 K.

Photoluminescence measurements provide information on the electron energy levels, including dopants and defects. The semiconductors were excited above the band gap where the electron relaxes to the band edge and trap states through coupling with phonon modes. Electron-hole recombination releases a photon with energy corresponding to the separation

in energy of the two charge carriers. The photoluminescence is transmitted to an Acton SpectraPro 2750 monochromator (0.75m path length, triple grating). The energy and intensity of the photons are then measured by an Acton CCD camera.

Nuclear T_1 relaxation measurements were completed using traditional saturation-recovery NMR pulse sequences without the use of the laser. T_1 , or spin-lattice relaxation, measures the rate at which perturbed nuclear spin state populations return to their thermal equilibrium which depends on the lattice temperature. Magnetic field fluctuations, the source of which can be spin-spin interactions, at the Larmor frequency, result in reordering of the populations of each energy level, effectively resulting in transitions between spin states [2]. The thermal equilibrium value of the populations is reached with a time constant of T_1 . Variations in T_1 will provide insight into potential differences in the physics governing the semiconductor sample.

The effect of the pumping time (τ_L) on the NMR signal intensity is studied in order to determine the optimal laser irradiation length to achieve maximum signal enhancements. Using the basic OPNMR sequence (similar to those in Figure 4.6a), τ_L can be varied and the pulse-acquire signal recorded for each time step. Longer τ_L times allow the spin system to approach a steady state, through spin diffusion, where the competing rates of polarization and relaxation become equivalent.

For the OPNMR profiles, each was obtained for multiple photon energies over a region covering below and above the band gap. To obtain the signal area, each spectrum was fit using three Gaussians to account for the splitting in the lineshape due to dipolar and J-coupling of the nearest neighbors [25].

6.3 Results and Discussion

6.3.1 Photoluminescence Measurements

Photoluminescence measurements were performed on the five samples: a. polycrystalline high resistivity CdTe, b. single crystalline CdTe, c. polycrystalline CdTe, d. single crystalline Zn-doped CdTe, and e. polycrystalline Zn-doped CdTe. Circularly polarized light was used to illuminate the sample mounted in the cryostat while the luminescence coming out of the bore of the magnet was reflected into a fiber optic coupler connected to the monochromator. No differences in the spectra were observed for different laser polarizations with the achieved resolution. Laser power was ≤ 100 mW in order to avoid heating of the sample. Excitation energy was ≥ 1.71 eV in order to excite electrons high into the conduction band and eliminate any chance of observing the excitation laser in the spectra. The resulting photoluminescence spectra for all five samples can be seen in Figure 6.1.

At liquid helium temperatures, the band gap energy is 1.606 eV. In addition, the binding energy of an electron-hole pair, or exciton, is known to be 10.1 meV, which can be directly excited to with an energy of 1.5959 eV [55]. The 1.5959 eV energy corresponds to the expected photoluminescence peak energy for a perfect CdTe crystal. In addition, LO (longitudinal optical) phonon modes for CdTe are often observed, with a spacing of 21 meV, which will further complicate the spectra [56]. For the pure CdTe samples (a.-c.), the majority of the photoluminescence peaks occur below 1.5959 eV, indicating the presence of donor and acceptor bound electrons, holes, and excitons as observed previously [56, 57, 58, 59, 60]. Rather than attempt to assign all the peaks in the complicated spectra, comparisons between the spectra and corresponding samples are made.

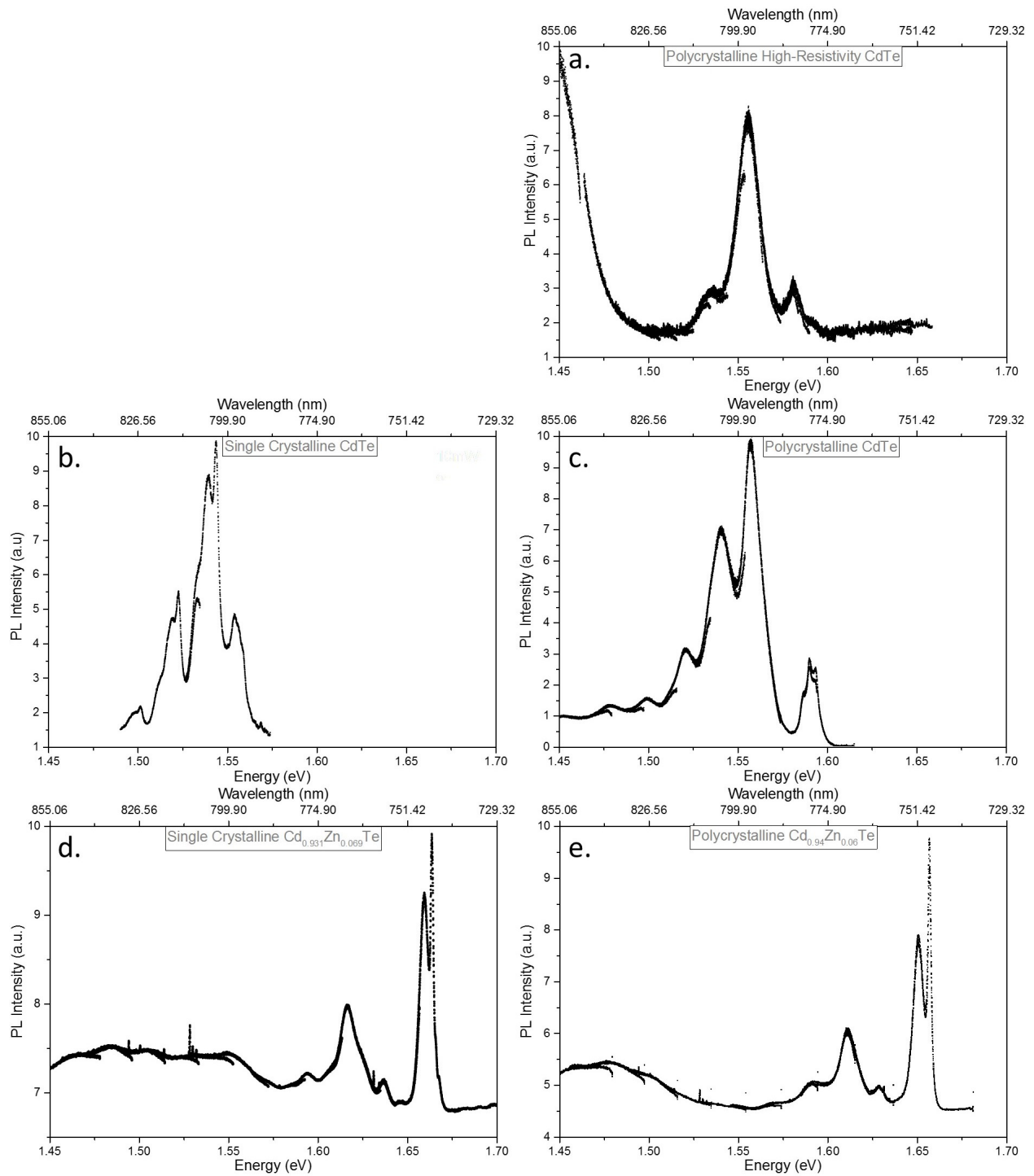


Figure 6.1: Photoluminescence measurements of bulk CdTe samples. The left (b. and d.) are single crystalline samples and the right (a., c. and e.) are polycrystalline samples. Samples d. and e. contain Zn dopants.

The sample with the fewest peaks, a. polycrystalline high-resistivity CdTe, is the only one from a different manufacturer, indicating a likely purity difference between the two manufacturing methods. The large peak growing in at lower energies (< 1.5 eV), can be attributed to the broad defect band observed by others [56, 58] which claim the band to be due to cadmium and tellurium vacancies in the crystal. The two other pure CdTe samples (b. and c.) produce photoluminescence spectra much more complicated attributed to the larger number of peaks. Even though the samples (b. and c.) are from the same manufacturer, different synthesis methods were used in order to form either the single or polycrystalline versions.

For the Zn-doped CdTe samples, higher energy luminescence peaks are observed. The band gap energy increases with the addition of zinc to ≈ 1.64 eV for the dopant levels studied here [56]. Overall, the shape and relative intensities of the photoluminescence peaks is near identical between the single and polycrystalline Zn-doped samples. Thus, the primary difference between the Zn-doped samples appears to only be the crystallinity of the sample; important to note when interpreting data from the other experiments.

Overall, the photoluminescence data shows a large variation in the defects and electron energy structure of the CdTe samples. The differences between the manufacturer and synthesis method ultimately result in different photoluminescence spectra which could explain variation observed in the NMR and OPNMR data discussed below.

6.3.2 Relaxation (T_1) and Optical Pumping Rates

Nuclear T_1 relaxation in semiconductors is typically governed by multiple interactions [61]. The most common relaxation is through thermally excited electrons and holes. However,

due to the low temperatures present in these experiments (6 K), very few charge carriers will be present in the absence of illumination (electrons should be spin-paired in the absence of laser irradiation). Another relaxation method occurs through a spin-rotation interaction between nuclei and moving electrons. This mechanism requires population of phonon modes in the semiconductor which is not present at low temperatures. The dipole-dipole interaction can also lead to relaxation if modulated by motion which will also be frozen out in these experiments. Ultimately, relaxation for these semiconductors will be inherently long at 6 K due to the lack of these mechanisms. The measured relaxation is thus, ultimately, dependent on the amount of dopants, defects, and impurities and other less-known mechanisms. For the five samples, the measured T_1 relaxation time constants are shown in Table 6.1.

Table 6.1: ^{113}Cd T_1 relaxation time constants for CdTe samples at 6 K and 4.7 T.

Sample	a.	b.	c.	d.	e.
Preparation	High Resistivity	Standard	Standard	Zn-doped	Zn-doped
Crystallinity	Poly	Single	Poly	Single	Poly
T_1 (min.)	360	1540	3420	820	2950
Error (min.)	20	300	240	30	550

The relaxation times for the samples show interesting behaviors. The high resistivity sample should be very close to no free electrons or holes, as deemed by the high-resistivity classification. However, even without the presence of free electrons and holes, this sample has the fastest relaxation out of the samples tested. This could be indicative of the dopant used to correct for the intrinsic defects (interstitial and vacancy sites) or the dominant charge carrier in the other samples having a weaker coupling to the nuclei, leading to nuclear relaxation. However, this is difficult to prove as this sample also came from another manufacturer than the other samples. Another trend shows the addition of Zn dopants leads to faster relaxation, even though the dopant would not add charge carriers to the semiconductor. Lastly,

the polycrystalline samples also experienced longer relaxation time constants, indicating that the presence of grain boundaries hinders relaxation for these samples.

Similarly, the optical pumping cross-relaxation rate is governed primarily by the hyperfine interaction and subsequent spin diffusion [12]. The Fermi-contact interaction is believed to be the primary interaction, especially for electrons which become localized as discussed in Section 3.4. Ultimately, faster optical pumping rates are ideal in order to acquire more scans in the same amount of time when implementing OPNMR as a technique for NMR signal enhancement.

Table 6.2: ^{113}Cd Optical pumping time constants for CdTe samples at 6 K and 4.7 T.

Sample	a.	b.	c.	d.	e.
Preparation	High Resistivity	Standard	Standard	Zn-doped	Zn-doped
Crystallinity	Poly	Single	Poly	Single	Poly
T_1 (min.)	9.5	—	267.4	525.0	—
Error (min.)	0.6	—	25.5	36.8	—

In all cases, the optical pumping timescale is much faster than T_1 . This indicates efficient polarization transfer between the electrons and many of the nuclei. Of interest, is that the optical pumping cross-relaxation and spin-lattice relaxation rates do not have the same trends, indicating different mechanisms leading to thermal and optical relaxation. This is not surprising since the optical pumping process creates the charge carriers necessary for many of the relaxation mechanisms mentioned above. The optical pumping time constant was not able to be measured accurately for the standard single crystalline or the Zn-doped polycrystalline CdTe samples due to long optical pumping times needed in order to no longer have a linear dependence.

6.3.3 OPNMR Profile Variability Between Samples

The premise of this experiment was originally to determine which of the OPNMR profiles and mechanisms were the most common in CdTe samples. In order to do this, OPNMR profiles need to be completed on the five samples studied above. However, due to the large variation in optical pumping rates, each sample was optically pumped for different amounts of time (τ_L). While both the standard single crystal and Zn-doped polycrystalline CdTe samples were still in the linear regimes for the optical pumping time, the Zn-doped samples also exhibited a lower signal-to-noise ratio for a reason not understood. This made obtaining a profile for sample e. (polycrystalline Zn-doped CdTe) impossible to measure in a reasonable amount of time. Potentially, the Zn dopants could be hindering the maximum electron polarization, resulting in poorer signal-to-noise ratios. The profiles for the other four samples can be seen in Figure 6.2. The spline fits in the figure are meant to be guides to the eye.

For the experiment, the high resistivity sample (a.) was pumped for the shortest time per scan at 4 min. The two other standard CdTe samples (b. and c.) were optically pumped for 30 min. The single crystal Zn-doped sample was optically pumped for 120 min per scan, limiting the amount of points to be acquired. Two samples, a. polycrystalline high resistivity CdTe and c. polycrystalline CdTe, show a clear laser helicity dependent signal intensity while the other two samples, b. single crystalline CdTe and d. single crystalline Zn-doped CdTe, see very little helicity dependence on the NMR signal. The polycrystalline samples having a larger helicity dependence may be a coincidence, or may be due to grain boundaries present in the polycrystalline sample localizing the electrons and/or affecting the recombination rate of the electrons. In addition, the enhancement for the Zn-doped CdTe shifts to higher energy, likely due to the larger bandgap.

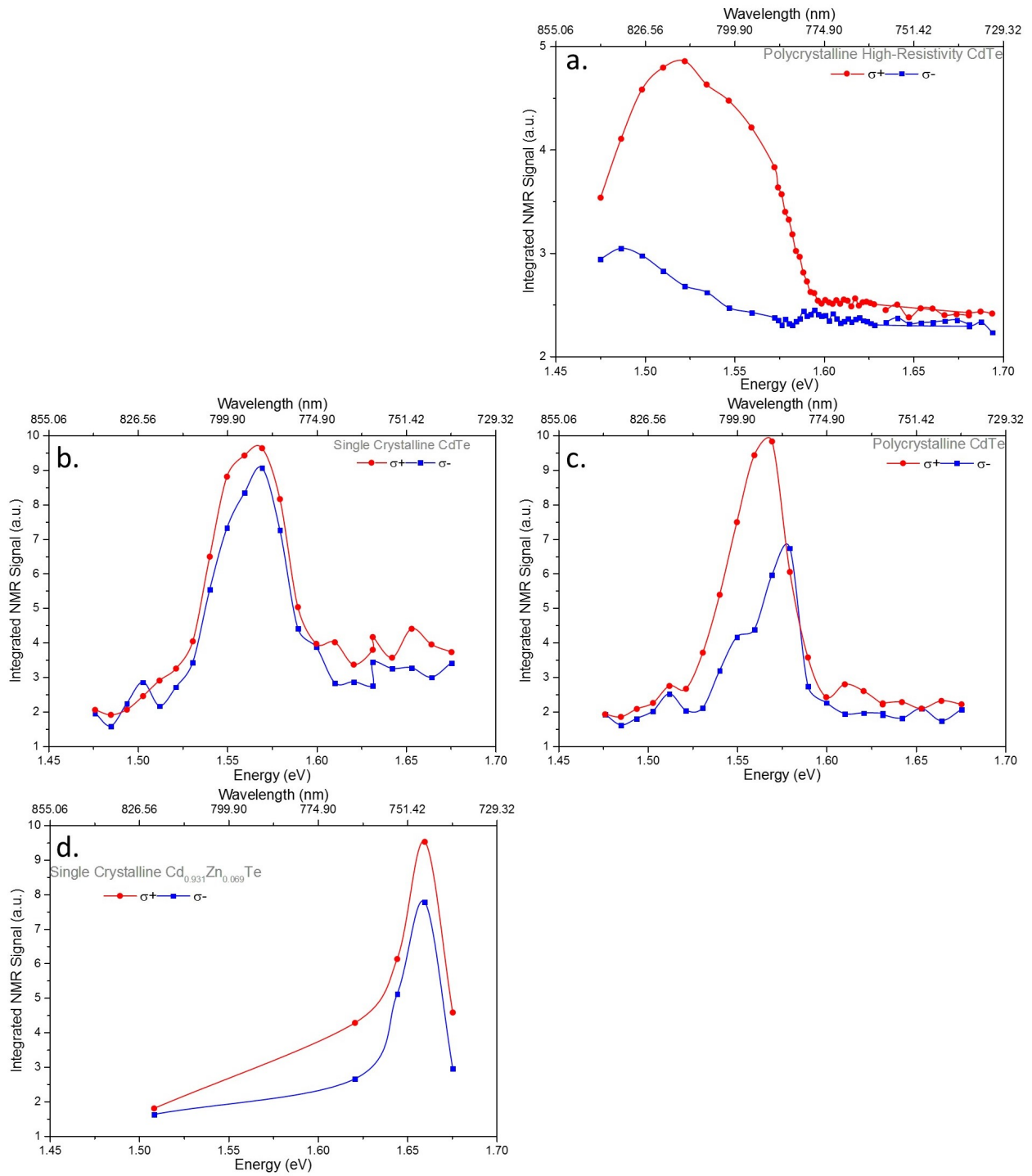


Figure 6.2: OPNMR profiles of bulk CdTe samples. The left are single crystal samples and the right are polycrystalline samples. Samples d. and e. contain Zn dopants. Sample e. was unable to be acquired due to poor signal-to-noise for reasonable optical pumping times.

Of note, all of the acquired profiles show an enhancement peak near the bandgap energy. This is in line with the observations by Leung, et al. [39] but not Dong, et al. [13], where the enhancement was constant above the bandgap energy. However, differences in signal intensity based on the helicity of excitation light are observed in some samples and not in others, indicating the both Leung and Dong were correct about certain aspects of the enhancement profiles.

6.3.4 OPNMR Profile Asymmetries and Enhancements

In order to make more quantitative comparisons between these samples and the previous results, two more complex values will be obtained from the profiles [38]. The first values is the profile asymmetry, A , between the maximum (or minimum) enhancement between the two helicities of light, defined as $I_{\sigma+} - I_{\sigma-}$. A value of 0, where the maximum enhancements are identical in intensity and sign, signifies no helicity dependence on the enhancement, likely indicative of an Overhauser type enhancement [12]. In order to compare between samples with different signal-to-noise ratios, number of scans, irradiation time, and more, the value will be normalized by the smallest signal intensity value. The second value, the offset value (B), is defined as $(I_{\sigma+} + I_{\sigma-})/2$ and will also be taken from the maximum signal enhancements. A larger offset value indicates a larger Overhauser effect, but also needs to be normalized as mentioned above, in hope to compare the samples. These values can be seen in Table 6.3.

One of the main observations from the A and B parameters is the wide range in the values. This could potentially be from using the lowest intensity OP signal, I_{min} , for normalization, which can introduce errors due to experimental differences. Thus, calculating the percent of

Table 6.3: ^{113}Cd OPNMR profile parameters for CdTe samples at 6 K and 4.7 T.

Sample	A_{max}	B_{max}	I_{min}	Norm. A	Norm. B	% A
Leung [39]	0.97	1.51	0.06	16.2	25.2	39%
Dong [13]	0.00	3.29	1.55	0.00	2.12	0.0%
a. High Resistivity Polycrystalline	1.81	3.95	2.30	0.79	1.72	31%
b. Standard Single Crystal	0.58	9.35	1.58	0.37	5.92	5.9%
c. Standard Polycrystalline	3.10	8.28	1.61	1.93	4.29	31%
d. Zn-doped Single Crystal	1.75	8.65	1.62	1.10	5.34	20%

enhancement due to the A parameter will be a more accurate way to compare the samples. To understand the two values, the steady-state electron polarization equation (Equation 3.6) must be interpreted using these parameters. Once again, the expression for the steady-state expectation value (proportional to signal enhancement) is [12, 36]

$$\langle S_Z \rangle_{\sigma\mp} = \frac{\langle S_Z \rangle_0}{1 + \frac{\tau_e}{T_{1e}}} + \frac{S_0}{1 + \frac{T_{1e}}{\tau_e}}. \quad (6.1)$$

The A parameter is related to the difference between the helicities of the light which requires long T_{1e} values to be dominant, to maintain the instantaneous polarization from the optical excitement, as shown in the first part of the equation. The B parameter is related to saturation of the electrons, leading to an Overhauser type enhancement, which requires the excited electrons to approach their thermal equilibrium quickly compared to the recombination time, τ_e , as shown in the second portion of the equation. By comparing the percent of the A parameter leading to enhancement between the samples, it is clear the samples studied here best represent the work completed by Leung, et al. [39].

6.4 Conclusions

A variety of CdTe samples were studied with OPNMR in an attempt to understand the dominant mechanisms leading to enhancement. Two previous studies had been completed on CdTe via OPNMR, resulting in contradicting data. By comparison, the shape of the OPNMR profiles obtained matched the data obtained by Leung, et al. [39], who explained the results using the standard OPNMR theory with maximum enhancements near the band gap energy as discussed in Chapter 3. In addition, analysis of the enhancement profile asymmetry and offsets indicate a competing mechanism between optical orientation and saturation of electron spins, with saturation being slightly more favored. This would indicate an electron relaxation rate and electron-hole recombination rate of similar time scales. Even small changes in the rates would produce rather large changes in the percent of enhancement from electron orientation versus saturation. However, even extreme changes in these time scales is not expected to produce constant above gap enhancement as observed by Dong, et al. [13] due to the changing laser penetration depth as a function of photon energy. Dong claims their differing results to be due to “spin-dependent recombination via shallow paramagnetic centers near the sample surface” which may be due to poor sample growths and surface treatments.

Chapter 7

Characterization of Isolated

^{113}Cd – ^{125}Te Nuclear Spin Pairs in

CdTe Using Optical Pumping

A continuation of the CdTe studies of the previous chapter, lead to the observation of interesting spin dynamics in CdTe. The results were obtained on the the high resistivity sample due to the faster optical pumping time constants and the larger signal-to-noise ratio, allowing more complex experiments to be completed for the first time on CdTe. In collaboration with the postdoctoral associate partially on the optically-pumped NMR projects (Dr. Zayd Ma), the spin dynamics of isolated spin pair under optical pumping conditions were studied.

7.1 Introduction

Quantum information processing is ultimately limited by fluctuations perturbing carefully prepared quantum states, and efforts are underway to find a system with long relaxation

times [62]. Electrons in semiconductors are attractive because the states are easily prepared, manipulated, and detected via optics and electron spin resonance [63, 64]. However, the relaxation times are prohibitively short for excited electrons, and schemes have been devised to use long-lived nuclear spins to process information instead [65, 66, 67]. Nuclear spin states have much longer relaxation times than that of electron spins (usually ≥ 3 orders of magnitude [31]), but can be much more difficult to access, prepare, and observe. In addition, A. Goto, et al. [68] have claimed to observe incident photons at or near the band gap of having the ability to tune nuclear-nuclear coupling strengths in GaAs via OPNMR and cross-polarization dynamics, making OP of interest to the quantum computing community.

Optically-pumped NMR of semiconductors [12] can overcome many of these issues. This technique results in a highly polarized nuclear spin bath with the nuclear spin orientation selected optically. OPNMR is typically performed at temperatures of 4–10 K which, depending on the system, can push nuclear spin-lattice relaxation time constants to well over tens of minutes to multiple hours. The longer spin-lattice relaxation times at these temperatures, while beneficial to quantum computing, require the use of OPNMR to quickly initialize and polarize the nuclear spin system.

The physical properties that can shift or broaden an NMR signal are diverse [69], but the mechanisms most relevant to this experiment are nuclear spin-spin scalar J -couplings, anisotropic J -couplings (i.e., pseudo-dipolar), and through-space dipolar couplings. If a ^{113}Cd has a ^{125}Te isotope directly bonded to it, the ^{113}Cd NMR resonance frequency will be affected by both dipolar and J -coupling interactions to this ^{125}Te . The resultant change to the ^{113}Cd resonance can be to either a higher or lower frequency depending on whether the ^{125}Te magnetic moment ($S = 1/2$) is aligned parallel or anti-parallel to the applied magnetic field. In solid samples, even without quadrupolar broadening, the NMR splitting due to

J -coupling is typically unresolvable because the dispersion in local magnetic fields due to randomly oriented dipole-coupled nuclei in close proximity (dipolar disorder) will dominate all other broadening mechanisms. However, ^{113}Cd , ^{111}Cd , and ^{125}Te are relatively rare isotopes (12.26 %, 12.75 %, and 6.99 %, respectively), making the spin bath dilute enough for narrow NMR resonances, allowing the coupling between ^{113}Cd and ^{125}Te nuclei in ^{113}Cd - ^{125}Te spin pairs to be resolved.

The spin-spin coupling between a ^{113}Cd and ^{125}Te will shift the ^{113}Cd NMR resonance frequency by [25]

$$\Delta\nu = [J_{iso} + (D - J_{aniso})(1 - 3\cos^2\theta)]S_z, \quad (7.1)$$

where $D = (\mu_0/8\pi^2) \times (\gamma_{\text{Cd}}\gamma_{\text{Te}}\hbar/r^3)$ is the direct dipole coupling, θ is the angle between B_0 and the internuclear axis, and J_{iso} and J_{aniso} are the indirect (through-bond) scalar and anisotropic interactions, respectively [25]. The through-space dipolar interaction is due to direct dipole-dipole coupling to both nearby homonuclear and heteronuclear magnetic moments, while J -couplings (both scalar and anisotropic) are due to hyperfine coupling of bonding electrons and nuclei [70]. In CdTe, the ^{113}Cd - ^{125}Te dipolar and J -couplings have been measured previously [25] with results in good agreement with the data presented here. The previously reported values also demonstrated that the two contributions to the observed total spin-spin coupling (dipolar coupling and J -coupling) can be of the same order, depending on crystal orientation, and therefore, neither can be neglected.

Even with resolvable spin-spin coupling, the ^{113}Cd NMR signal is complex since all ^{113}Cd nuclei, including those with only NMR-inactive (nuclear spin, $S=0$) neighbors, are excited. To select (“filter”) only the contribution from directly-bonded ^{113}Cd - ^{125}Te spin pairs, we used the well-established technique of static (without sample spinning) cross-polarization (CP) [71]. Heteronuclear CP is induced by applying simultaneous B_1 fields (radio-frequency

excitation magnetic fields) at the Larmor frequency of each isotope, with the magnitude of each B_1 field set so the nutation frequency of each is identical, the Hartmann-Hahn matching condition [72] ($\gamma_N^{(1)} B_1^{(1)} = \gamma_N^{(2)} B_1^{(2)}$). Matching the nutation frequencies allows energy to exchange between spins that are coupled and results in a transfer of magnetization from one spin to the other. The focus of the measurements presented in this article are on the CP dynamics of isolated spin pairs of ^{125}Te and ^{113}Cd and the opportunity to probe such pairs in relative isolation, owing to the low abundance of these isotopes (as discussed below).

Cross-polarization dynamics in solids have been studied extensively [73] which typically assumes abundant spin reservoir for energy to transfer from, when using a thermodynamic approach. Oscillations in CP dynamics were first observed in 1969 [74]. The oscillations occur as the spin coherence between the spins oscillates in a two-spin system, where the oscillation frequency is set by the magnitude of the spin-spin coupling strength. In a truly isolated spin pair, the oscillations would persist indefinitely [43]. However, in real world systems studied to date, the oscillations decay due to spin diffusion [43, 75], molecular diffusion [76], and averaging over different crystal orientations (for non-scalar interactions) [23, 77].

The use of heteronuclear scalar spin-spin coupling (J -coupling) in cadmium telluride has been proposed for use as a quantum gate by Shimizu *et al.* [78]. However, there has been no experimental demonstration of $\text{Cd} \leftrightarrow \text{Te}$ couplings under optical pumping conditions, whereas changes in couplings have been observed in GaAs, previously [68]. In this chapter, the ability to directly excite and monitor the dynamics of “isolated” spin-pairs in CdTe with optical pumping at 6 K is demonstrated. In addition, the spin-pairs are characterized in order to determine their ability to be used in spintronic and quantum computing applications.

7.2 Experimental

Experiments were performed on crystalline CdTe purchased from Marketech International, designated as high resistivity. The sample has 99.999% purity and was grown by the Bridgeman method with a Cd reservoir. X-ray diffraction has shown the crystal to be primarily biphasic with two domains: the surface normal vector is along the [111] growth direction, and the two domains are related by a rotation about this surface normal vector.

The sample was irradiated with a continuous wave irradiation at $\lambda = 805$ nm (photon energy, $E_{ph} = 1.540$ eV) from a Ti:Sapphire ring laser (Coherent 899-21) pumped by a 10 W solid-state diode laser (Spectra Physics Millennia X). The $E_{ph} = 1.540$ eV pumping light was chosen to be slightly less than the bandgap energy, E_g [12], as it gives the maximum enhanced NMR signal and also penetrates the sample deeply (so as to irradiate spins throughout the entire sample) [39]. The spectral linewidth of the Ti:Sapphire laser is ≈ 30 MHz (not frequency locked) with a spot diameter of ≈ 2 mm. Output of the laser is linearly polarized, and was converted to circularly polarization with a $\lambda/4$ plate centered at 790 nm as the final optical element before the cryostat window. The output power of the laser was adjusted with a $\lambda/2$ plate followed by a beam splitter cube. Laser access to the sample was controlled with a mechanical shutter (rise/fall time of 2 ms) synchronized to the NMR pulses with TTL pulses from the NMR spectrometer.

Nuclear spin excitation and detection was performed on a home-built doubly resonant (^{113}Cd at 44.406 MHz and ^{125}Te at 63.077 MHz) NMR probe (Section 4.4). The probe was housed in a helium recirculating Janis cryostat (Janis-SHI 950), and NMR data were acquired with an Apollo (Tecmag) spectrometer. The sample chamber temperature was maintained with

a Lakeshore temperature controller at 6 K. Nuclear excitation magnetic field (B_1) strengths ranged from 15–25 kHz.

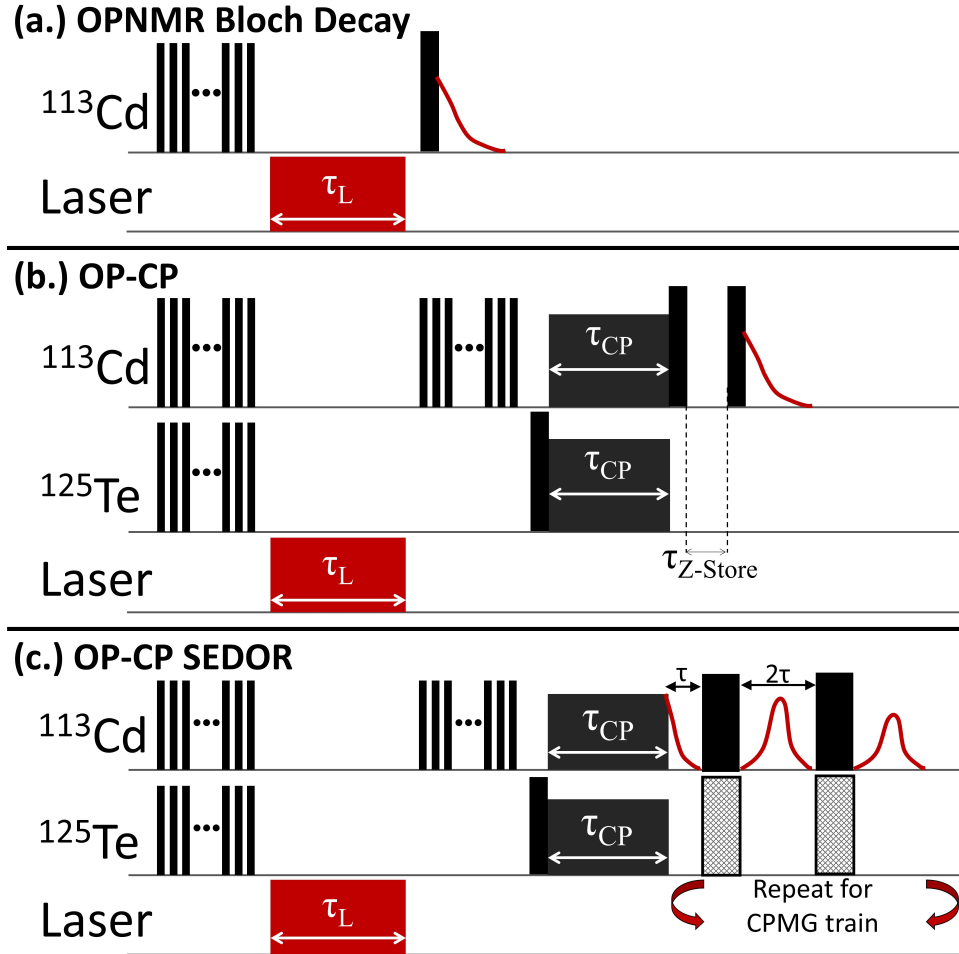


Figure 7.1: OPNMR pulse sequences used to study the CdTe sample. The x -axis is time (not to scale). Saturation pulse trains are shown with the middle pulses in the train denoted by ellipses (\cdots). In each, the laser pumping time (τ_L) is shown, after the initial saturation and before the NMR sequences for the light-off experiments. (a.) The standard optically pumped NMR sequence implementing a Bloch decay sequence. (b.) Optically-pumped-cross-polarization (OP-CP) pulse sequence for static cross-polarization (CP) from ^{125}Te to ^{113}Cd . The ^{113}Cd are cross-polarized from the ^{125}Te nuclei for a time of τ_{CP} and are then stored along the the external magnetic field for a period of $\tau_{z\text{-store}}$. (c.) OP-CP SEDOR sequence ($\tau = 100\ \mu\text{s}$ shown here) using XY-8 ($xyxy\ yxyx\ \bar{x}\bar{y}\bar{x}\bar{y}\ \bar{y}\bar{x}\bar{y}\bar{x}$) phase cycling for the coincident π pulses, leading to accurate measurement of the spin pair coupling strengths.

A standard OPNMR sequence employs a Bloch decay pulse sequence and can be seen in Figure 7.1(a.). The sequence begins with a saturation comb on nuclei of interest before laser polarization occurs for a period of τ_L . τ_L was 15 minutes for all OP experiments in this chapter. The excited electrons can then relax back to the valence band with the light off starting 1 s before acquisition. Figure 7.1(b.) shows the pulse sequence (optically-pumped-cross-polarization, OP-CP) used to optically pump and cross-polarize only the directly-bonded nuclear spin pairs. A typical cross-polarization sequence using the Hartmann-Hahn matching condition was inserted where the tipping pulse is a 90° pulse (on ^{125}Te) and the contact time (τ_{CP}) can be varied. The spins were stored along the z -axis (“ z -store”) for 15 ms to allow the preamplifier electronics to recover from the high-power and relatively long contact pulses. The T_1 of the sample was ≈ 6 h at these experimental conditions, making the effect of the z -store delay negligible. After cross-polarization, the ^{113}Cd magnetization is detected with a Bloch decay sequence or a spin-echo double resonance (SEDOR) echo train. In Figure 7.1(c.), a variant of a SEDOR experiment is shown, using a CPMG train during the acquisition [79]. For this experiment, a 200 μs delay between the coincident 180° pulses and XY-8 phase cycling [80] were implemented on both the ^{113}Cd and ^{125}Te channels. The ω_{RF} 's of the two channels are separated by an approximate 3 kHz with a FWHM ≈ 700 Hz matching condition. It is important to note that due to the coincident refocusing pulses, transient Hartmann-Hahn CP matches may occur during pulse build-up and decay, but is unlikely to noticeably change the results due to the short contact times and narrow matching condition.

7.3 Results and Discussion

7.3.1 OPNMR Cross Polarization

Direct detection of ^{113}Cd after optical pumping can be performed to detect all ^{113}Cd present, not just those close to ^{125}Te . This is achieved by an OPNMR sequence with Bloch decay detection of the ^{113}Cd as often employed [12]. In the resulting spectrum, we observe a central resonance flanked by two satellite peaks (Figure 7.2, black). Conventional NMR without optical pumping yields no signal at 6 K owing to the need to signal average and the prohibitively long T_1 times. The resulting spectra from the $^{125}\text{Te} \rightarrow ^{113}\text{Cd}$ OP-CP pulse sequence (contact time, $\tau_{CP} = 1$ ms) can be seen in blue. The spectrum is plotted in Hz to display the size of the splittings. Only the satellite peaks are detected using the OP-CP sequence at this (shorter) contact time. By transferring the magnetization from ^{125}Te to ^{113}Cd and observing the ^{113}Cd , we have selected only those ^{113}Cd nuclei in ^{113}Cd - ^{125}Te spin pairs. Furthermore, these spin pairs are highly isolated from other pairs since only 22.5% of the 12.3% naturally abundant ^{113}Cd atoms are in a ^{125}Te - ^{113}Cd spin pairs (74.8% of the Cd atoms do not have a single ^{125}Te neighbor). While the $T_{1\rho}$ of ^{125}Te was not explicitly measured, it is likely longer than 25 ms since no signal decay is observed of the satellite intensities in the CP curve (discussed later). The RF amplifiers limit the pulse lengths obtainable, setting a maximum on spin-lock length possible in a $T_{1\rho}$ measurement, making it impossible to measure $T_{1\rho}$ and make any comparisons to T_1 .

Such ^{125}Te - ^{113}Cd pairs are at an average distance of $\approx 13.4 \text{ \AA}$ from one another in the zincblende structure – a long distance compared to the Cd-Te bond length of 2.8 \AA . The

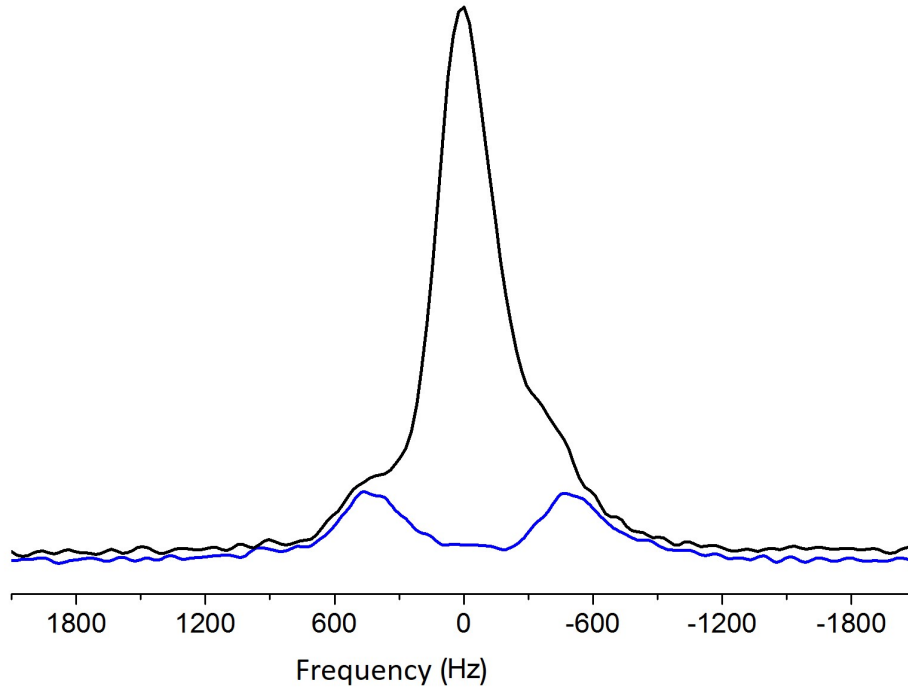


Figure 7.2: ^{113}Cd OPNMR Bloch decay spectrum (black), and ^{113}Cd - ^{125}Te OP-CP (blue) spectrum. The OP-CP spectrum was recorded for $\tau_{\text{CP}} = 1$ ms. Laser irradiation for the τ_{L} period was with $\sigma+$ light for 15 min for both. 0 Hz is on resonance with the ^{113}Cd pulses.

average separation of the spin pairs was calculated by dividing the total volume of an expanded “unit cell” (of 100 Te and 100 Cd atoms, 680 nm^3) by the expected 2.8 ^{113}Cd atoms¹ in a ^{125}Te - ^{113}Cd spin pair to find the average volume and therefore average separation distance of these ^{113}Cd - ^{125}Te spin pairs. If the lone ^{113}Cd and ^{125}Te atoms could be decoupled efficiently, the remaining spin system will primarily be isolated, strongly-coupled spin pairs. At short contact times, only the ^{113}Cd that are closely coupled to ^{125}Te are apparent, since the strong coupling between the two nuclei results in a fast CP build-up. At longer contact times, contributions from farther ^{125}Te can possibly be seen. The Bloch decay spectrum in

¹ $P = \left(\frac{n!}{k!(n-k)!}\right) p_{^{125}\text{Te}}^k (1 - p_{^{125}\text{Te}})^{(n-k)} * p_{^{113}\text{Cd}}$ where $n=4$ bonded atoms, p_X is the natural abundance of isotope X , and $k=1$ for a single ^{125}Te neighbor out of the 4 directly bonded atoms, (i.e., a spin pair).

Figure 7.2 is a combination therefore of both ^{125}Te -split species and unsplit ^{113}Cd that is more distant from the ^{125}Te spins.

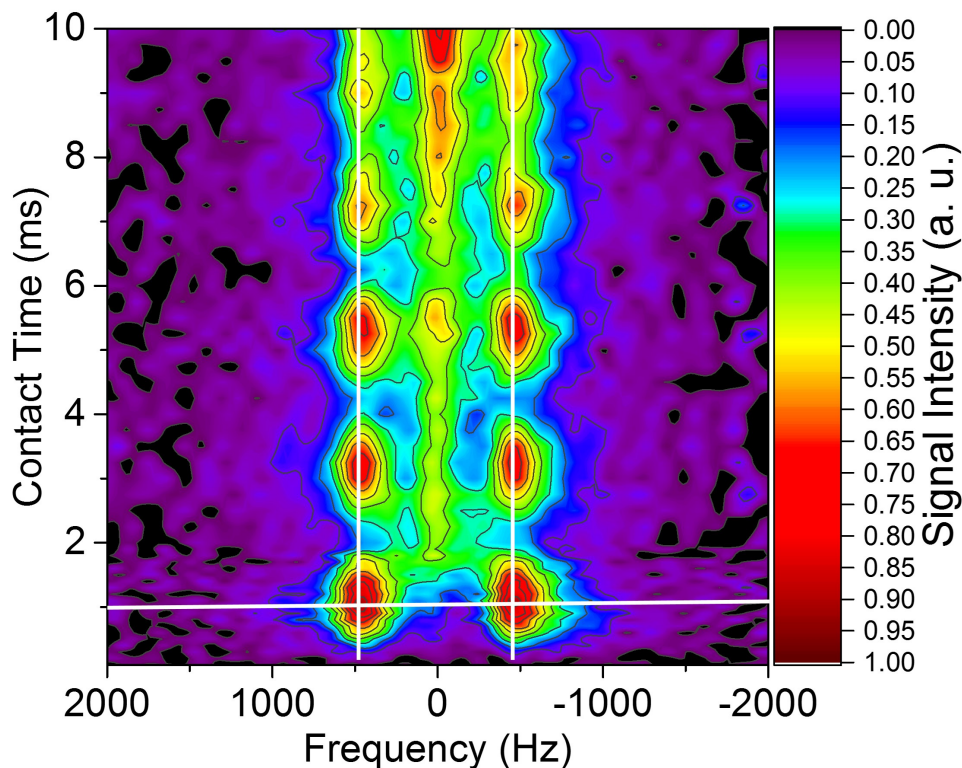


Figure 7.3: ^{113}Cd OP-CP NMR data with contact time along the vertical axis and NMR frequency along the horizontal axis. 0 Hz is on resonance with the ^{113}Cd pulses, and contours denote the intensity of the signal. The horizontal white line corresponds to the blue OP-CP spectrum in Figure 7.2. The vertical white lines correspond to slices shown in Figure 7.5.

In order to probe that coupling between ^{113}Cd and ^{125}Te , the contact time can be incremented in the OP-CP experiment. Figure 7.3 is a contour plot of the ^{113}Cd OP-CP NMR plotted as contact time versus frequency (0 Hz indicates “on resonance” with the ^{113}Cd pulses). Due to the spectrally-resolvable splittings due to dipolar and J -couplings in CdTe, we observe several complete oscillations of cadmium directly bonded to tellurium. The J -coupled satellite peaks are centered at approximately ± 500 Hz, and a 1-dimensional horizontal slice at $\tau_{CP} = 1$ ms is the spectrum shown in Figure 7.2 (in blue). The central peak, denoting ‘lone’ ^{113}Cd , has a

much slower CP build-up as seen in contour plot, indicating a much weaker coupling strength to ^{125}Te atoms as expected. The shape of the growth does not match current CP build-up models and contains multiple features. The initial rate of the central peak growth has a time constant of 1.85 ms as shown in Figure 7.4. This is likely due to the weaker coupled ^{125}Te - ^{113}Cd spin pair as discussed later and in Figure 7.6. However, a sharp rise in the area of the central peak occurs at ≈ 15 ms, which is not able to be modeled.

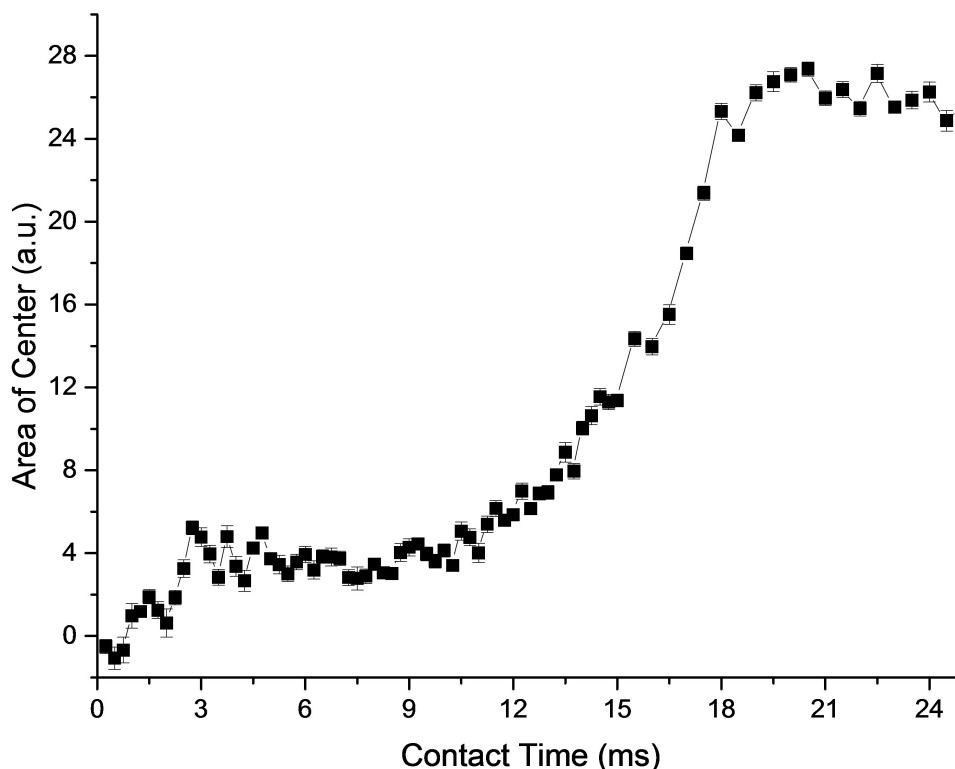


Figure 7.4: ^{113}Cd OP-CP NMR vertical slices of data at the frequency of the central peaks as a function of contact time with ^{125}Te .

The satellites oscillate in intensity with respect to contact time. The intensities are best viewed as vertical slices (plotted in Figure 7.5), and oscillate with respect to contact time with a period of 534 ± 6 Hz, when fit with an exponentially-decaying sine wave. The ^{113}Cd magnetization oscillates during the CP contact time with one-half the difference in frequency between the J -coupled peaks, and the oscillations die out due to the coupling of the spin

pair to neighboring nuclei with non-zero spin. However, the oscillations persist much longer (decay to equilibrium around 10 ms) than in other solid materials, where the longest found was ^{113}In - ^{31}P in InP with oscillations decaying to equilibrium around 4 ms under decoupling and magic-angle spinning conditions [81]. For this present CdTe experiment, the predominant mechanism contributing to decay of the signal is coupling to spins outside the directly bonded spin pair. The oscillations decay as a function of contact time to a value $\approx 1/2$ of the maximum amplitude, contrary to many dipolar oscillation results in the literature that treat CP dynamics to include spin diffusion [73] to a spin bath with infinite temperature. This likely indicates the polarization is still present in the spin pairs, but becomes evenly split between the ^{113}Cd and ^{125}Te , rather than oscillating between the two nuclei. The convergence of the oscillations on the value of $\approx 1/2$ is also consistent with calculations of an isolated spin pair on a molecule which does not have enough time to exchange its energy with the lattice (in the model, undergoing restricted diffusion) [76].

The satellite peak splitting and the frequency of the oscillations depend on the net coupling strength between the two nuclei. As shown by Nolle [25], the net heteronuclear coupling strength in CdTe is comprised of dipolar (D), isotropic J (scalar), and anisotropic (pseudo-dipolar) J -couplings (which have the same angular dependence as dipolar interactions). Equation 7.1 shows that both the dipolar and anisotropic terms depend on the angle between the internuclear axis and the external magnetic field (B_0). Since CdTe has a zincblende crystalline structure (confirmed by x-ray diffraction on the sample), and we know the growth direction of our semiconductor, the various angles θ between B_0 and the Cd-Te internuclear axes can be calculated (Figure 7.6).

B_0 is aligned with the crystal growth direction, and the magnetic field vector is aligned with one of the bonds and splits the other three internuclear axes at an angle of 70.53° . Given

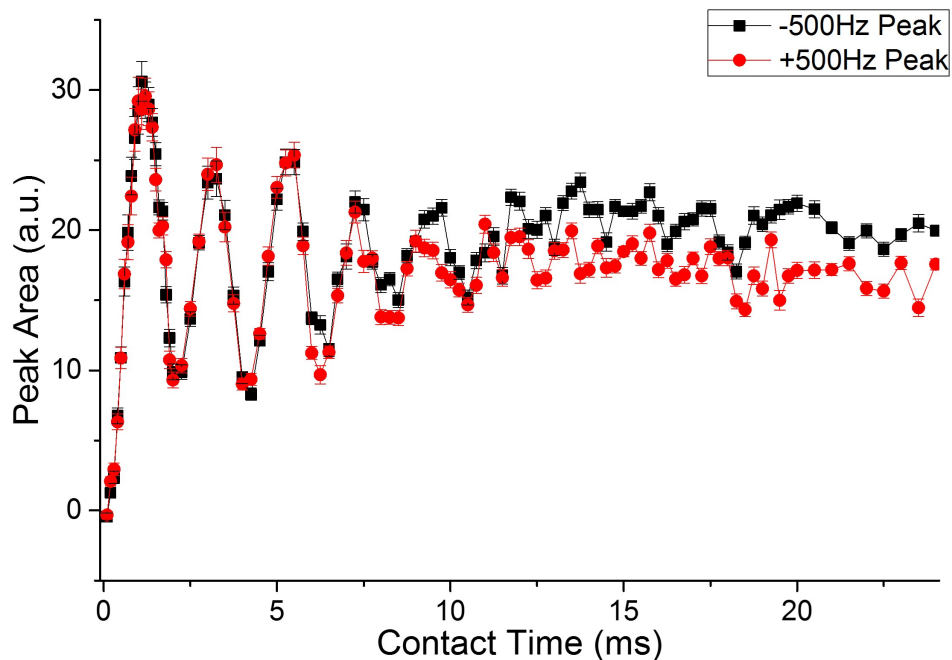


Figure 7.5: ^{113}Cd OP-CP NMR vertical slices of data at the frequency of the satellite peaks as a function of contact time with ^{125}Te (shown as vertical white lines in Figure 7.3). Black squares correspond to the lower frequency satellite peak while the red circles are the higher frequency satellite peak.

the orientation-dependent splitting reported previously for J_{iso} (655 ± 60 Hz) and $D - J_{aniso}$ (490 ± 50 Hz) [25], the calculated splittings are 960 Hz for the 3 pairs at 70.53° and -320 Hz for the Cd-Te pair at 180° (Equation 7.1). Therefore, the 3 bonds trisected produce the observed satellite peaks, while the bond aligned along the field, with one quarter of the total satellite intensity, would appear near 0 Hz. The peaks at ± 480 Hz are clearly observable in the OP-CP experiments, and while peaks at ± 160 Hz would be expected, they are likely not observable in the short contact time cross-polarization experiments due to being only one out of every four ^{113}Cd - ^{125}Te spin pairs and the three times weaker coupling strength (slower CP build-up). The first maximum of the central peak (≈ 3 ms) aligns well with the first maximum of the satellite peaks (≈ 1 ms), for a three times weaker coupling strength, and thus, corresponding to the ^{125}Te - ^{113}Cd spin pairs oriented along the magnetic field.

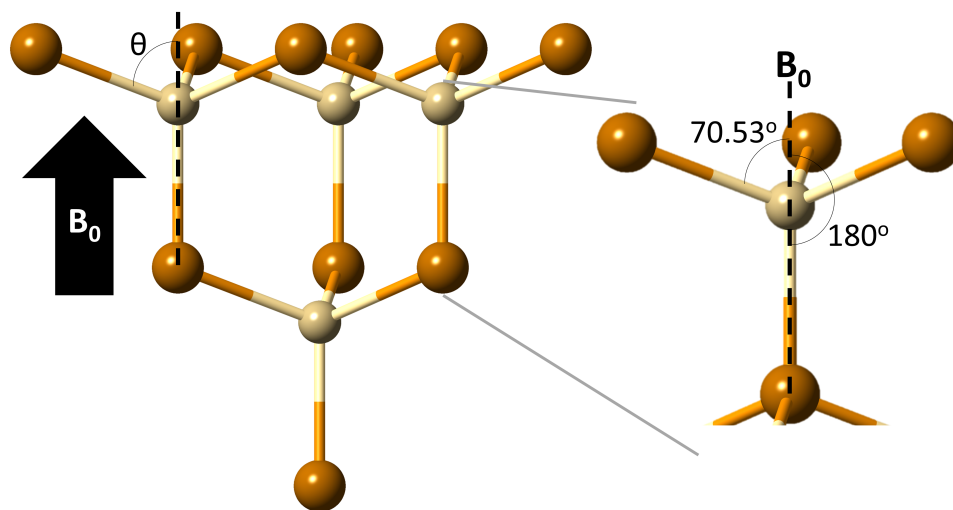


Figure 7.6: CdTe structure with important angles noted. B_0 is oriented along the $[111]$ crystal axis. Cadmium atoms are colored white and tellurium atoms are orange. Each cadmium and tellurium are tetrahedrally coordinated with all interatomic angles at 109.47° . Each cadmium is coordinated to four telluriums, three at 70.53° with respect to B_0 and one at 180° .

7.3.2 OPNMR SEDOR Experiments

To confirm the cross-polarization measurements, two ^{113}Cd - ^{125}Te time-domain OP SEDOR NMR sequences (one which uses cross-polarization between ^{125}Te and ^{113}Cd nuclei) were performed as a second independent measurement of the ^{125}Te - ^{113}Cd coupling strength. The sequence implemented a variant of SEDOR employing a CPMG pulse train separated by acquisitions, as proposed by C. P. Slichter in 1996 [79], rather than the conventional incrementing of the echo time on the S -spins developed by E. L. Hahn [82]. This experiment has not been experimentally reported, to the best of our knowledge, likely due to the fact that it is extremely rare to find systems with observable isolated spin pairs probed in static conditions. SEDOR compares two different nuclear precession signals (S and S_0) where the only difference between them is to reintroduce the heteronuclear spin-spin interactions (here

the dipolar and J -interactions, including the pseudo-dipolar), with 180° pulses on the unobserved nuclei simultaneously with the 180° pulses of the CPMG train of the observed nuclei for the S signal. Here, we have implemented a series of 180° pulses with the transverse ^{113}Cd magnetization recorded between each pulse [79]. For suitably isolated spin pairs, the dipolar dephasing will be apparent in this “echo train”.

Figure 7.1(c.) shows the more complicated pulse sequence used (with CP), with the more simple version using a 90° pulse instead of the cross polarization portion of the sequence. The data is acquired over the CPMG train and plotted along the x -axis as a function of time. A time of $0\ \mu\text{s}$ corresponds to the end of the 90° pulse or τ_{CP} period. The data in Figure 7.7(a.) and (b.) represent the echo train - gaps between the echoes are the locations of the CPMG pulses. The echo train therefore traces out the time-dependent S and S_0 curves, depending on if the 180° pulses are on the S -channel. In contrast to the typical 1-echo acquisition SEDOR sequence, much less time is required to acquire the full SEDOR dephasing curve since the echo time does not need to be incremented to obtain the S and S_0 curves. Here, we observe, in Figure 7.7(a.) and (b.), a typical CPMG signal for S_0 (black) and an oscillatory S curve (red). The oscillation occurs due to the total dephasing strength for the observed nuclei. In Figure 7.7(a.), all three peaks are being observed, leading to multiple dephasing strengths being observed (i.e., the “isolated” ^{113}Cd and paired ^{113}Cd will have different coupling strengths to the nearest ^{125}Te). In Figure 7.7(b.), we can overcome this issue by selectively exciting the paired ^{113}Cd by the use of CP. Of note, the signal intensity passes through zero and inverts in phase, as the nuclei precess about the dephasing nuclei.

The resulting SEDOR curves are plotted as $\Delta S/s_0$, which is the difference between the SEDOR experiments with and without the 180° pulses on the S -channel (ΔS), divided by the S_0

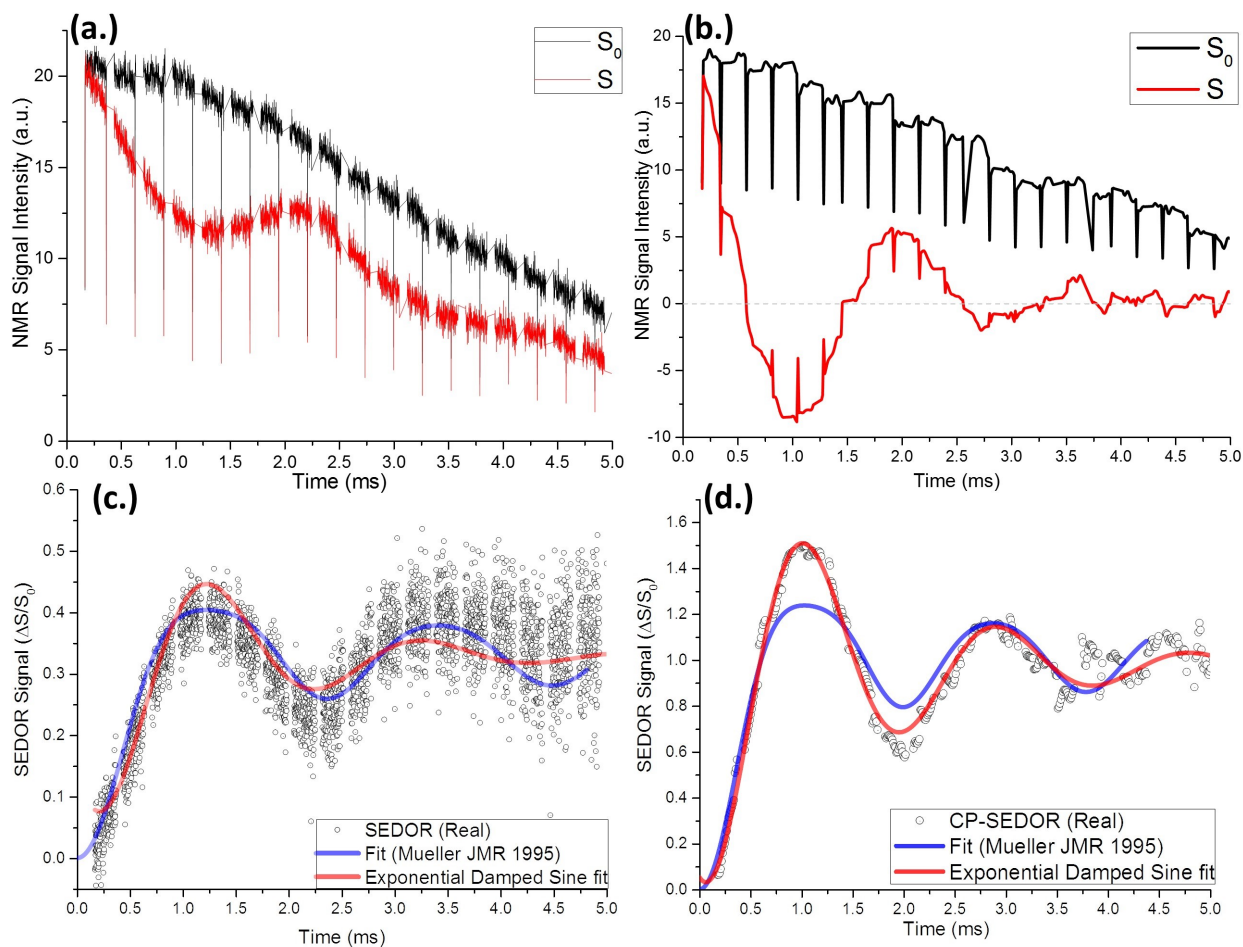


Figure 7.7: OP SEDOR data of ^{113}Cd - ^{125}Te spin pairs. (a.) OP SEDOR S (red) and S_0 (black) curves. (b.) OP-CP SEDOR S (red) and S_0 (black) curves. (c.) and (d.) are the resulting SEDOR curves, represented by black circles. The typical analytical SEDOR fit [23] for a powder/amorphous sample is shown in blue and an exponentially damped sine curve (red).

SEDOR experiment (without the S -channel 180° pulses). For the OP SEDOR sequence without CP, neither the typical analytical model or exponentially damped sine curves fit the data well, likely due to the multiple contributions to the dephasing. The resulting data for the CP-SEDOR was also fit by a damped sine curve (red line), as expected for nearly isolated pairs of ^{125}Te - ^{113}Cd nuclei, similar to that seen in other single crystals [83]. No clear signal originates from the 180° orientated Cd-Te bond with the weaker coupling, likely due

to the short (1 ms) contact time used for the CP portion of the experiment. The function here results in an amplitude of 1.01 ± 0.02 , a decay time constant of 1.63 ± 0.05 ms, and a coupling strength of 946 ± 5 Hz for the parameters of interest, which agree well with the satellite oscillations in Figure 7.5. Note the damped-sine curve fit is offset by a value of 1, indicating the dephasing in the S echo train occurs fully before the S_0 echo train, typical of SEDOR experiments [23].

Using the OP-CP SEDOR sequence, we measured the ^{113}Cd - ^{125}Te coupling strength with and without the laser irradiation left on during the pulses and acquisition with no discernible difference for CdTe (within 1 Hz of each other). Therefore, the effect observed by A. Goto, et al. [68] of incident photons at or near the band gap tuning nuclear-nuclear coupling (i.e. an electron density of states tunable nuclear coupling) is either unique to their sample or too weak in CdTe to be observed in the directly bonded spin pairs.

7.4 Conclusions

We have shown the ability to selectively excite ^{113}Cd - ^{125}Te spin pairs in CdTe. In addition, the coupling strength and dephasing time of the spin pairs was analyzed by CP build-up times and SEDOR methods. In future experiments, INEPT (insensitive nuclei enhanced by polarization transfer) can be used instead of CP in order to take advantage of the J -coupling for the polarization transfer, rather than the total coupling strength used in the CP experiments presented here. An alternative method of SEDOR was implemented for faster acquisition, making this the first time this experiment was proven to work experimentally. In addition, we were able to complete SEDOR from an optically initialized nuclear spin system for the first time. In contrast to previous results on GaAs [68], no observation of tunable

coupling strengths via optical irradiation was found in CdTe. This is the first experimental step towards using pseudo-isolated spins and spin pairs in CdTe with conventional NMR techniques and nuclear initialization with optical pumping in spintronic and quantum computing applications. Future experiments could investigate the placement of the dephasing pulses on the Te channel as well as rotation of the sample to accurately separate the isotropic and anisotropic coupling strengths. In addition, the use of continuous wave amplifiers would allow for measurement of the longer time dynamics present in the spin pairs. The use of other decoupling and refocusing sequences can also be tested to compare techniques.

Chapter 8

OPNMR Investigation of an Al₂O₃-GaAs Interface

Through a collaboration with groups from Oregon State University (Professor John Conley, atomic layer deposition) and Washington University in St. Louis (Professor Parag Banerjee, finite element method), the interface of a GaAs-Al₂O₃ sample was analyzed via OPNMR. The sample exhibits interface specific signals, only clearly observable only by OPNMR. In addition, the spectral features allowed for multiple ways to measure extremely high polarizations, yet to be seen in OPNMR experiments. Some of the results and discussions in this chapter has been published in Reference [84].

8.1 Introduction

Semiconductors are often layered in solid-state electronic devices using materials with dissimilar band gap energies [85]. To create higher performing electronic devices, a better understanding of the chemical structure/electronic property relationship of the interface is

necessary. The specific sample studied here ($\text{Al}_2\text{O}_3/\text{GaAs}$) has been proposed for many applications including MOSFETs [86, 87], MOS capacitors [87], and as a passivation layer for GaAs [86, 87, 88, 89]. By determining the interfacial structure, we may be able to manipulate growth and adjust synthetic procedures to change interface structure and reduce the number of defects that affect the electronic performance of devices.

Solid-state nuclear magnetic resonance (ssNMR) has been used to study inorganic semiconductors [90]; however, conventional NMR techniques are usually incapable of measuring spectra from interfaces due to the extremely small number of spins present and the large number of spins needed for NMR detection ($\approx 10^{16}$) [8, 91, 92]. Hyperpolarization allows a lower detection threshold for NMR spectroscopy of samples with rare nuclear spins, including surfaces, interfaces, and those with low isotopic abundance.

Optical pumping relies on the use of laser excitation to form unpaired polarized electron spins. Optical pumping creates non-equilibrium spin states by taking advantage of optical transitions and their respective relaxation rates to hyperpolarize the electrons, which, in turn, transfer polarization to the nuclear spins to which the electrons are coupled.

Optically-pumped NMR (OPNMR) [11, 12] is a technique which combines optical pumping of electrons in semiconductors and detection of the nuclear magnetization (i.e. nuclear spin state populations) with traditional radio-frequency NMR methods. The OPNMR signals are photon energy dependent, and vary as a function of the laser penetration depth since the laser-excited electrons are the origin of the hyperpolarization [51]. Thus, the laser intensity and spatial distribution throughout the sample, determines the portion of the sample being enhanced, and therefore the portion of the sample detected.

The nuclear isotope studied in this chapter is quadrupolar, ^{75}As (nuclear spin quantum number, $I = 3/2$), which means the nuclear spins also couple to any electric field gradient (EFG) present, resulting in a splitting of the NMR resonance [93, 94]. For nuclei in highly symmetric environments, the resulting quadrupolar splitting will be zero. However, since stress can perturb a structure away from perfect cubic symmetry through bond distortions, lattice strain can be detected from the amount a quadrupolar resonance is split [95, 96, 97]. Strain in GaAs has been studied previously by OPNMR (and ODNMR) methods to determine nuclear spin temperatures [35], bandstructure effects [17], spatial inhomogeneities of strain in a quantum well [97], and dominant polarization mechanisms in different spatial regions [15, 50, 52].

8.2 Experimental

8.2.1 Al_2O_3 -GaAs Interface Sample

A 400 μm bulk semi-insulating single crystal of GaAs (ITME, grown along [100], lot 2137, polished on one side) was used as a substrate. A thin film of amorphous alumina, hereafter denoted “ Al_2O_3 ”, was deposited using atomic layer deposition (ALD) on the polished side of the GaAs. The deposition temperature was 300 $^\circ\text{C}$. Four pulses of tri-methyl aluminum were used to remove the native oxides on the surface of the GaAs substrate [88, 89] prior to ALD growth. The final thickness of the Al_2O_3 film was 11.2 nm and is shown schematically in Figure 8.1.

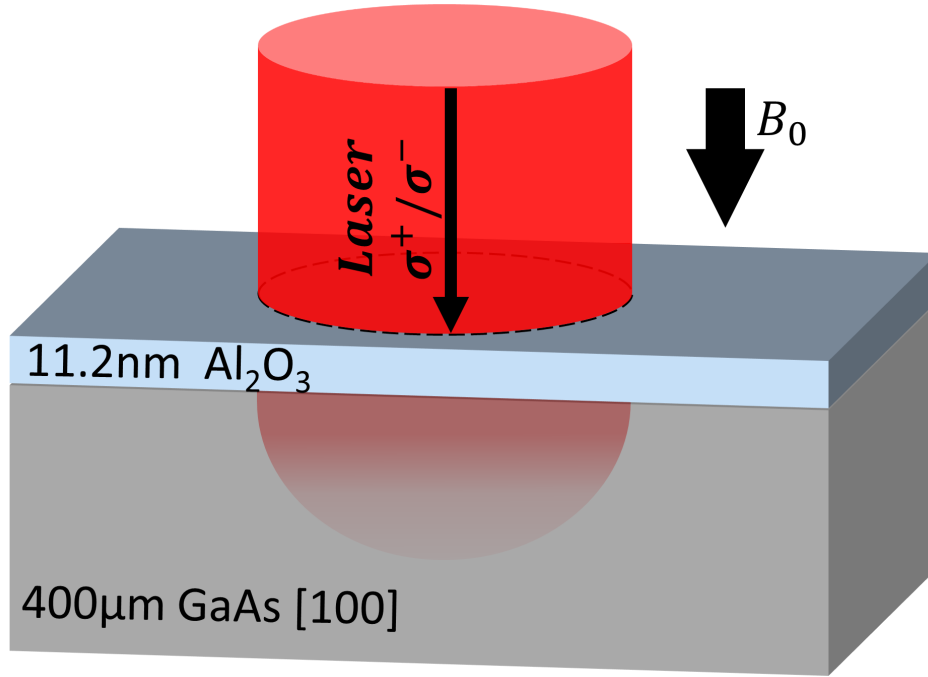


Figure 8.1: The sample configuration in the OPNMR experiment showing the orientation of the laser Poynting vector and the external magnetic field vector (B_0) with respect to the sample. The laser passes through the Al_2O_3 film and into the GaAs where it is absorbed.

8.2.2 OPNMR Methods and Sequences

The experimental procedures for OPNMR have been described previously, with critical parameters for the observation of the interface listed here: [12, 18] external magnetic field (B_0) of 4.7 T, B_1 excitation strengths were ≈ 20 kHz, circularly polarized light was used with the laser power (measured at the cryostat window) held constant at 100 mW, sample irradiated for a time period of τ_L (90 s) after the saturation sequence, a short period of time (τ_D) was inserted where the laser was shuttered (≈ 1 s), and the NMR spectra were then acquired by a quadrupolar echo [98] pulse sequence (using 55° pulses) while the laser was shuttered (Figure 8.2). For the observation of the interface signals, 55° tip angles were used in order to observe the asymmetry of the satellites and refocus the dipolar and quadrupolar

interactions [99, 100, 101]. The $90^\circ-\tau-64^\circ$ pulse sequence [99, 100] results in symmetric satellites, which does not properly depict the spin temperature. The $55^\circ-\tau-55^\circ$ sequence represents the best (approximate) tradeoff between optimal refocusing of the central transition and the satellites for a spin- $3/2$ nucleus [101]. The polarization measurement sequences instead implemented a single $<10^\circ$ pulse to accurately measure the polarization in 4.7 T and 3.0 T external fields.

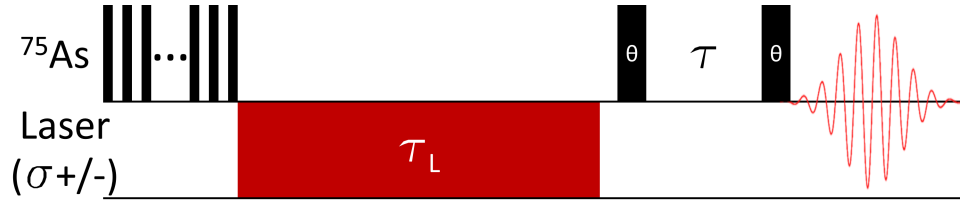


Figure 8.2: Optically-pumped quadrupolar echo pulse sequence used to acquire the interface spectra (not polarization measurements). ^{75}As polarization is first destroyed by a saturation train. The GaAs is then optically pumped with $\sigma+/-$ for a period of τ_L (1.5 min with $\sigma+$ polarized light used for interface spectra). The laser is then shuttered for 1 s before a quadrupolar echo sequence is used to observe the spins. θ is the radio-frequency flip angle, here 55° . (Not scaled proportionally with respect to time.)

Since polarization originates from the optically-excited conduction electrons [38], the spatial regions where the light is absorbed determine the portion of the sample that can be observed. The size of such regions is governed by the beam diameter, the position of the laser on the sample, and the penetration depth of the light. Absorption coefficients and the resulting penetration depth of the laser have been used to previously model the photon energy dependence of OPNMR spectra [51]. In this study, all photon energies used were much smaller than the band gap of the ALD-deposited Al_2O_3 (at $\approx 9\text{ eV}$ [102]), allowing the laser to pass through the ALD film to the GaAs substrate underneath. The laser intensity then decays exponentially with depth [12] into the GaAs. At high optical absorption values ($\alpha_{opt}(E)$), the laser excites conduction electrons in only the topmost GaAs layers located in the interfacial region, where strain induced by the Al_2O_3 layer is present as discussed below. The minimal

penetration depth of the laser (estimated as <275 nm [103]) in the OPNMR experiments relegates the observable signal to the top portions (interface region) of the GaAs. At lower photon energies, the laser will penetrate deeper into the sample, and thus observe a large fraction of the bulk (≈ 400 μm thick) GaAs crystal away from the interface.

8.2.3 Thermal Strain

Due to the ALD deposition parameters (i.e., temperature and surface pretreatment), the resulting Al_2O_3 film is amorphous, reducing most of the strain which would be due to the lattice mismatch of the two structures. (GaAs has a zincblende cubic unit cell with a lattice constant of 5.65 \AA , and Al_2O_3 a hexagonal unit cell with lattice constants $a = 4.79$ \AA and $c = 12.99$ \AA .) However, since the growth of the ALD film occurs at higher temperatures, thermal strain can develop when the sample cools, and the materials compress according to their thermal expansion coefficients. The thermal strain, ϵ , resulting from differing thermal coefficients of the film and substrate is expressed as [104]:

$$\epsilon = (\alpha_{film} - \alpha_{substrate}) \times (T_i - T_f) \quad (8.1)$$

where α is the thermal expansion coefficients, and T the temperatures of the growth ($T_i = 573$ K) and final temperature ($T_f = 6$ K). The difference in thermal expansion coefficients is $1.3 \times 10^{-6}/\text{K}$ [105]. The resulting thermal strain expected for our experiments is 7.37×10^{-4} (dimensionless units), leading to changes in the crystal structure dimensions which will be most intense at the interface, and dissipate linearly with distance from the interface [106].

8.2.4 Strain Induced Quadrupolar Splitting

The strain at 6 K will create an electric field gradient (EFG) and results in splitting into a quadrupolar lineshape. Since the ^{75}As electric quadrupole moment ($Q = 0.29 \times 10^{28} \text{ m}^2$) is comparatively large, small amounts of strain will result in splitting of the signal. Deeper into the GaAs bulk crystal, the strain diminishes until the nuclear spin environment is a single unsplit resonance owing to the cubic symmetry (zincblende crystal structure) of the lattice.

Through the continuing use of finite element methods, the dependence of the strain as a function of depth in the sample can be modeled [107, 108]. The results show a linear dependence with depth for reasonable optical penetration depths ($>5000 \text{ nm}$). If the strain has a linear dependence, without additional factors, this would indicate the satellites to be approximately flat rectangular peaks from the maximum strain (interface) to minimum strain values (bulk) present in the sample. However, additional factors, including laser intensity, must be included to the strain calculation to accurately model the expected lineshapes. Through a continued use of finite element methods, we hope to correlate the NMR signals to depths in the sample in order to help elucidate effects present at or near the interface.

8.3 Results and Discussion

8.3.1 OPNMR Signal From a Buried Interface

Interface signals are difficult to measure by NMR due to the large variety of bonding environments, defects, strain, and their non-crystallinity resulting in larger dispersion of observable frequencies. The atoms at the interface (i.e., bonded directly to Al_2O_3) are essentially a

monolayer and their NMR-active nuclear spins (^{75}As , ^{71}Ga , ^{69}Ga) would be shifted in frequency with respect to the bulk signal owing to the distinct chemical environment. As these are all quadrupolar spins (nuclear spin quantum number $I = \frac{3}{2}$ for all), both the chemical environment and strain would create a large electric field gradient (EFG), resulting in splitting from the quadrupolar interaction. The other nuclear spins in the interfacial region are nuclei which experience an effect from the interface without being directly bonded to the Al_2O_3 . These nuclei would remain unshifted in frequency (to first order) but the strain would still be present, creating an EFG around the nuclei and therefore a splitting. As depth into the sample increases, the strain diminishes until the nuclear spin environment is identical to the bulk GaAs sample with cubic symmetry. The nuclear spins at the interface and in the near-interface strained region have a very limited number of spins, and their signals would be hidden by the large bulk signal when detected conventionally. The use of optical pumping overcomes this issue by limiting signal to the penetration depth of the laser and by hyperpolarizing the nuclear spins present in the top layers of the GaAs, where the absorption occurs.

Coated and Uncoated Spectra Comparison

For standard NMR, what appears to be a single peak is observed as seen in Figure 8.3 (black dashed line). However, instead of the expected Gaussian peak for the static crystal, tails are present in the peak, resembling a Lorentzian shaped line. This is likely due to the strain present in the sample which results in multiple peaks from the nuclei with different quadrupolar splittings because they are experiencing different values of strain in the sample. As one can see, no clear information is obtainable due to the appearance of a single peak.

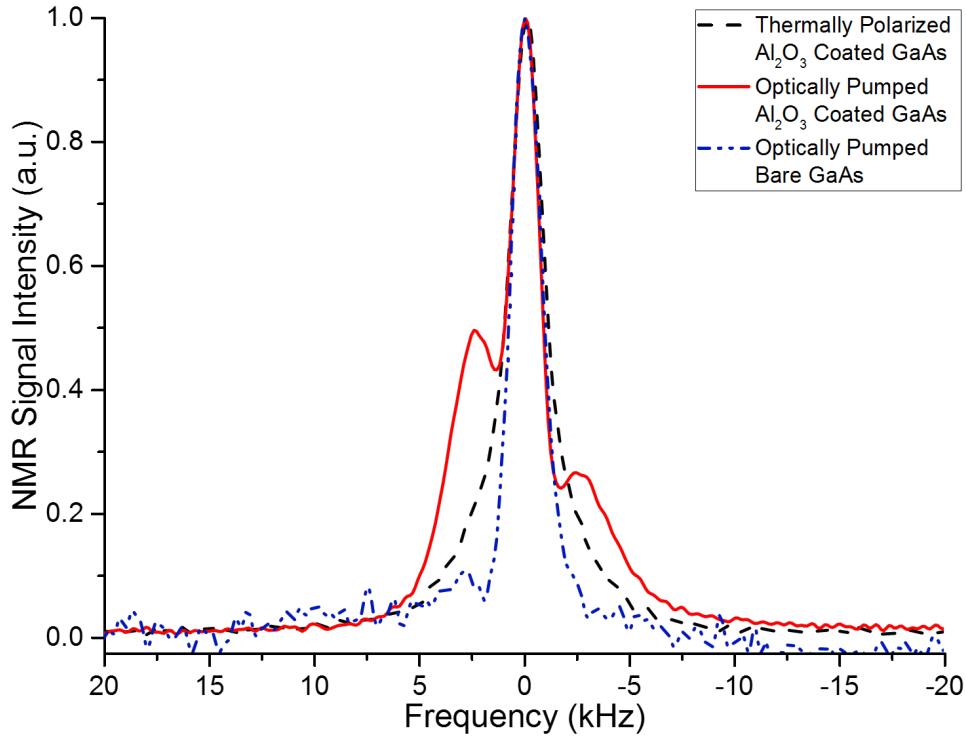


Figure 8.3: ^{75}As NMR (black dashed line) and OPNMR (blue dot-dash and red solid lines) of GaAs. Comparison of the conventional spectrum of the coated GaAs (black) to an optically pumped spectra of “bare” GaAs with its native oxide present (blue) and the OPNMR spectra of the Al_2O_3 -coated GaAs (red). The optically pumped NMR spectra were recorded at a wavelength of 819.3 nm. The spectra have been normalized.

Optically-pumped NMR of the Al_2O_3 -coated GaAs sample (shown in red, 8.3), using photon energies in excess of the excitonic absorption ($\approx 1.517\text{ eV}$), can then be compared to that of the “bare” GaAs. OPNMR of the Al_2O_3 -coated GaAs produces three peaks; the two outer peaks are the quadrupolar satellites, while the middle peak is predominantly² from the central transition. The satellite intensities are asymmetric, indicating high levels of nuclear polarization [35] – evidence of spin cooling below that of the “high temperature approximation” [34]. With the large polarization present, the populations are best represented by an exponential distribution (assuming a single spin temperature) which leads to

²The central peak would be the combination of the central transition of the quadrupolar split spectrum and signal from any unsplit bulk GaAs being polarized.

larger population differences, and thus larger transition intensities, for transitions at lower (for positive spin temperature) or higher (for negative spin temperature) frequencies. The clear resolution of the peaks between the satellites and central transition confirm that we are observing only nuclei with enough strain to distinguish their satellites from the central transition.

To prove the satellites and tails are due to strain, we can perform OPNMR on an identical GaAs wafer, which did not have the ALD film placed on top. The results can be seen in Figure 8.3 (blue, dashed-dot line), where the spectrum only contains one peak with a Gaussian shape.

Next, we would like to estimate the strength of the quadrupolar interactions (and thus strain) in our system. The first order quadrupolar splitting (for an $\eta_Q = 0$) [94], given by:

$$\nu_Q = \frac{3eQV_{zz}}{8I(2I-1)\hbar}(3\cos^2\theta - 1) \quad (8.2)$$

relates the magnitude of the EFG and the orientation of the EFG tensor with respect to the magnetic field. In the equation, eQ is nuclear electric quadrupole moment, V_{zz} is the largest component of the EFG tensor, and θ is the angle between the V_{zz} component of the EFG and the external magnetic field. For a single quadrupolar interaction, we would expect the satellite peaks to have Gaussian lineshapes. The satellite peaks do not fit to perfect Gaussian lineshapes as they have asymmetric “tails” distributed away from the central transition (Figure 8.4); this spectral feature is attributable to a distribution of EFG’s (and therefore ν_Q ’s) arising from the perturbative effects of the interface, detecting different amounts of strain, likely as a function of distance from the top of the sample. Modeling this type of continuum of interaction strengths has not been done before, and is not trivial.

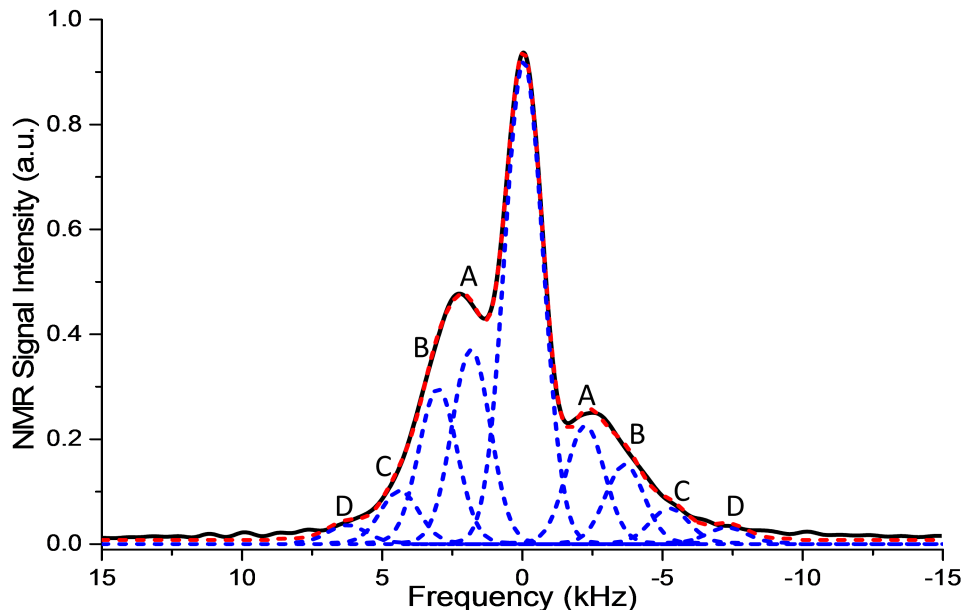


Figure 8.4: ^{75}As OPNMR of the alumina-coated GaAs showing the deconvolution of spectrum using Gaussian peaks with a linewidth fixed to that of the “bare” ^{75}As OPNMR. The blue dashed lines are the individual Gaussian peaks which comprise the red fit. The spectrum was recorded using 819.3 nm light.

In order to estimate the quadrupolar interaction strengths in the sample, the two asymmetrically-shaped quadrupolar lineshapes, have been deconvoluted into a series of quadrupolar satellites, whose width is constrained to that of the single-crystal resonance in the “bare” GaAs spectrum ($\text{FWHM} \approx 1.5 \text{ kHz}$). Four such peaks effectively fit each quadrupolar lineshape, each split symmetrically about the central transition (with a linear offset, the cause of which is unknown). Table 8.1 lists the relative intensities and splittings of the satellites. While a sum of many Gaussians (representing a continuum) could effectively fit the data, here we have selected the minimum number to provide a straightforward picture of the degree of splitting and the different fractions of the sample with similar strain.

Since the theoretical peak intensities in a quadrupolar, $I = \frac{3}{2}$, spectrum is 3:4:3 using small tip angles [109], the percent of signal due to the strained nuclei can be calculated. Thus,

Table 8.1: Satellite peak parameters acquired by deconvolution of Figure 8.4. The intensities are relative to that of the central peak intensity, set to a value of 10.0.

Satellite Pairs	$4\nu_Q$ (kHz)	Relative Intensity	Contribution to Central Transition
A	4.08	6.44	$\frac{4}{6}6.44 = 4.30$
B	6.68	4.83	$\frac{4}{6}4.83 = 3.22$
C	9.65	1.80	$\frac{4}{6}1.8 = 1.20$
D	13.55	0.69	$\frac{4}{6}0.69 = 0.46$
			$\Sigma=9.18\pm0.51$

the ratio of central to satellite intensity should be 4:6. However, assumptions must be made for the intensity of the strained central transition using Figure 8.4. Conservatively, if an estimate is made from the average of the two satellites' integrated areas [110] and using the 4:6 ratio, $91.8 \pm 5.1\%$ (area = 9.18) of the observed nuclei are strained as seen in Table 8.1. We ascribe this extra 8.2% intensity in the central transition from unstrained ^{75}As atoms being optically pumped. In addition, the quadrupolar splitting of even the outermost Gaussian peak corresponds to a strain of 3.4×10^{-5} [17], which is less than the expected strain (7.37×10^{-4} , see Equation 8.1), indicating the observed satellite peaks correspond to areas deeper in the sample where strain has been partially relaxed. The observed NMR signal decays to the baseline at $\approx \pm 15$ kHz, corresponding to a maximum observed strain of 7.53×10^{-5} , also much smaller than expected. This is suggestive of the inability to detect the nuclei with larger strain. Potentially, the absence of larger strain could be indicative of either a depletion zone[52] or other interactions which reduce the electron and nuclear polarization at the interface.

Optical Excitation Wavelength Dependence on Interface Signal

The effect of laser penetration depth, governed by the optical absorption coefficient, can be seen from the OPNMR spectra recorded as a function of photon energy, and the resulting ^{75}As lineshapes are plotted in Figure 8.5. The vertical lines in the figure correspond to the (theoretical) wavelengths for the excitonic and band gap transition energies at 0 K [111], for reference. Since our experiments were performed at a temperature of 6 K, the precise photon energies for the transitions should be shifted slightly left to a higher wavelength (lower energy). The spectrum at 821.3 nm (below E_g , the band gap energy) shows a lineshape dominated by the central peak which masks the satellite peaks due to the deeper penetration of the laser (to tens or hundreds of μm). We do observe broadening at the base similar to that seen by conventional NMR (though with slightly asymmetric phasing)³. The spectrum pumped at 818.3 nm, is polarized by laser excitation of a bound exciton [28], which results in a very shallow penetration depth because of the intense absorption at this wavelength [51]. Notably, it is at this photon energy (wavelength) where the quadrupolar satellites are first clearly resolved. For the spectrum with an optical pumping wavelength of 815.3 nm (also above E_g), the polarization remains relatively the same. Due to the large increase in the absorption coefficient at and above the band-gap energy, all the spectra above the band gap originate from areas of strain while the spectra below the band gap cannot be deconvoluted due to the large contribution of the unstrained GaAs.

Other recent studies in OPNMR of strained GaAs have shown evidence of quadrupolar splitting, reporting on a significant dependence with laser power [15, 50, 52]. Sub-bandgap irradiation was used in their experiments [15, 50, 52], revealing both a positive spin temperature at low laser power (ascribed to quadrupolar relaxation close to defect sites) and

³As documented previously [38], we use the “system phase” for all experiments.

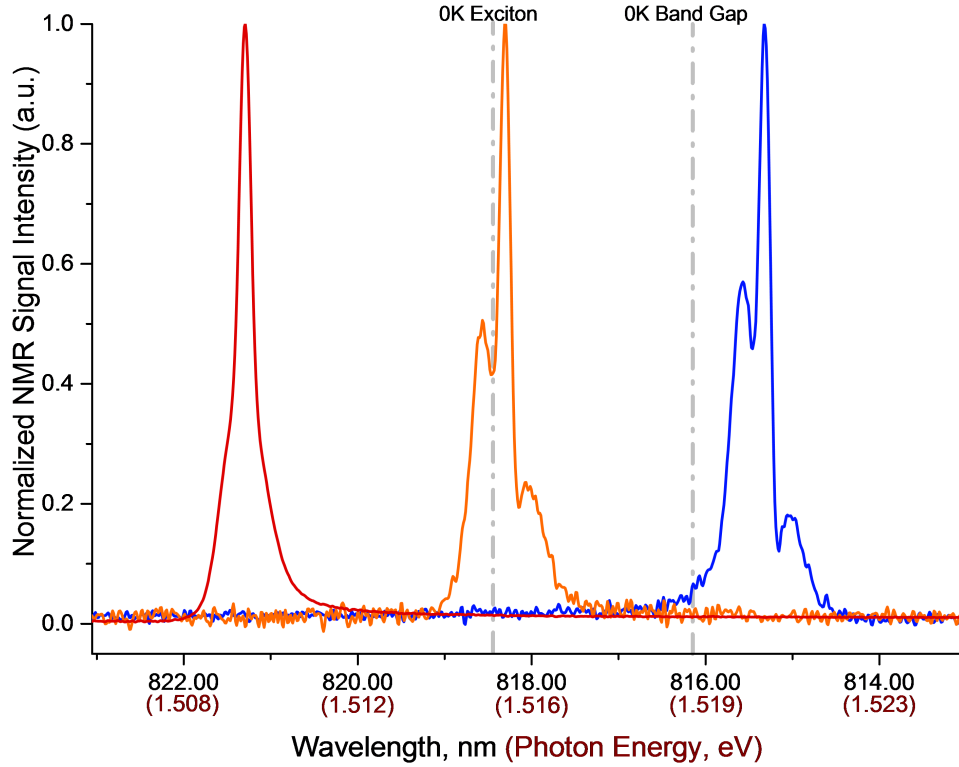


Figure 8.5: Intensity normalized ^{75}As OPNMR spectra at various photon energies/wavelengths. The spectra (from left to right) are in order of decreasing wavelength (increasing photon energy) with the central transition positioned over the corresponding optical excitation wavelength. Theoretical positions of the band gap and exciton absorption energies are shown as dashed lines.

a resolved quadrupolar splitting attributed to strain *throughout* the sample, exhibited only with high laser power arising from hyperfine relaxation (and negative spin temperature) for σ^+ light. With similar conditions (high laser power and sub-bandgap irradiation), we only observe indistinct quadrupolar splitting with a lineshape dominated by the central transition. These results illustrate different strain environments. The experiments in this chapter only have strain concentrated at the near surface accessed by high photon energy, while other studies [50] have strain throughout accessed by low photon energy.

Laser Helicity Dependence

$\sigma+$ light carries + 1 unit of angular momentum and thus creates conduction electrons primarily in the $m_s = -\frac{1}{2}$ state, opposite in sign to that of thermal equilibrium. As the hyperfine interaction allows the total conduction electron energy to equilibrate with the total nuclear spin energy, the nuclear spins also become polarized (populated) toward non-equilibrium m_I spin states. If the polarization is high enough, the initial population would be primarily in the $m_I = -\frac{3}{2}$ state. Since the helicity of light determines the direction the nuclear spins are optically pumped, using $\sigma-$ light should initialize the nuclear spins in the $m_I = +\frac{3}{2}$ state. The population transfer due to a B_1 pulse would then start from that initial state, and follow the expected transition of $\Delta m = -1$. An example spectra for both helicities of light can be seen in Figure 8.6. Since the flip angle is less than a 90° pulse, we will primarily observe the transitions from the initial spin state and the central transition.

8.3.2 OPNMR Hyperpolarization at an Interface

Satellite intensities have been used previously to calculate the polarization of the observed nuclei [35, 112]. Because quadrupolar splitting creates transitions at three different frequencies and the phase correlates to the sign of Δm , the peak intensities can be used to describe the population differences between the states. However, the central peak may be convoluted by unstrained signal, therefore it will not be used in the calculation for the spin state populations. If we were to assume an exponential population toward the $\pm\frac{3}{2}$ spin states (depending on the helicity of light), the ratio of the two satellite intensities would be:

$$\frac{I_{-1/2 \rightarrow -3/2}}{I_{3/2 \rightarrow 1/2}} = \exp\left(\frac{-2\hbar\gamma_I B_0}{kT_n}\right) \quad (8.3)$$

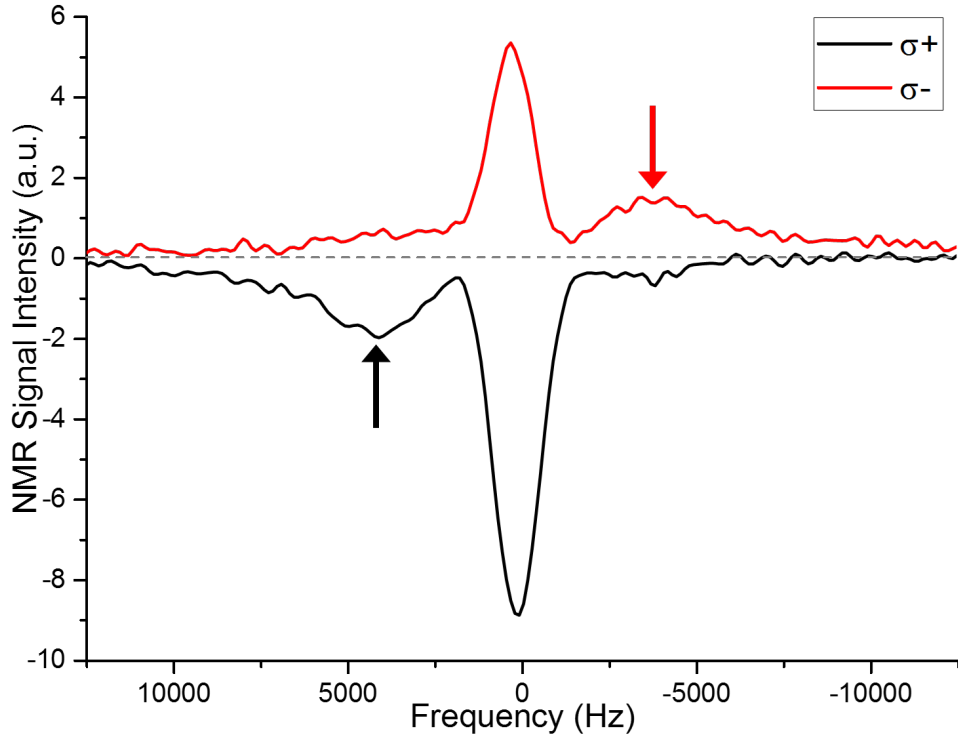


Figure 8.6: ^{75}As OPNMR spectra for $\sigma+$ (black, bottom) and $\sigma-$ (red, top) laser at 817.3 nm (100 mW). The spectra were recorded at 4.7 T for an optical pumping time of 1.5 minutes. The spectra are phased with respect to a conventional thermally polarized spectrum (positively phased). The pulse is roughly a 55° pulse in order to obtain more signal while still having an idea of the polarization (before the satellite begins to nutate).

where γ_I is the gyromagnetic ratio of the observed nuclei, B_0 is the external magnetic field, and T_n is the local average nuclear spin temperature. It is important to note, a single spin temperature is unlikely to represent all of the nuclei due to the laser irradiation volume not incorporating the entire sample and the equilibration of the nuclei only occurring at longer times. The local average nuclear spin temperature can then be solved for by rearranging Equation 8.3:

$$T_n = \frac{-2\hbar\gamma_I B_0}{k \ln \left(\frac{I_{-1/2 \rightarrow -3/2}}{I_{3/2 \rightarrow 1/2}} \right)} \quad (8.4)$$

The local average nuclear spin temperature can then provide insight into the polarization of the observed quadrupolar split nuclear spins, assuming an exponential population distribution.

To calculate polarization, the expectation value for the nuclear spin projection on the z -axis, $\langle I_z \rangle$, is needed. $\langle I_z \rangle$ can be calculated from the spin temperature for a spin- $3/2$ nucleus by [35]:

$$\langle I_z \rangle = \frac{1}{2} \tanh\left(\frac{\hbar\gamma_I B_0}{2kT_n}\right) + \tanh\left(\frac{\hbar\gamma_I B_0}{kT_n}\right) \quad (8.5)$$

For ^{75}As , where $I = \frac{3}{2}$, the maximum expectation value for $\langle I_z \rangle$ is $\pm\frac{3}{2}$ and would correspond to all observed nuclear spin states in one of the $m_I = \pm\frac{3}{2}$ states. This would equate to 100% polarization according to:

$$\text{Polarization}(\%) = \frac{\langle I_z \rangle}{I_z} \times 100 \quad (8.6)$$

Using Equations 8.4-8.6, we can now use the satellite intensities to calculate the nuclear spin polarization near the interface.

However, we would like to note that most of these measurements will be before an equilibrium spin temperature is reached. There is likely to be areas of higher and lower polarization in the sample due to the polarization transfer from the conduction electrons. If that is the case, what we are measuring is a distribution of spin temperatures and modeling their sum as a single average local spin temperature. It is important to realize this, as the populations are unlikely to be perfectly exponentially distributed between the spin states, especially at short times. The inability to use the central transition population difference as mentioned above prevents the use of three points to describe the exponential distribution and thus we are unable to provide insight into the validity of the exponential assumption, until a complete model is formed.

To study the polarization as a function of various parameters, small tip angle ($\approx 8^\circ$) pulses were used in order to not greatly perturb the system from the initial polarization after optical pumping. This is critical as seen in the nutation (Figure 8.7) where during the length of the NMR pulse, population is constantly changing which would lead to different measured polarizations.

OPNMR Nutation Dependence

Nutation with optical pumping changes the initial population distribution of the nuclear spin states. A horizontal slice from the $\sigma-$ nutation is compared to the same pulse width from the $\sigma+$ nutation in Figure 8.6 to show the initial population distribution. Therefore, we observe a negatively phased $\omega_0 + 2\omega_Q$ resonance for $\sigma+$ irradiation while a positively phased $\omega_0 - 2\omega_Q$ is observed for $\sigma-$ irradiation based on the energy level diagram in Figure 8.7(a.). The optically pumping behavior is further proof the observed splitting is due to straining the quadrupolar nuclei near the interface.

As mentioned earlier, nutation experiments study the population transfer between spins states as a function of irradiation length (B_1 pulse width). Thermally relaxed spins will possess a Boltzmann distribution of populations among the $I = 3/2$ energy levels ($3/2, 1/2, -1/2, -3/2$), with spin states lower in energy having more spins. When the B_1 pulse starts, spin population transfer can occur for all $\Delta m = \pm 1$ transitions. For the thermally polarized case, the spins would all follow the $\Delta m = -1$ transition due the lower states having more population. In the strained portions of the thermally polarized sample, all three transitions would be observable at all times during the pulse since the lower energy spins states have more population than the spins state higher in energy. The peaks will also be approximately

the same in intensity since the signal is proportional to the population difference between the spin states and $\omega_0 \gg \omega_Q$.

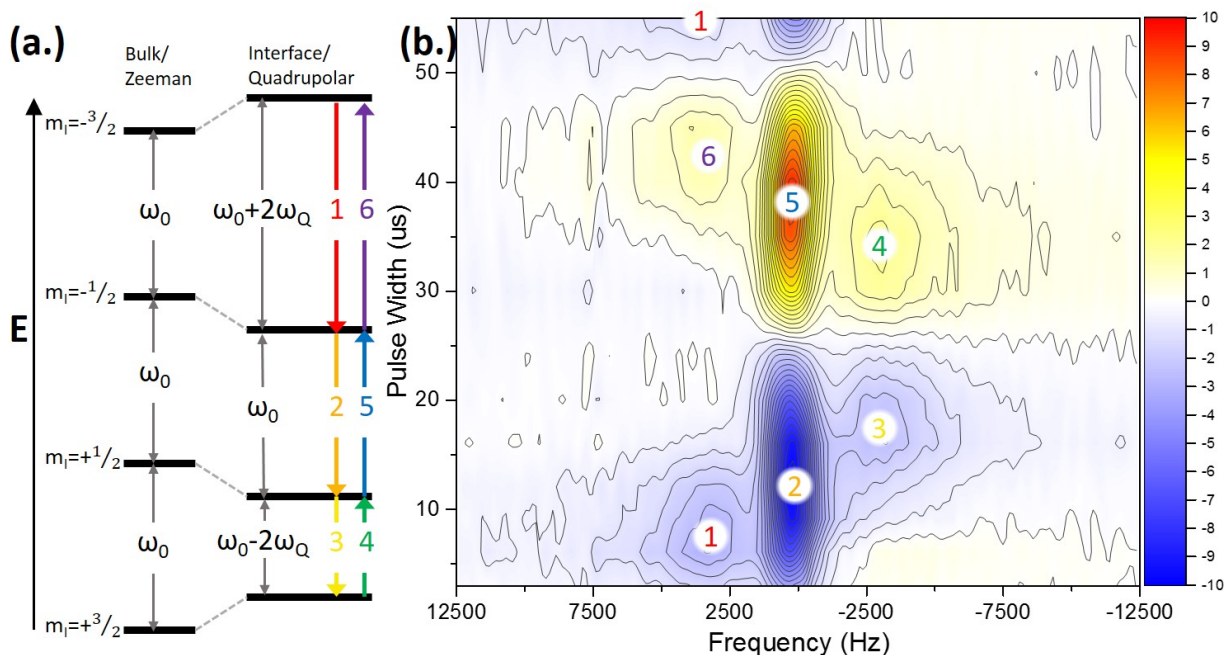


Figure 8.7: (a.) ^{75}As energy level diagram, and (b.) quadrupolar nutation under OPNMR at 4.7 T for 1.5 minutes of $\sigma+$ light (100 mW, 817.3 nm). (a.) Energy diagram of the nuclear spin states for the ^{75}As without (cubic) and with quadrupolar splitting. The gray arrows represent the transition frequencies of the allowed NMR transitions. Colored arrows denote the 6 possible transitions referred to in the text. (b.) Contour nutation plot of the ^{75}As OPNMR spectra using the Bloch decay sequence as a function of the pulse width. Horizontal slices are typical 1-dimensional OPNMR spectra. The numbered white circles correspond to the colored arrow transitions in part (a.).

In order to follow the nutation in the interface region, we need enhancement from the OPNMR, meaning we do not start with a thermal distribution of populations. We can then follow an initial $\sigma+$ polarized population ($m_I = -\frac{3}{2}$) as it nutates through the quadrupolar split energy levels as seen in Figure 8.7 (b.). Starting primarily in the $m_I = -\frac{3}{2}$ state, the only allowed transition with a population difference is the transition to the $m_I = -\frac{1}{2}$ state at a frequency of $\omega_0 + 2\omega_Q$, represented by transition “1” (red) in Figure 8.7. The signal

phase is negative since the sign of Δm (positive) is opposite of the thermal distribution Δm (negative). The population continues to move with $\Delta m = +1$ as it moves to the $m_I = +\frac{1}{2}$ (transition “2”, orange) and $m_I = +\frac{3}{2}$ (transition “3”, yellow) states at a frequency of ω_0 and $\omega_0 - 2\omega_Q$, respectively. Here, transition “2” (orange) is convoluted with the ω_0 transitions of the unstrained bulk signal. Once the spins are in the $m_I = +\frac{3}{2}$ state, the spins are fully inverted with respect to the magnetic field and the observable transitions are $\Delta m = -1$, in phase with thermal equilibrium. The population will then move back towards the $m_I = -\frac{3}{2}$ state going through transitions “4”, “5”, and “6” which are all positively phased. This cycle would then repeat again as seen in the top of Figure 8.7 (b.) where transition “1” is starting to appear again. This was able to be modeled in Mathematica using the density matrix formalism as shown in Figure 8.8 using only the RF Hamiltonian.

Through modeling, we can confirm the observed nutation behavior is due to the very high polarizations present from the optical pumping of the nuclear spin states. The acquired nutation aligns very well to a -2 mK spin temperature, or a -58% polarization, without fully optimizing all available parameters (again, under the assumption of an exponential population distribution described by a single temperature). In order to determine the maximum polarization able to be achieved with our experimental setup, additional parameters including wavelength, magnetic field, helicity of light, and optical pumping time will need to be varied.

Polarization Dependence on Multiple Parameters

The ^{75}As NMR satellite intensities and line-shapes were studied as a function of photon energy as seen in Figure 8.9. Photon energy affects which transitions are excited and the penetration depth of the laser into the GaAs. Exciting different transitions will result in

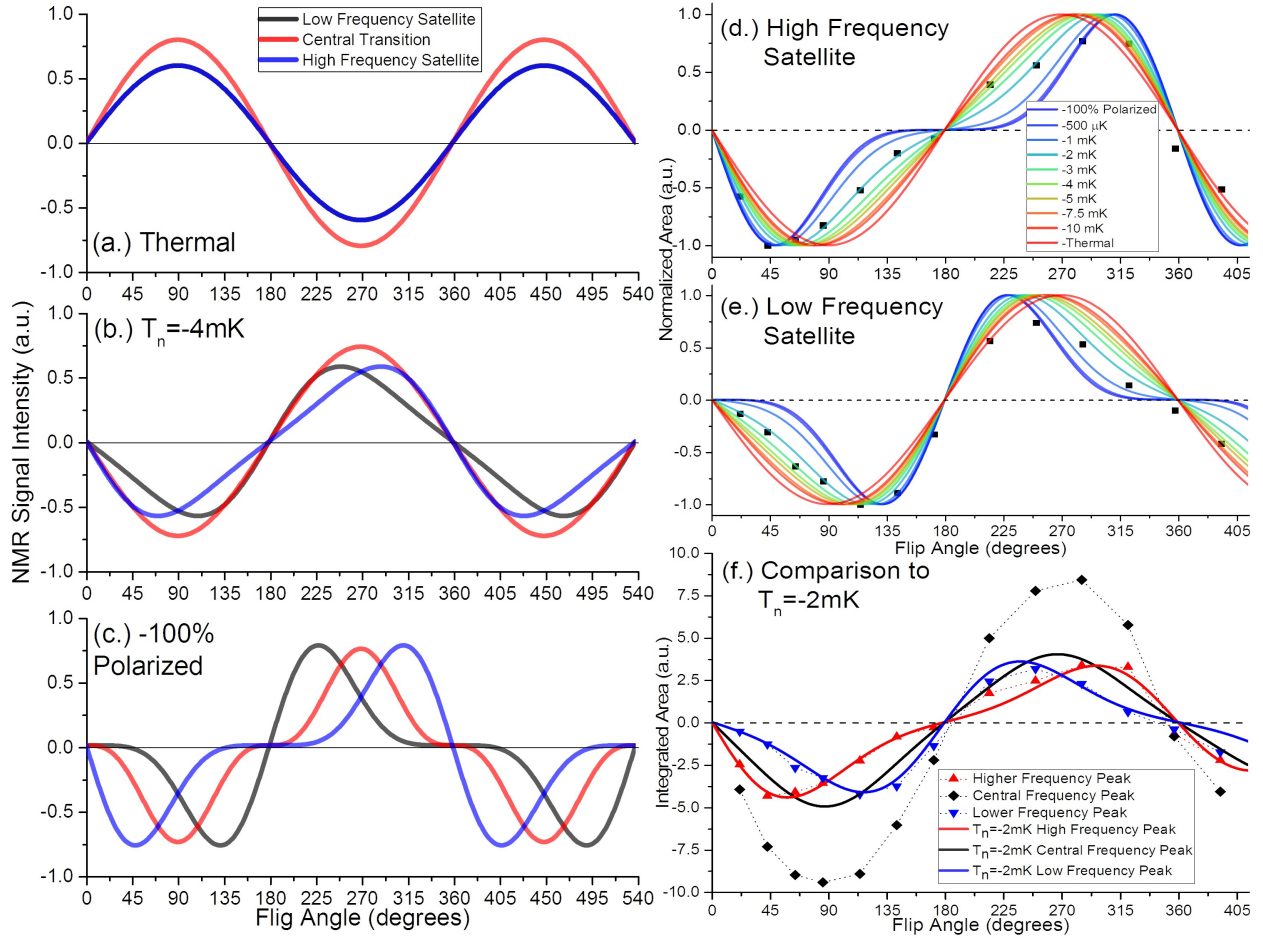


Figure 8.8: Model for nutation of a hyperpolarized weakly-quadrupolar-split interface signal. (a.) Expected nutation for the three satellites in a system where $\omega_{RF} \gg \omega_Q$. The satellite intensities are degenerate for the entire nutation. (b.) and (c.) are models for a -4mK spin temperature and -100% polarized nutation, respectively. (d.) and (e.) compare the amplitude of the satellite peaks to various spin temperatures for the high and low frequency satellites, respectively. (f.) Comparison to the best match spin temperature for the satellite nutation.

different electron polarizations due to differing amounts of light hole and heavy hole character in the valence bands [17, 37]. Since the absorption coefficient, which is a function of photon energy, changes the penetration depth of the laser, the number of nuclear spins being optically pumped will change as a function of wavelength as well. We can then infer three different regions for the wavelengths we measured based on the spectra which are marked by the

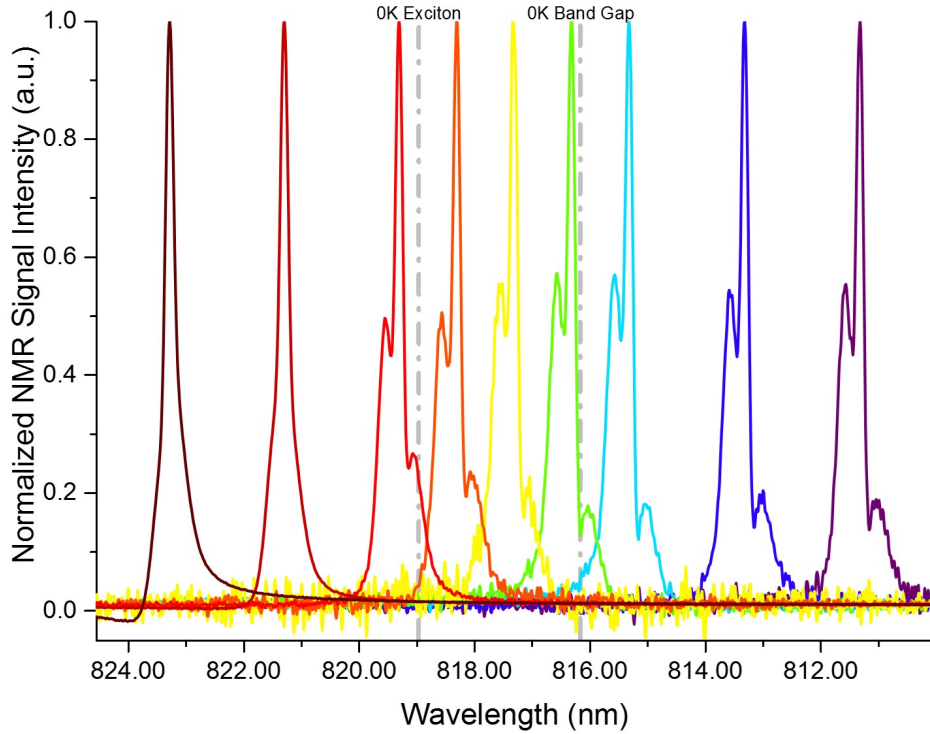


Figure 8.9: Normalized ^{75}As OPNMR spectra for 100 mW $\sigma+$ laser at various photon energies/wavelengths. The spectra were taken at 3.0 T for a optical pumping time of 1.5 minutes. The spectra are phased 180° out of phase with respect to a positive thermally polarized spectrum in order to have them positively phased and easier to compare by eye. The pulse is roughly a 55° pulse in order to obtain more signal while still having an idea of the polarization. The spectra (from left to right) are in order of decreasing wavelength and increasing energy with the central transition positioned over the corresponding excitation energy.

vertical dashed lines in Figure 8.9. Similar to the other plot (Figure 8.6), the lines correspond to the 0 K wavelengths for the excitonic and band gap transition energies and since our experiments were performed at a temperature of 6 K, the lines should be shifted slightly left (to a higher wavelength and lower energy). The two spectra at wavelengths greater than 820 nm show a line-shape dominated by the central peak which swamps the satellite peaks. We do observe some broadening of the base similar to that seen in the thermally polarized spectra. We would also like to note the slight phase twist in these two spectra, when phased with respect to thermal, for which the cause is currently unknown. The next

set of spectra, 820 nm to 817 nm, is polarized by laser excitation to a bound exciton and the quadrupolar satellites become observable. This is due to the much larger absorption coefficient for the material at this energy and thus less unstrained bulk signal being optically pumped. Polarization then increases as energy increases until the polarization reaches a maximum around the band gap energy. For spectra with optical pumping wavelengths less than 817 nm, the polarization and penetration depth remains relatively the same for the wavelengths we studied. From this data, we can confirm laser excitation, with an energy near the band gap, achieves the largest polarizations for this sample.

Next, several parameters (helicity of light, optical pumping time, and magnetic field) were varied in order to determine how they affect the polarization. We begin with the base set of experimental parameters used $\sigma+$ light for 10 minutes in a 3.0 T magnetic field (one of the data points in Figure 8.10). These parameters result in a relatively large negative polarization. By switching the helicity of light to $\sigma-$, the polarization becomes positive and roughly half of the $\sigma+$ data. The polarization is now positive since the nuclear spins are pumped the same direction as thermal equilibrium. The polarization being half as large, corresponds well to the asymmetry observed in the intensity of the OPNMR signals previously reported [12], lending to the asymmetry being due to different polarizations of the nuclear spins. If we increase the magnetic field to 4.7 T (while going back to $\sigma+$ light), our polarization is negative as we would assume for $\sigma+$ light but the polarization decreases to approximately 75% of the 3.0 T data. The decrease in polarization could be due to the magnetic field dependence of the optical pumping phenomena [6, 53] or the increased mixing of the states at higher fields [17, 37]. The last parameter to be studied was the length of the optical pumping time and the results can be seen in Figure 8.10. The time dependent polarization data was obtained by only varying the pumping time of the base set of parameters.

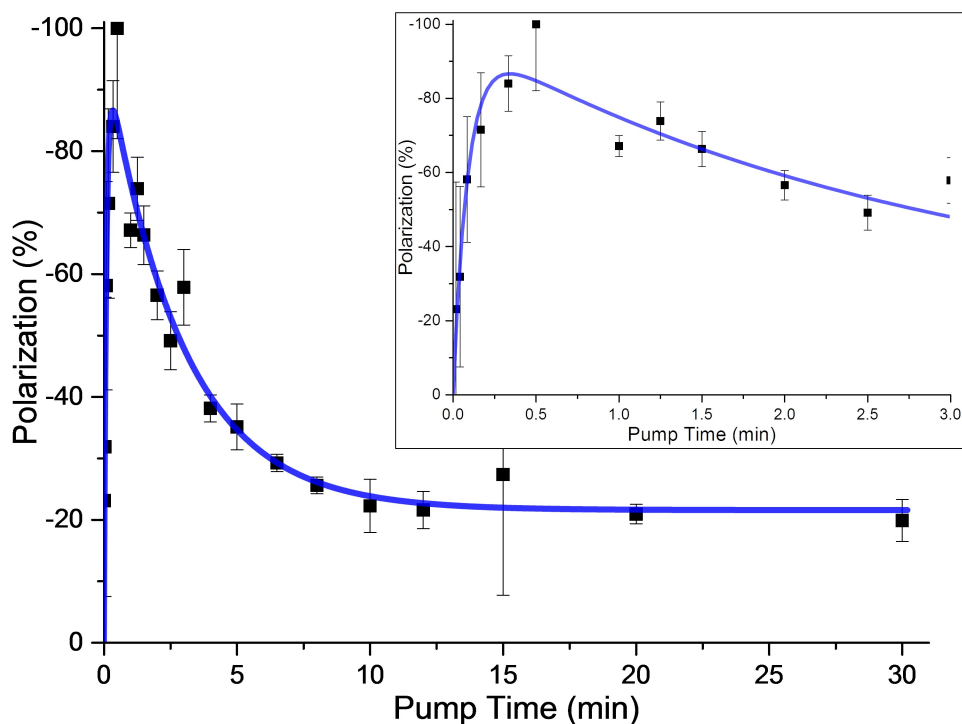


Figure 8.10: Local polarization of ^{75}As nuclei near the interface for 100 mW 817.9 nm $\sigma+$ laser at various optical pumping times. The spectra were taken at 3.0 T. The pulse is roughly a 8° pulse in order to not perturb the population/polarization of the observed quadrupolar split nuclei. The blue line is a fit to the data but plotted as guides to the eye. The inset shows the growth and fit to the shorter time points.

The time dependence of the optical pumping time showed a maximum polarization of $\approx 85\%$ at ≈ 0.5 minute. The polarization then decayed to an equilibrium of approximately 25% for the near interface ^{75}As nuclei. This behavior can be well represented by a competing fast exponential growth and slow exponential decay, similar to a cross polarization buildup curve, as seen by the blue line fit in Figure 8.10, meant as a guide to the eye. The only other similar results, achieved a polarization of $\approx 30\%$ [35], have shown the inability for traditional spin diffusion equations to quantitatively model the time dependence in this curves. Thus, quantitative modeling of the polarization dependence remains to be understood. However,

this result is very promising due to the large maximum polarization observed, indicating the potential use for further analyzing interfaces.

Many OPNMR studies have used a simplified theory [12, 19] for electronic polarization which leads to a maximum polarization of 50% due to the inter-band optical transition probabilities as described in Chapter 3 [31]. The theory though relies on the light-hole and heavy-hole bands being degenerate and only optically exciting at the band gap. This is inaccurate for OPNMR studies since the bands are perturbed by the magnetic field [14, 17], are optically pumped at multiple wavelengths, and, in this case, perturbed by strain effects [17]. Instead, the individual transitions and resulting $\langle S_z \rangle$ will need to be calculated for the perturbed bands [37, 113]. Thus, if a narrow laser is used, we can selectively excite transitions dominated by the heavy-hole or light-hole to obtain polarizations of 100%, if spin relaxation is neglected.

8.4 Conclusions

We were able to obtain NMR spectra of near interface ^{75}As nuclei in a Al_2O_3 -GaAs sample which exhibited signs of strain induced quadrupolar splitting at cryogenic temperatures. The strain is due to the lattice mismatch between GaAs and Al_2O_3 . The use of optically pumping was required in order to observe this smaller number of spins by NMR. Polarization was measured for various conditions in order to determine the best parameters to achieve the highest polarization. With the use of optical pumping, nuclear polarization of the near interface atoms was measured at values $>90\%$. The realization of highly polarized nuclei near the surface of a semiconductor via OPNMR lends to possible transfer of this polarization to materials on the surface.

Chapter 9

CASTEP Calculations of NMR

Parameters in Amorphous Alumina

As a side project and through a collaboration with Dr. Murat Aykol and Dr. Kristin Persson (Lawrence Berkely National Laboratory, molecular dynamics simulations), an attempt to model amorphous alumina was made. Many NMR studies have looked at spectra of precursors, their change as a function of annealing through amorphous phases, and the resulting crystalline alumina phases. The results have provided some information about the amorphous coordination and the observed trends with respect to annealing temperature; however, no atomic structural information has been derived. The combination of molecular dynamics, CASTEP calculations, and NMR spectra modeling have been combined and compared to experimental data to achieve an average structure representative of bulk amorphous alumina at different temperatures.

9.1 Introduction

Aluminum oxide is a model, complex polymorphic system with a wide range of stable and metastable crystalline phases such as α , γ , κ , η , β , θ and χ -alumina, and a competing amorphous phase [114]. The interest in amorphous Al_2O_3 beyond being a precursor for crystalline phases was in fact sparked by the discovery of spontaneous formation of such disordered films on aluminum metal at low temperatures, which gives it a natural corrosion protection [115, 116, 117]. Technological applications of amorphous alumina, *am*- Al_2O_3 , range from electronics [118] to protective coatings [119], where the properties are controlled by the local atomic structure.

Atomic structure of *am*- Al_2O_3 has been studied extensively with diffraction, microscopy, nuclear magnetic resonance (NMR) experiments [120, 121, 122, 123, 124, 125, 126] and with molecular simulations [127, 128, 129, 130, 131]. The chemical environment in this material is known to consist of a mixture of $n = 3, 4, 5$ and 6-fold coordinated Al-centered AlO_n polyhedra, but there are significant discrepancies in different reports of the relative amounts of such AlO_n units [130]. Using reverse Monte Carlo Simulation (RMC) of X-ray and neutron diffraction spectra, Lamparter and Kniep [120] reported 20 %, 56 % and 22 % for 3, 4 and 5-fold coordinated Al, which was later contradicted by many experimental and computational studies. Using magic-angle spinning (MAS) ^{27}Al NMR spectroscopy, Dupree et al. [125] showed that more than 30 % 5-fold coordination may exist in the amorphous films, depending on the sample preparation route, but they were not able to distinguish that possibility from an equal split to 4- and 6-fold coordination with much less 5-fold coordination. Using the same technique, Kunath-Fandrei et al. [124] suggested the fraction of AlO_5 is as small as 7%. More recent NMR experiments by Lee et al. [121, 122] on deposited Al_2O_3 films showed AlO_5 fractions around 40 %, with the rest being mostly 4-fold Al-O coordinations.

Using classical interatomic potentials in molecular dynamics (MD) simulations, Gutierrez and Johansson [132] reported a mostly 4-fold dominated structure with $\approx 20\%$ 5-fold coordination, whereas Jahn and Madden [133], and Hoang [129] reported approximately 5:4 ratio for of 4- and 5-fold polyhedra dominating the structure. Based on structures derived from ab-initio MD (AIMD), Davis and Gutierrez [134] also reported similar ratios; approximately 50%, 40% and 10% for 4, 5 and 6 fold Al-O polyhedra, respectively. Calculating X-ray photoemission (XPS) spectra and NMR shifts using first-principles, Lizarraga et al. [130] showed the amount of AlO_5 increases as density increases (within the range of $\approx 40\text{--}60\%$), along with AlO_6 , in expense of AlO_4 . Overall, there exists a strong dependence of local coordination environment in *am*- Al_2O_3 on the synthesis route and characterization technique in experiments, and on the description of interatomic forces (e.g. classical potential vs. first-principles) and structure generation pathways in computational studies.

NMR studies [135, 136] are very sensitive to local environments and have been completed on Al_2O_3 crystalline phases and precursors, as well as the spectral dependence on annealing temperature before reaching the stable phases. However, for the amorphous annealing temperature regions, few have attempted to understand the changes, observable by NMR, occurring in the local atomic structure or to model the local atomic structures which affect the quality of the films. Lizarraga et al. [130] attempted to use Density Functional Theory (DFT) to calculate NMR parameters for amorphous alumina using MD simulated structures for the first time; however, only the chemical shift was compared to experimental data for *am*- Al_2O_3 . The accuracy of their method depends on the number of nuclei used in the calculation, since each nucleus is weighted equally. However, most NMR spectra for disordered quadrupolar solids are simulated by the Czjzek model [137] which has been extended [138] to provide information on the distributions of electric field gradients (EFGs). In this chapter, we investigate the changes in the NMR parameters and local environment of amorphous

Al_2O_3 as a function of the annealing, by applying the extended Czjzek model and AIMD simulations. In addition, further proof for the combined use of MD and DFT to model amorphous alumina and other materials, besides the commonly done glasses, is presented.

9.2 Experimental

9.2.1 Molecular Dynamic Simulations of Structures

MD simulations were completed by the collaborators at Lawrence Berkely National Laboratory. They followed a melt-and-quench route to generate amorphous alumina. They first created a constrained random packed configuration of 40 Al and 60 O atoms with packmol [139] in a cubic box at a density approximately 20% larger than corundum ($\alpha\text{-Al}_2\text{O}_3$). This initial configuration was equilibrated as liquid Al_2O_3 at 3000 K and cooled down in a step-wise procedure using canonical (NVT) AIMD as implemented in Vienna Ab-initio Simulation Package (VASP) [140, 141] using Perdew-Burke-Ernezerhof (PBE) [142] formulation of generalized gradient approximation and a plane-wave kinetic energy cutoff of 400 eV, and Γ -point only. During cooling, isothermal MD runs at selected temperatures of 2500 K, 2000 K, 1773 K, 1573 K, 1373 K, 1223 K and 1073 K were performed. To ensure a near equilibrium density was obtained at each temperature, cell volume was dynamically modified every 4 ps until the average pressure dropped below 5 kbar, which was followed by a 10 ps long isothermal production run. Temperature transitions were done in a continuous cooling period of 4 ps. A time-step of 2 fs was used in all AIMD simulations. A 5-point Savitzky–Golay filter was applied to radial distribution functions (RDFs) and bond angle distribution functions (BDFs) to obtain a slightly smoother form.

9.2.2 CASTEP Simulations of NMR Parameters

NMR resonances for each Al nucleus were calculated using Cambridge Serial Total Energy Package (CASTEP) [143] as implemented by Materials Studio 2016. CASTEP is a DFT code which implements the gauge including projected augmented wave (GIPAW) method to simulate the all-electron wavefunction in the presence of a magnetic field, found in NMR experiments. The PBE functional was used with geometry relaxation of each MD derived structure to the ground state with a planewave cutoff energy of 630 eV. Ultrasoft pseudopotentials were used to describe the core-valence interactions. The calculations were allowed to run until the energy converged within 5×10^{-6} eV/atom.

To emulate the variations in local environment with the degree of relaxation of the amorphous phase, we quenched 10 configurations to 0 K using DFT relaxation of all geometrical degrees of freedom in CASTEP from two different temperatures of the AIMD cooling; namely, 1373 K and 1073 K. A maximum heteronuclear bond length of 2.45 Å was applied (value obtained from MD calculated RDFs to limit homonuclear bonds). Each nuclear resonance was then separated into 4-, 5-, or 6-coordinate Al species. The NMR parameters of each coordination environment were averaged together for each MD snapshot and then averaged for all the snapshots obtained from a given MD temperature. These values can then be used to obtain a calculated lineshape using the Dmfit [144] program which requires, for each coordination environment and temperature, the average percent signal intensity, average isotropic chemical shift, the standard deviation of the Gaussian chemical shift distribution, and the peak value of the quadrupolar coupling.

9.2.3 Synthesis and NMR Acquisition of Al₂O₃ Thin Films

The NMR data which we compare our results were adapted from Hammann et al. [145] where experimental specifics can be found. An overview of the synthesis and NMR acquisition of the Al₂O₃ thin films is presented here briefly. Thin films of Al₂O₃ are deposited on 100 μm thick, polished silicon wafers by spin casting from molecular clusters [146]. The molecular clusters are passed through 2 μm filters and soft-baked until ten layers are formed for a film thickness of ≈380 nm. Each film was then further annealed in a furnace under ambient conditions at different temperatures up to 1100 °C which had a final thickness of ≈270 nm.

The silicon wafer coated with the *am*-alumina was then crushed to a coarse powder using mortar and pestle with the film still attached to the wafer as shown previously by scanning electron microscopy [145]. For NMR, The coarse powder was loaded into a 3.2 mm rotor and spun at the magic angle at 22.5 kHz. ²⁷Al ($I = 5/2$) was acquired in a 19.96 T magnet with a resonance frequency of 221.41 MHz. The spectra were referenced with respect to 1 M Al(NO₃)₃ at 0 ppm. The spectra were acquired using a 90°- τ -180° rotor synchronized quadrupolar echo [98] with a central selective 90° pulse length of 2.25 μs. The spectra were collected using 5400 transients with a 1 s recycle delay. The probe background was subtracted, and the resulting spectra are shown in Figure 9.1. The two lowest annealing temperatures, 200 °C and 300 °C, contain many impurities (primarily water and nitrates) left over from the synthesis method and thus would not be described by our modeling of pure Al₂O₃. The two highest annealing temperatures, 950 °C and 1100 °C, correspond to crystalline phases of alumina. The 400 °C to 800 °C spectra are, thus, the amorphous region we are modeling.

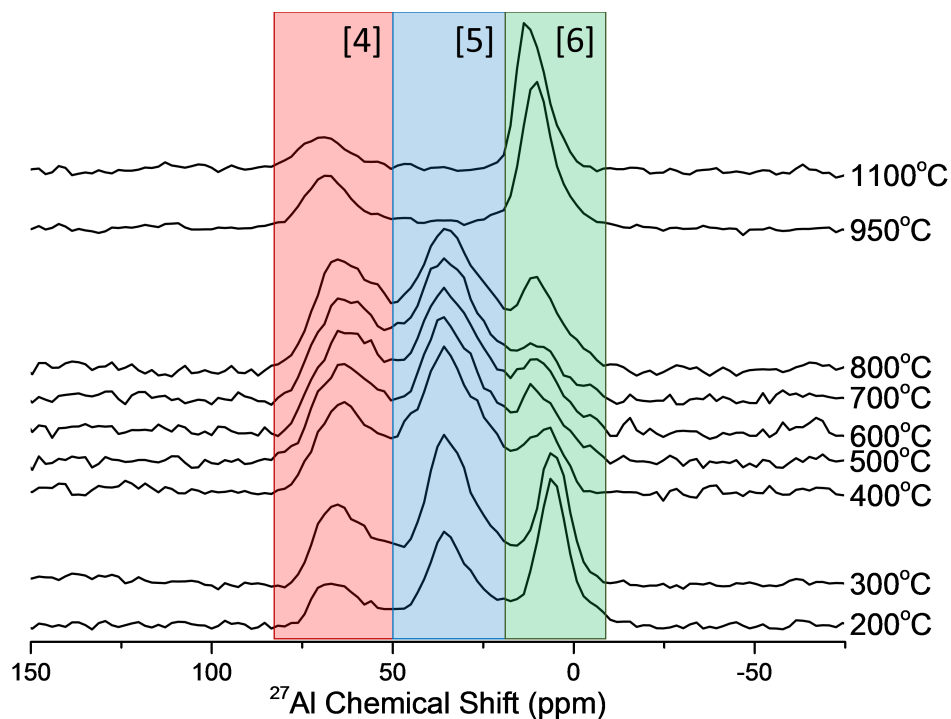


Figure 9.1: ^{27}Al MAS NMR spectra acquired using a rotor synchronized selective quadrupolar echo pulse sequence as a function of annealing temperature. Three distinct peaks are observable, corresponding to 4-, 5-, and 6-coordinate Al in red, blue and green, respectively.

9.3 Results and Discussion

9.3.1 Amorphous Structures of Aluminum Oxide

The AIMD-based melt-and-quench route to obtaining amorphous materials follows a physically plausible path analogous to an experimental cooling process from the liquid phase. While the cooling rate is still much higher than typical rates in experiments, we expect the method to capture the prevailing short-range order in amorphous Al_2O_3 much better than a stochastic generation method.

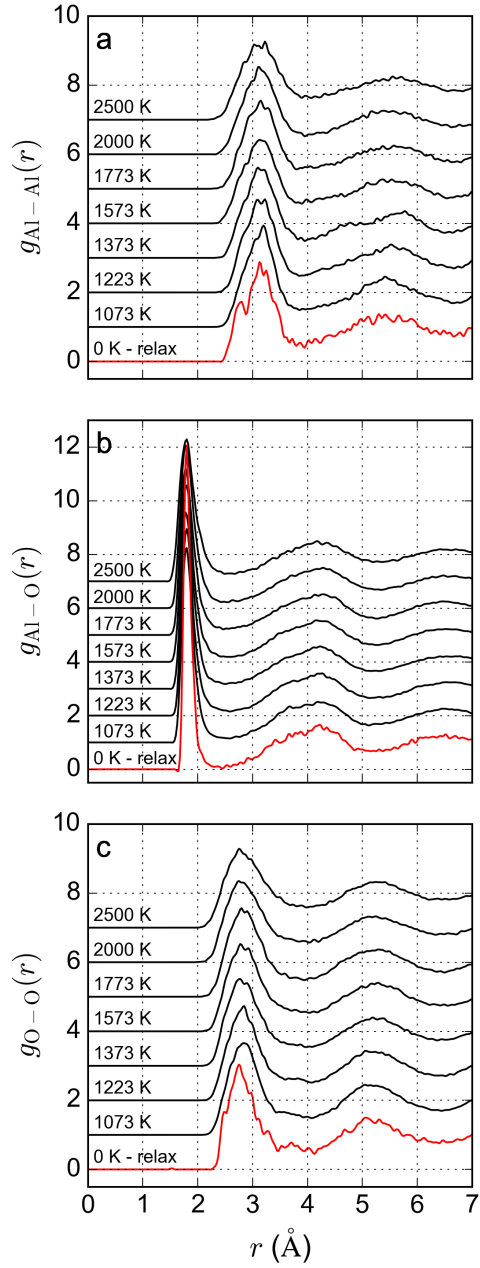


Figure 9.2: Partial RDFs of Al_2O_3 as a function of temperature upon cooling down the melt from 2500 K, along with the averages of snapshots quenched to 0 K by DFT relaxation (0 K - relax). Panels (a), (b), and (c) show RDFs of Al-Al, Al-O and O-O pairs. $g(r)$ is shifted by +1 incrementally for each temperature step above 0 K.

The partial RDFs of alumina as it is cooled down from the liquid are shown in Figure 9.2. The positions of first peaks (average distance to closest corresponding nucleus) of Al-Al, Al-O and O-O do not change considerably with temperature, and are in excellent agreement with the experimental reports for liquid and amorphous Al_2O_3 [120, 147]. The only noticeable changes are that the first peak of Al-O pairs becomes significantly sharper, and all peaks become slightly narrower and shift towards smaller interatomic separations, as expected from densification at lower temperatures. This is also consistent with the BDFs shown in Figure 9.3, where the intensity of the peak around 90° of O-Al-O bonds increases as the temperature is lowered, hinting at the relaxation from lower to higher coordinated AlO_n polyhedra.

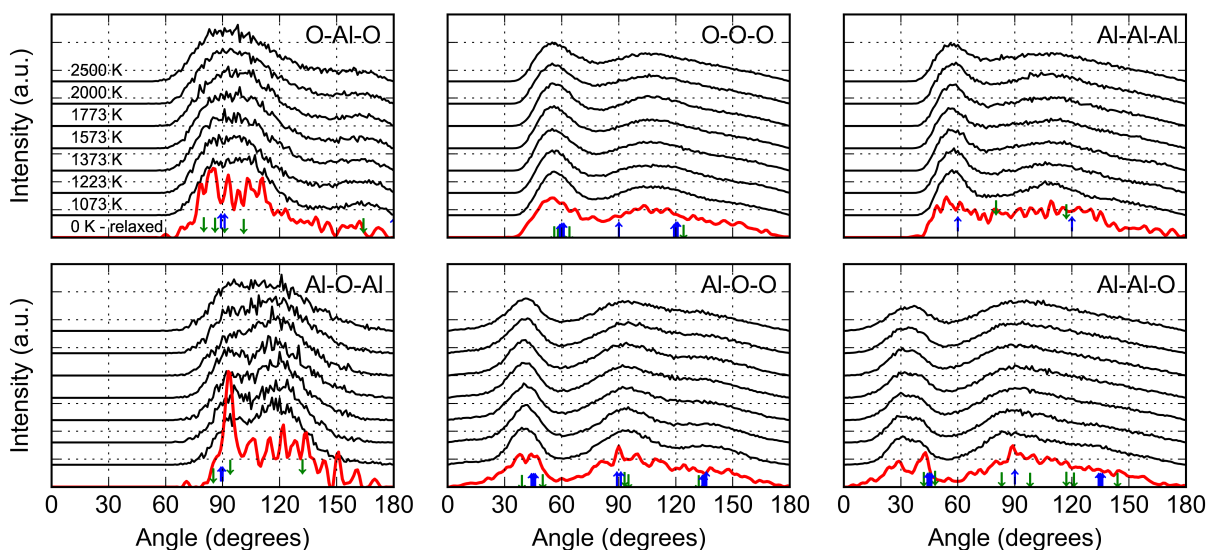


Figure 9.3: Bond angle distribution functions of triplets in liquid and amorphous Al_2O_3 . Starting from 0 K DFT-relaxed snapshots, functions are shifted upwards with the same increments for each temperature step. For comparison, major bond angles in α and γ - Al_2O_3 are also shown as downward and upward arrows, respectively.

9.3.2 NMR Parameters of Amorphous Structures

The NMR parameters are expected to be sensitive to the degree of local order established in the *am*-Al₂O₃. Therefore, we focus on atomic configurations from AIMD simulations at two distinct temperatures (1073 K and 1373 K), which exhibit slightly different degrees of relaxations in the Al-O local environment. The resulting average values of the NMR parameters for the full (geometry and energy) optimization of the 10 MD simulations per temperature can be seen in Table 9.1. The structures obtained from the lower temperature MD simulation may have slightly more 4- and 6-coordinate Al than those obtained from the higher temperature MD simulation (uncertainty too large to fully make claim), which trends towards that of the pure γ -Al₂O₃ crystal structure which exhibits only 4- and 6- coordinate Al [136]. In addition, the standard deviation of the NMR parameters decreases for the lower MD temperature, indicating a more ordered structure.

The only other attempt in calculating amorphous alumina from MD and further DFT calculations, only used the nuclei present in the unit cell [130]. In this work, by implementing a known model, which describes an infinite distribution of amorphous quadrupolar nuclei, the expected lineshape for an infinitely large unit cell can be calculated from the sets of calculations. This method, while faster than calculating a much larger unit cell, should also be more accurate as it minimizes the effect of nuclei near the edge of the unit cell, which can cause some unexpected results.

The NMR parameters obtained for the three coordination environments in the Czjzek model include percent, δ_{iso} , FWHM of δ_{iso} , $|C_q|$, as well as δ_{aniso} , η_{CS} , and η_Q . Percent is the percentage of nuclei in all the snap shots for a given MD simulation temperature which have the corresponding coordination number. δ_{iso} is the average isotropic chemical shift from the

Table 9.1: CASTEP NMR parameters results for 4-, 5-, and 6-coordinate Al for the amorphous Al_2O_3 structures obtained from two selected MD simulation temperatures. The first four columns of results are those used to model the Czjzek NMR lineshapes. The values given are the average of 10 snapshots for each temperature. The error shown is the standard deviation between the 10 results.

MD Sim.	Percent	δ_{iso}	FWHM	$ C_q $	δ_{aniso}	η_{CS}	η_Q	
Temp.	(%)	(ppm)	δ_{iso} (ppm)	(MHz)	(ppm)			
1073 K	[4]	44 ± 2	64 ± 1	7.4 ± 0.6	9.6 ± 0.1	44 ± 2	0.55 ± 0.02	0.53 ± 0.06
	[5]	45 ± 3	40 ± 1	6.9 ± 0.5	9.8 ± 0.2	62 ± 1	0.61 ± 0.02	0.61 ± 0.04
	[6]	12 ± 1	18 ± 1	5.4 ± 0.6	10.7 ± 1.0	26 ± 3	0.66 ± 0.11	0.59 ± 0.09
1373 K	[4]	43 ± 4	68 ± 1	7.2 ± 0.9	10.8 ± 0.6	46 ± 4	0.58 ± 0.07	0.58 ± 0.08
	[5]	48 ± 4	43 ± 1	6.1 ± 0.8	9.3 ± 0.5	58 ± 4	0.58 ± 0.09	0.59 ± 0.05
	[6]	9 ± 3	18 ± 2	6.4 ± 3.3	8.5 ± 1.7	24 ± 7	0.61 ± 0.08	0.59 ± 0.16

average chemical shift of each of the ten snapshots. The position of the peak and thus the splitting between the different coordination peaks is determined by δ_{iso} . The FWHM of δ_{iso} is the average of the FWHM of the isotropic chemical shift distributions in each snapshot and is a Gaussian broadening mechanism. $|C_q|$ is the average/most common quadrupolar coupling constant from all of the snapshots and describes the length of the tail in the Czjzek model. The last three parameters are not used in the Czjzek model but are informative values that can be calculated. δ_{aniso} is the average anisotropic portion of the chemical shift from all the snapshots, which is not of interest here due to the magic angle spinning to remove it. η_{CS} is the chemical shift asymmetry parameter and η_Q is the quadrupolar asymmetry parameter, which are averaged over all the snapshots as well.

Using the first four columns of NMR parameters in Table 9.1, a calculated lineshape can be constructed for the amorphous alumina assuming the distributions of quadrupolar parameters fit the Gaussian Isotropic Model (GIM) for a Czjzek distribution. By assuming

a Czjzek distribution, which has been used to fit many amorphous quadrupolar NMR signals [137, 148], a smooth continuum for the lineshape can be reached without the need for large unit cells. The resulting spectra for the structures obtained from two different MD temperatures result in slightly different lineshapes as seen in Figure 9.4. It is important to note, NMR is very sensitive to the local structure, allowing for observable changes in the spectra, which is not as noticeable in the table of resulting parameters.

9.3.3 Comparison of Calculated and Experimental NMR Lineshapes

In order to confirm accurate computational modeling of the local atomic structure in *am*-alumina, comparison of the calculated and experimental data must be made. The two resulting Czjzek models were compared to experimental spectra from the five annealing temperatures of interest for amorphous alumina. For each comparison, the 5-coordinate calculation and 5-coordinate experimental chemical shifts were overlapped to reference the calculations since the 5-coordinate peaks are the most intense, and thus, most accurately known. During this referencing, the separation of the 4-, 5-, and 6- coordinate Al isotropic chemical shifts were kept constant. The two MD simulation temperatures resulted in better matches with two separate experimental annealing temperatures, indicating this method may be able to model the small changes as the amorphous structure rearranges to become crystalline. The best match between experimental and calculation can be seen in Figure 9.5.

The 1373 K calculated lineshape best matches the 400 °C annealing temperature (Figure 9.5(a.)). The two main differences between calculation and experimental is the smaller calculated chemical shift separations between the different coordinations in the calculate

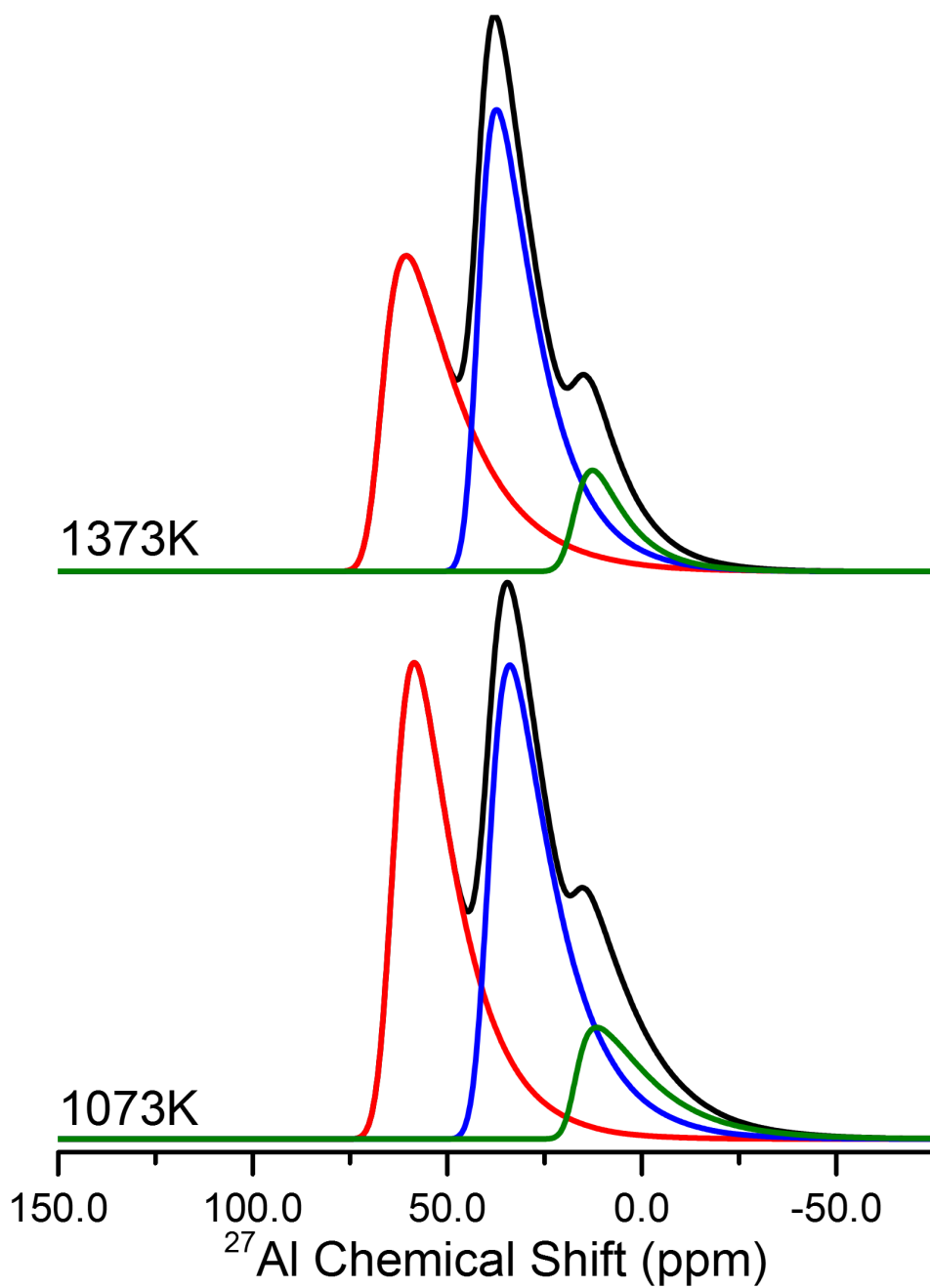


Figure 9.4: Resulting geometry optimized Czjzek lineshapes from the calculated NMR parameters for the two molecular dynamics simulations. The 4-, 5-, and 6-coordinate (red, blue, and green, respectively) are shown as well as the sum (black).

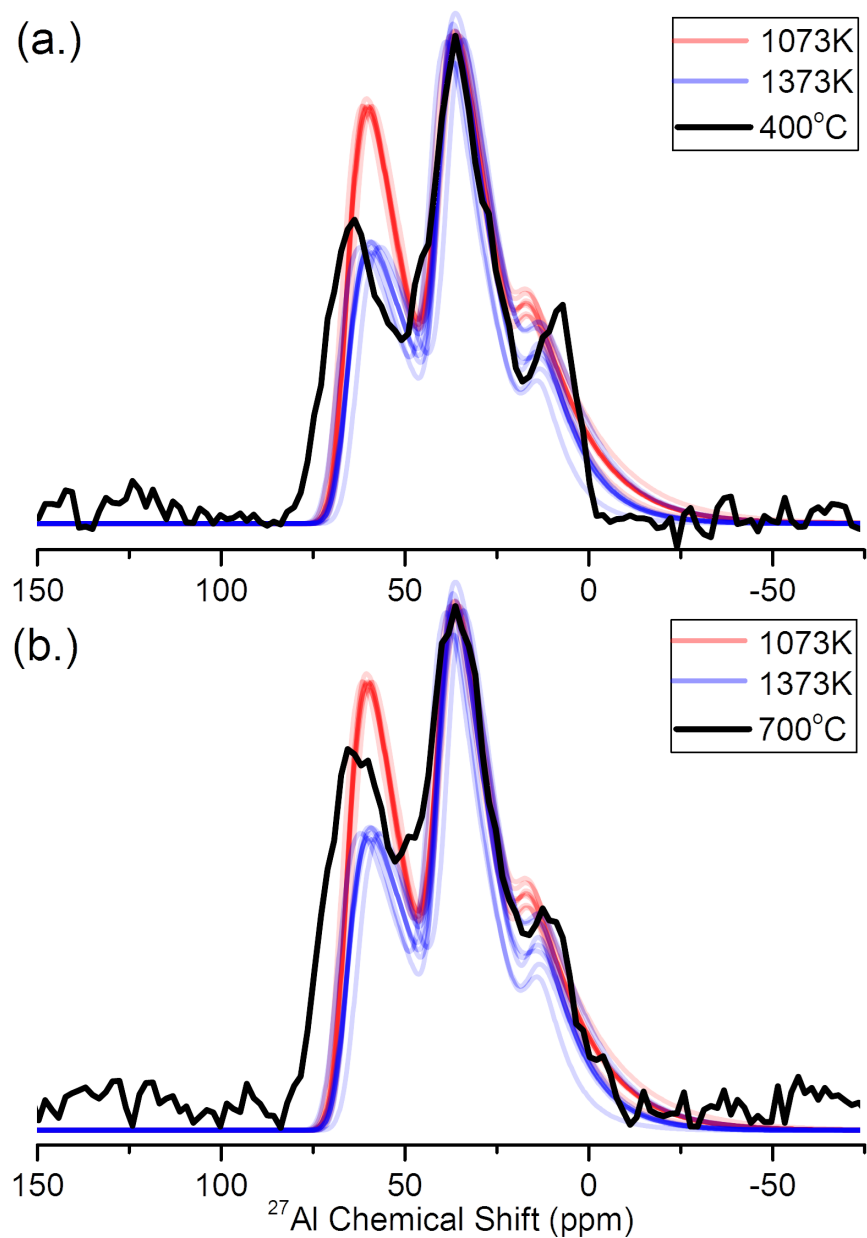


Figure 9.5: Best matches between experimental and calculated results. The multiple lines for the calculated spectra represents the expected spectrum within one standard deviation for each variable. (a.) Comparison of 400 °C experimental data to the two temperature calculation results illustrating the match between 400 °C experimental and 1373 K (blue) calculations. (b.) Comparison of 700 °C experimental data to the two temperature calculation results illustrating the match between 700 °C experimental and 1073 K (red) calculations.

spectrum and the lack of a tail to lower ppm values for the experimental 6-coordinate aluminum in the experimental spectrum. The smaller chemical shift separations could be due to inappropriate energy levels of the electron orbitals present, similar to that observed in Ca glasses [149], leading to errors in chemical shifts or due to a non-ideal correlation of shielding and chemical shift as observed in many other systems [143, 149, 150]. The lack of the typical Czjzek tail for the 6-coordinate experimental resonance could be due to incomplete removal of the water and nitrates used in the synthetic procedure, which is not taken account in these simulations.

The 1073 K calculated lineshape best matches the 700 °C annealing temperature (Figure 9.5(b.)). A similar discrepancy in the chemical shifts is also observed; however, the tail for the 6-coordinate aluminum resonance matches well. Instead, the 4-coordinate resonance height is slightly higher than the experimental and a small lack of intensity between the 4- and 5-coordinate resonances appears. This could be an under calculation of resonance width by CASTEP calculations or could be indicative of a better match with an annealing temperature between those measured here where the 4-coordinate aluminum would have slightly different NMR parameters.

The inverse relationship between MD simulation temperature and annealing temperature can be understood considering the nature of the simulations and experiments, which approach the more locally-ordered structures from different directions on the temperature scale. The MD simulation method used here, starts with a liquid phase of Al_2O_3 and slowly cools the structure to a relatively high temperature before a faster quench. Thus, a higher quenching temperature would lead to more disorder in the structure while a lower temperature quench would have allowed further relaxation and a more ordered local structure. The annealing process raises the temperature to a higher temperature to allow for mobility of the nuclei

before cooling back to room temperature. The higher the temperature, the more motion the nuclei are allowed to undergo before a slow cooling process to form the film. More motion will allow the sample to overcome thermodynamic barriers until it ultimately reaches the lowest energy crystal structure. Ultimately, this indicates the formation of short range order, such as micro-crystallites, forming in the simulated spectra, as expected for the temperatures near the transition to a crystalline phase.

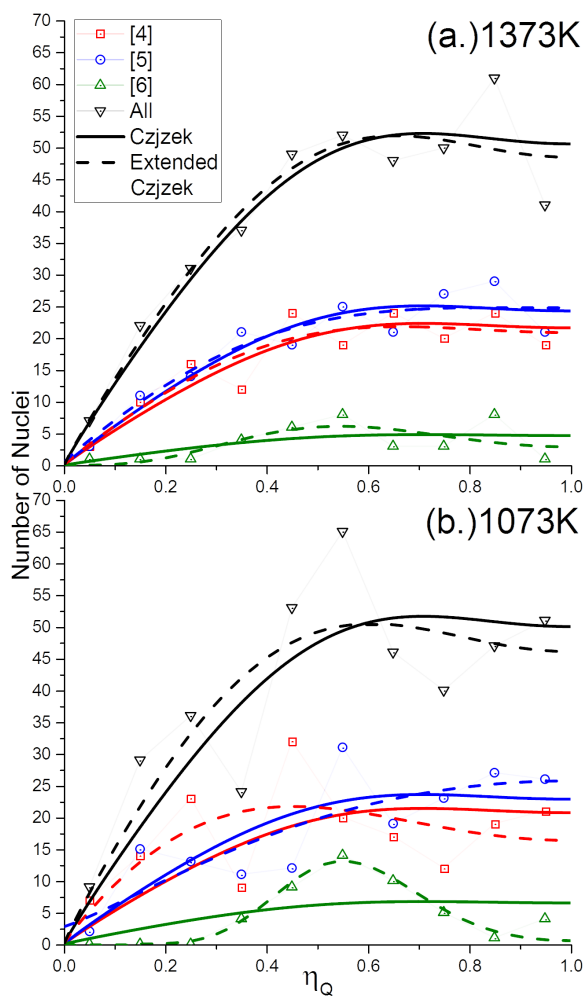


Figure 9.6: Quadrupolar asymmetry parameter (η_Q) distributions from the resulting MD/CASTEP unit cells for the (a.) 1373 K and (b.) 1073 K amorphous alumina simulations. The solid lines represent fits to the distributions using the standard Czjzek model. The dashed lines represent fits to the distributions using the extended Czjzek model.

To confirm the use of the Gaussian Isotropic Czjzek Model lineshapes, an extension [138, 148] of the Czjzek model was used to analyze the MD-simulated, CASTEP-optimized structures. The extended model does not assume an isotropic Gaussian distribution of the quadrupolar tensor which allows for structural information of the sample to be obtained. The comparison of the two models for the distribution of the η_Q parameter for every nuclei (from all ten snapshots, for a given temperature) can be seen in Figure 9.6. For the 1373 K simulation, the GIM and extended model are almost identical. This is indicative of a truly amorphous and random structure. However, for the 1073 K simulations, the distribution of η_Q can no longer be simply modeled with a GIM Czjzek model, especially for the 6-coordinate aluminum. This indicates the 6-coordinate Al resonances are dominated by local contributions rather than the global isotropic contribution of the GIM [148], for these simulated structures. This is indicative of a transition to a more ordered structure.

One of the ten example structures obtained for the two temperatures can be seen in Figure 9.7. The structural change between the two is hard to see by eye. However, additional 6-coordinate is observed in these representative structures in addition to the formation of some tetrahedral shaped polyhedra (rather than highly distorted four coordinate Al) in the 1073 K (b.) simulation. This corresponds well to the larger percentage of 6-coordinate Al and the narrowing of the 4-coordinate Al species observed in the NMR spectrum simulation and in the higher annealing temperature experimental NMR data. As can be seen, NMR is very sensitive to these geometries as shown in the calculated and experimental lineshapes.

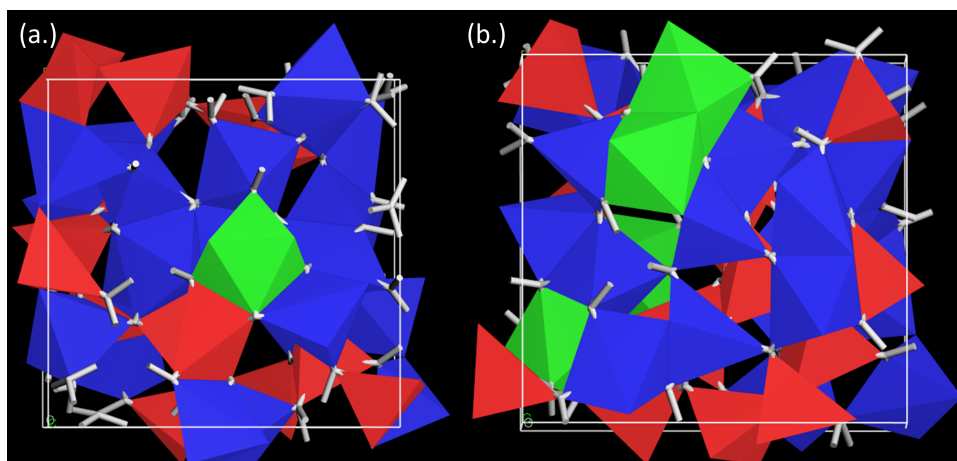


Figure 9.7: Representative structures of the amorphous Al_2O_3 at MD quenching temperatures of (a.) 1373 K and (b.) 1073 K. The white lines are the oxygen atom bonds and the red, blue, and green polyhedra are for the 4-, 5-, and 6-coordinate aluminum atoms, respectively.

9.4 Conclusions

MD simulations have been used to create large amorphous unit cell structures of Al_2O_3 while using the quench temperature to control the disorder. DFT relaxation to the lowest local energy minimum and subsequent NMR simulations were completed via CASTEP for two of the MD quench temperatures believed to be the most similar to the amorphous structure of alumina. The calculated NMR parameters were used to obtain lineshapes for the expected Czjzek model (assuming a Gaussian isotropic distribution of nuclear sites). The temperature of the MD quenched simulated spectra were inversely related to the annealing temperature of the experimental amorphous alumina NMR spectra. This correlates well with the expected order and crystallinity for both calculation and experiment. In addition, comparison to the extended Czjzek model shows local order becoming dominant in the lower temperature MD quenches, especially for the six coordinate aluminum nuclei. This correlates well to the expected growth of micro-crystallites for nucleation as expected for the annealing

temperatures approaching the crystallization temperature. Ultimately, an excellent match to the NMR spectra and expected short range order is obtained.

Chapter 10

Conclusions and Future Directions

10.1 Conclusions

OPNMR has proven to be of interest with respect to fundamental science and for advancing the understanding of spin physics. The basic understanding of OPNMR was advanced by the design and fabrication of an affordable and simple two-channel OPNMR probe which is able to perform as needed, even in the non-ideal horizontal orientation of the cryostat. In addition, a better understanding of the optical pumping phenomena in CdTe was made more clear after the two previous research studies produced strongly contradicting data. Of note, is the first measurements of optically pumped nuclear polarizations reaching $\approx 90\%$, much greater than the previous measurements hovering around a maximum of $\approx 35\%$.

The use of the hyperpolarization from optical pumping as an application for analytical experiments in other fields has been rather limited. However, through my work as a graduate student, many examples of applications for OPNMR are now available. Using OPNMR, one can now accurately measure the energy to excite to the lowest level light-hole state which is difficult to measure by traditional optical means. In addition, OPNMR has been proven to be

a technique for accurate measurements of couplings and the effect of laser excitation on said couplings for spintronics and quantum computing applications. The accuracy of optically pumped SEDOR (with and without cross polarization) will be imperative in measuring the couplings in these systems reliably, especially for monitoring minor changes. The proven ability to now measure effects near the interface will be imperative to allow for analysis of interface properties by NMR. This will allow for advancements in electronic devices and the ability to study other buried interfaces.

10.2 Future Directions

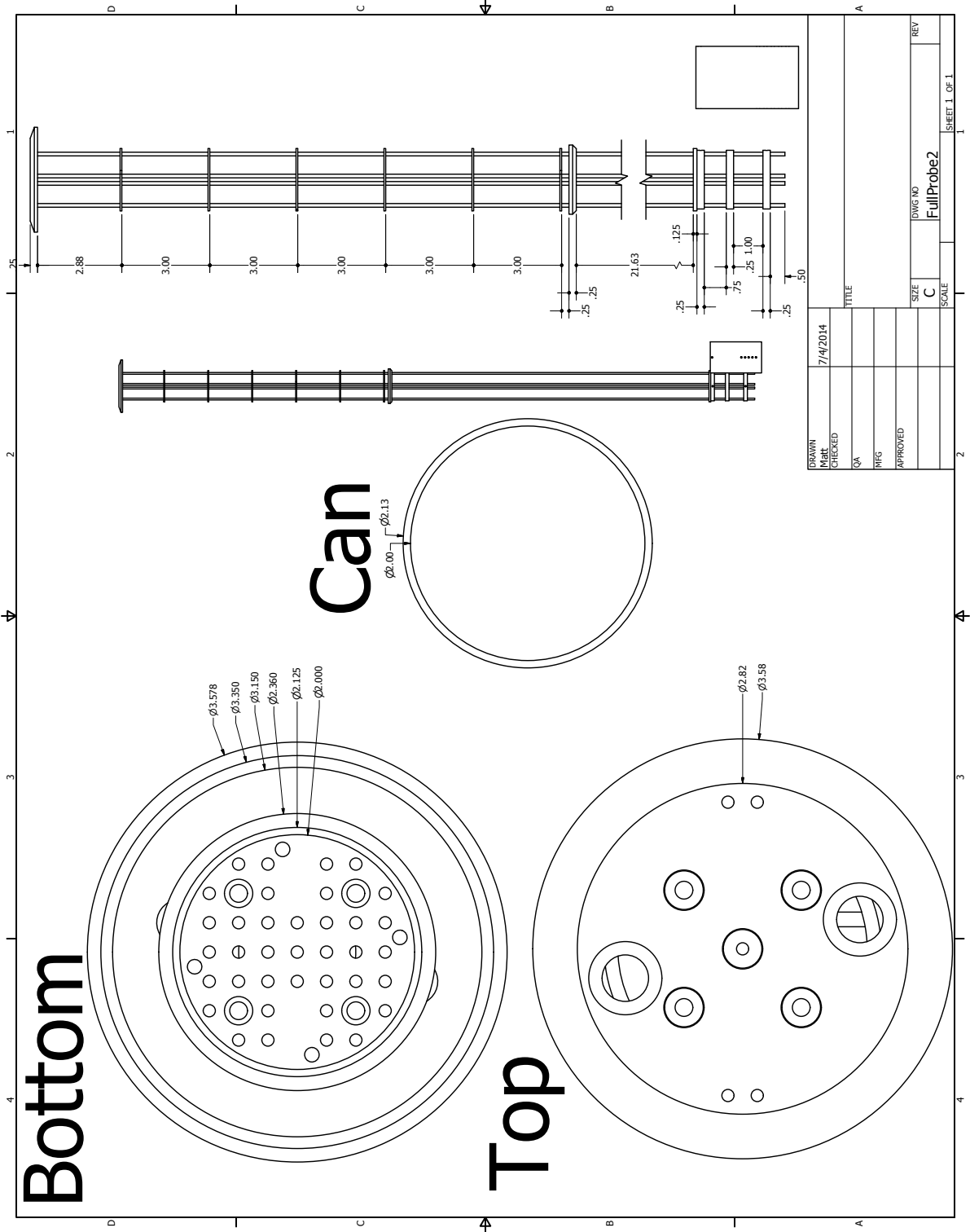
With the advancements of potential applications for OPNMR, a large amount of studies can now be completed. For instance, how would the presence of a crystalline film affect the strain and thus polarization? Or, can the amount of strain relaxation be tuned by film deposition parameters to optimize and provide the most accurate depth information? And, how can one achieve the highest polarization at the interface for very accurate interface information? Many of the methods presented in this dissertation will help make the necessary advancements in order to make OPNMR a useful analytical technique. In addition, modeling of the strain as a function of depth can provide insight into the depth dependence of the polarization. One could then model the polarization as a function of depth and thus observe how the polarization changes as a function of time at various depths. However, further understanding of the mechanisms leading to the shape of these satellites (besides strain as a function of depth) will need to be understood. Ultimately, once a clear understanding of the polarization at and near the interface is better understood, a different (ideally, a spin-1/2) semiconducting substrate can be used to transfer the polarization to surface bound

films/ligands. The transfer of the polarization has been one of the most sought after goals for OPNMR to become an imperative analytical technique.

Appendix A

2 Channel Probe Drawings

Complete probe and individual part designs used for the fabrication of the two channel probe are on the following pages.

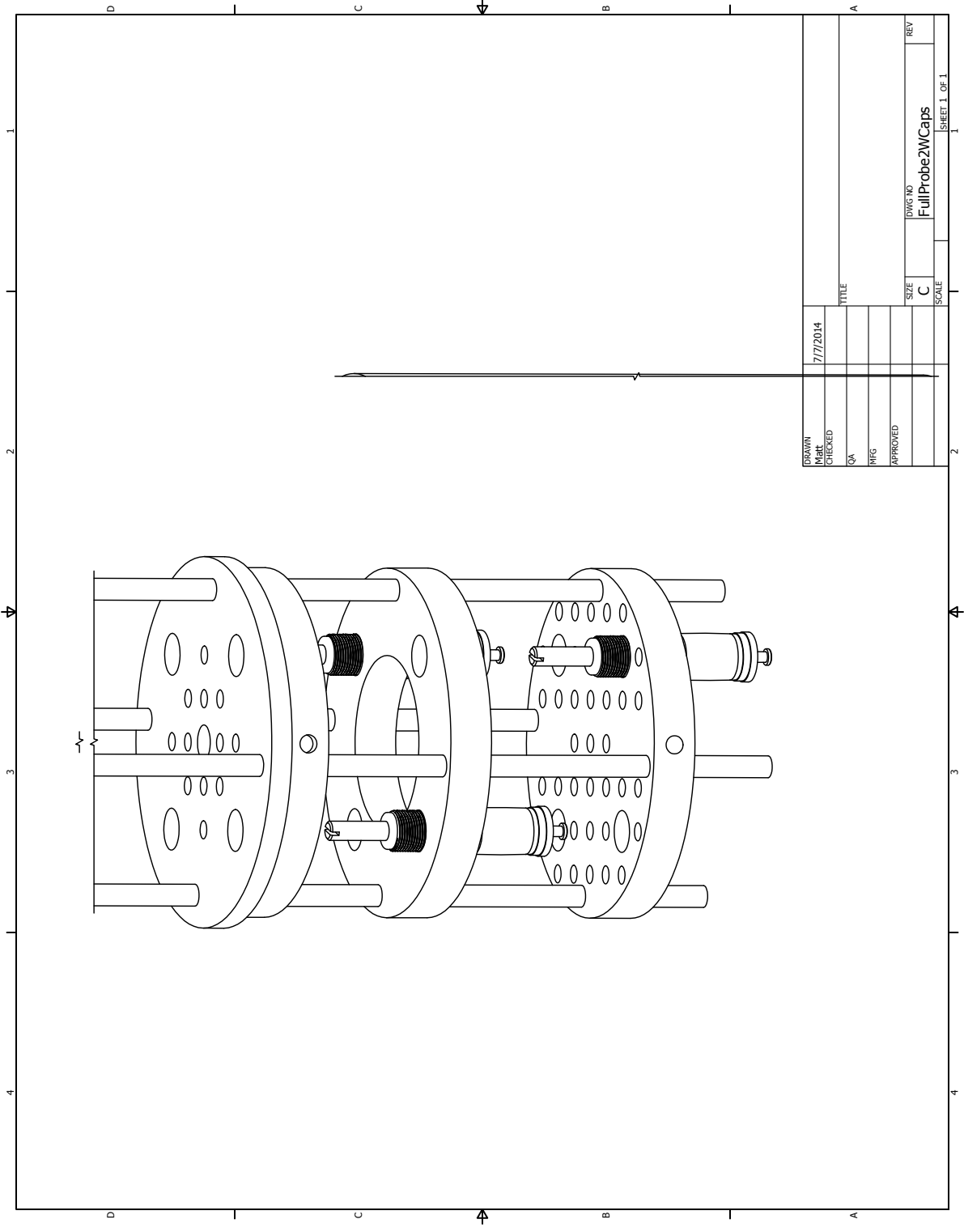


DESIGN	7/4/2014	TITLE	
ISSUED			
CHECKED			
QA			
PROBING			
APPROVED			
SIZE	C	DWG NO	FullProbe2
SCALE			
			REV
			SHEET 1 OF 1

Bottom

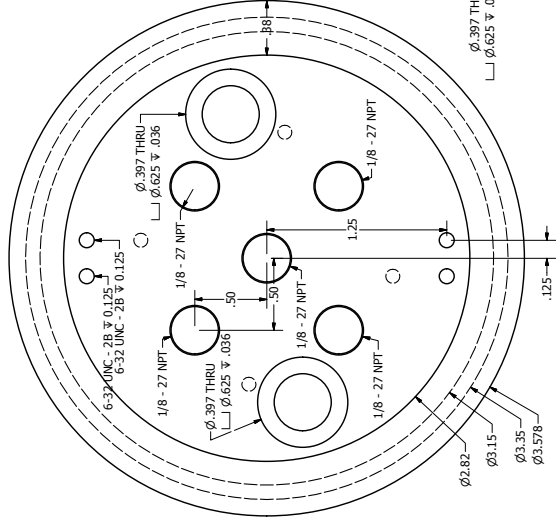
Top

Can



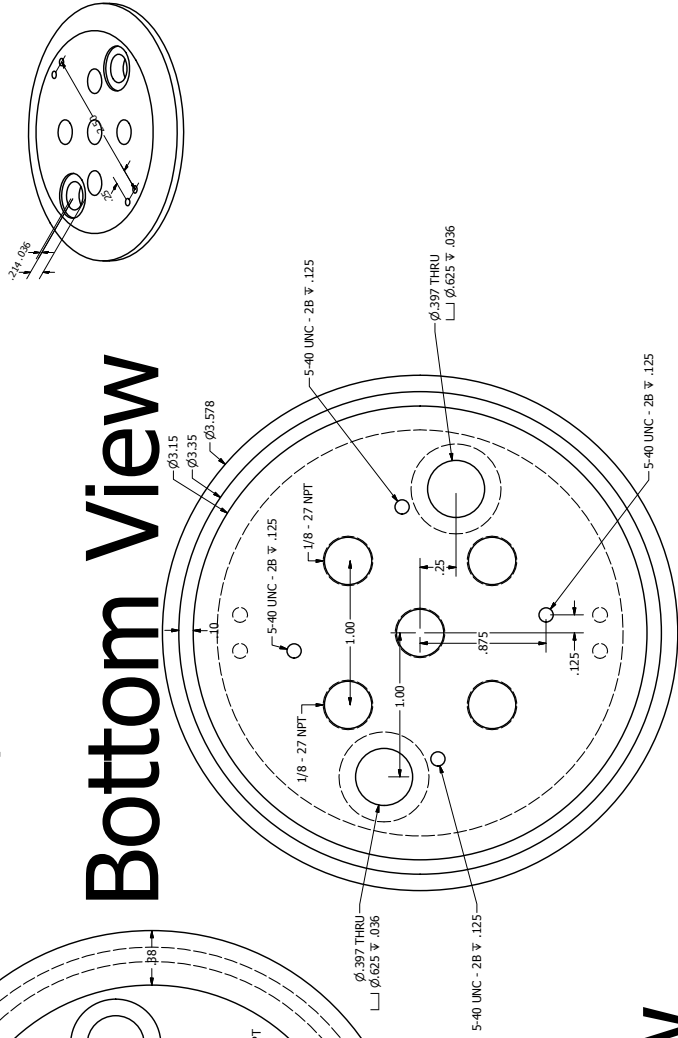
DESIGN	7/7/2014	TITLE	
ISSUED		SIZE	C
CHECKED		SCALE	
QA		FIGS NO	FullProbe2WCaps
APPROVED		REV	
		SHEET 1 OF 1	

Top View

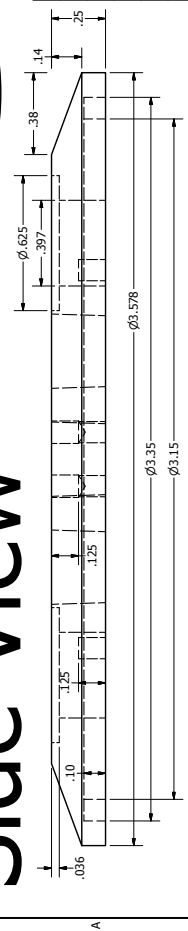


Solid flange will be provided
 Holes and threads need to be added
 Material: Stainless Steel
 Quantity: 1

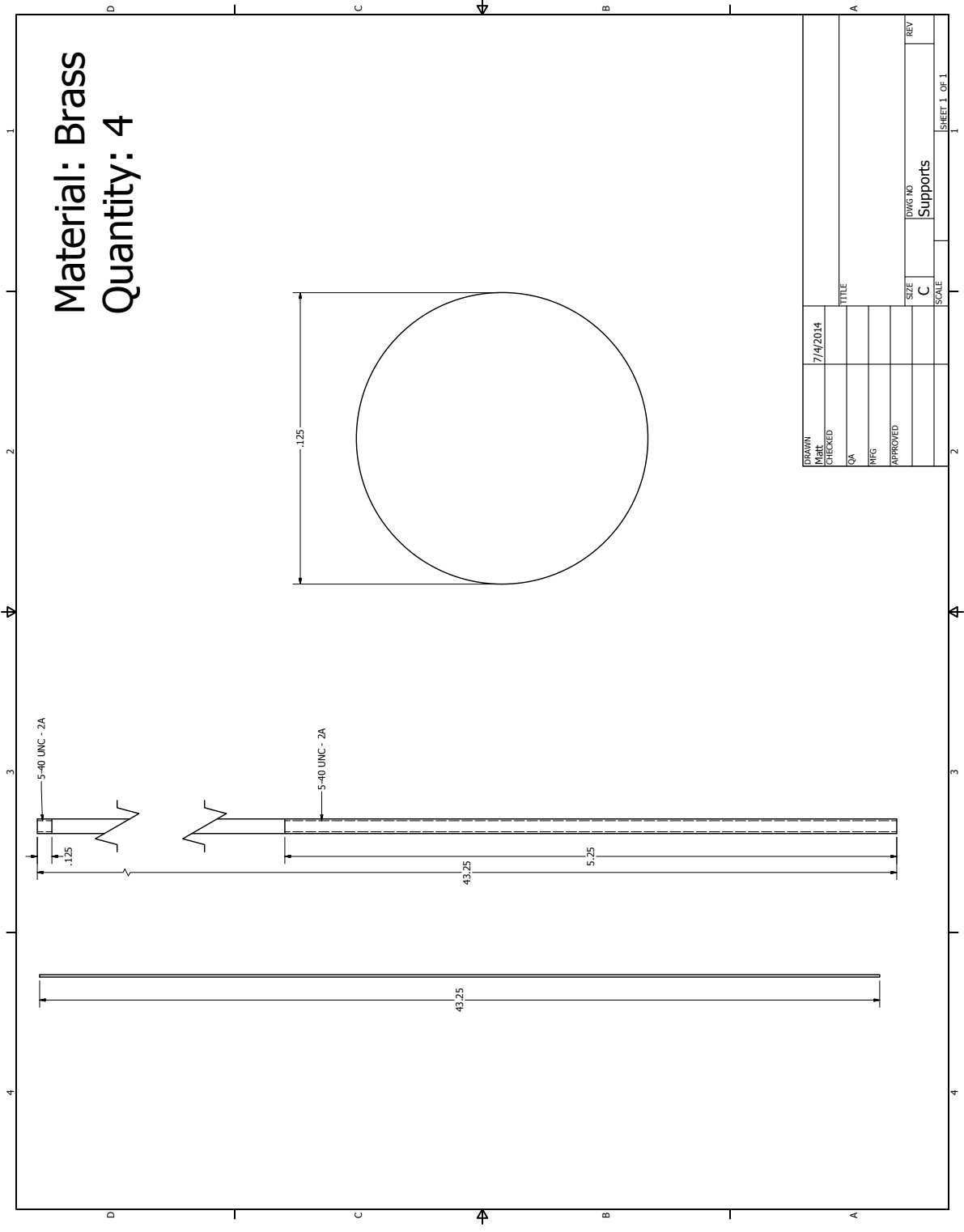
Bottom View



Side View



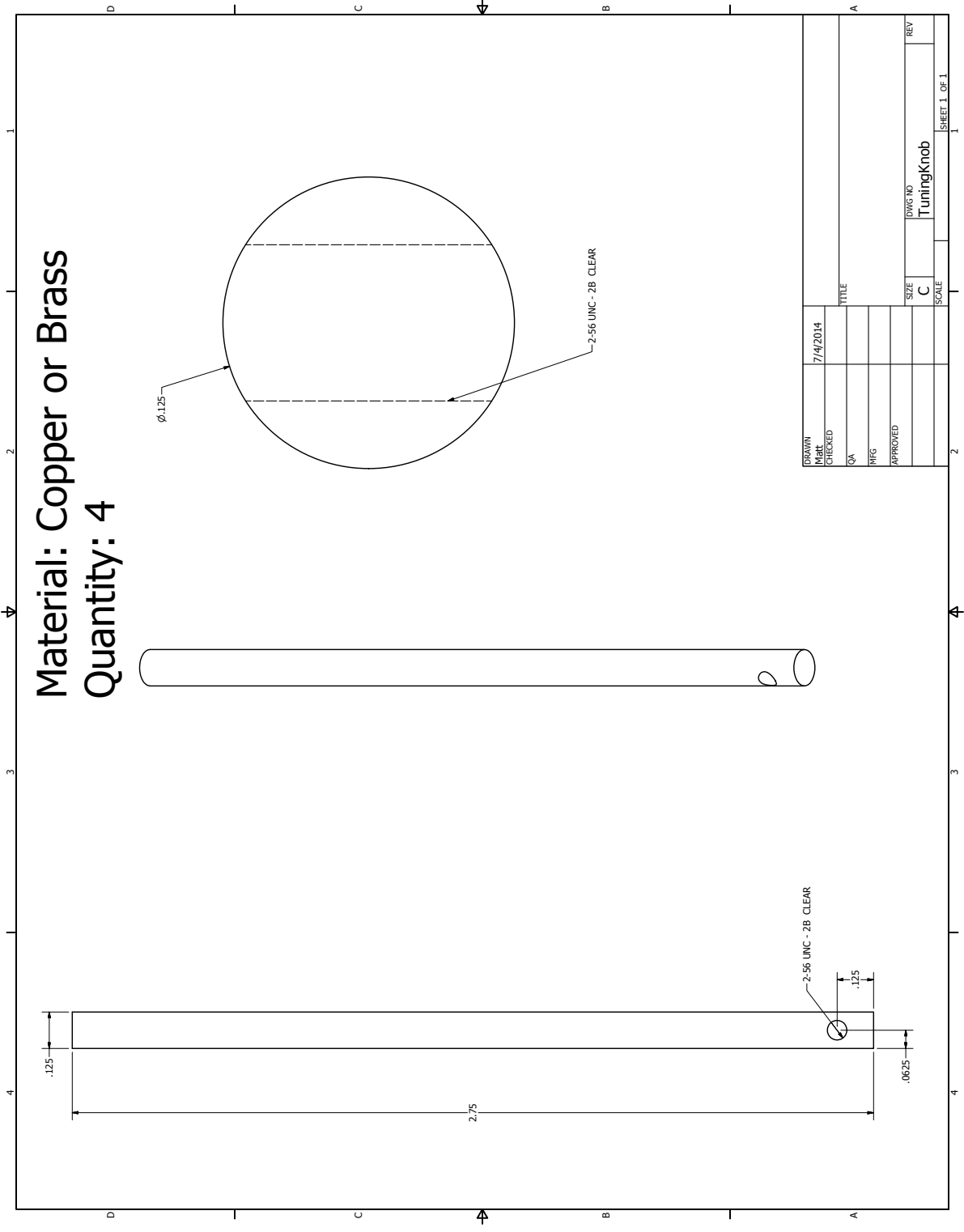
DESIGNED	7/4/2014	TITLE
CHECKED		
QA		
DRG NO		
APPROVED		
REV		
SIZE	C	TopHat
SCALE		
SHEET 1 OF 1		



Material: Brass
Quantity: 4

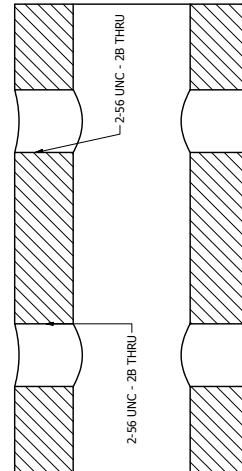
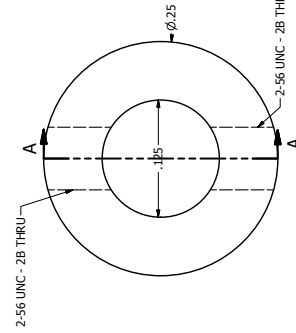
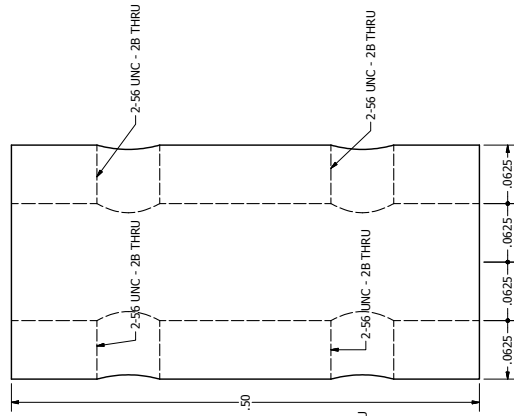
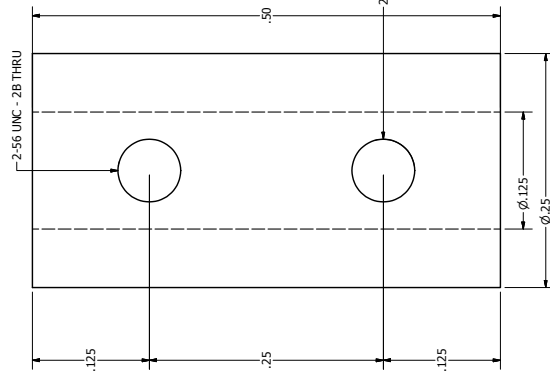
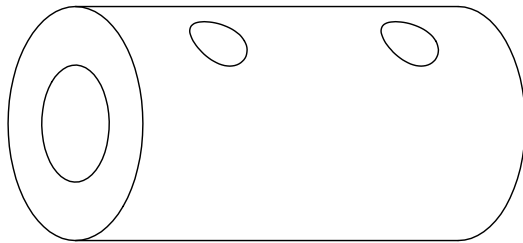
DESIGN	7/4/2014	TITLE	
DATE			
CHECKED	QA		
BY			
APPROVED			
		SIZE	C
		SCALE	
		DWG NO	Supports
		REV	
			SHEET 1 OF 1

Material: Copper or Brass
Quantity: 4



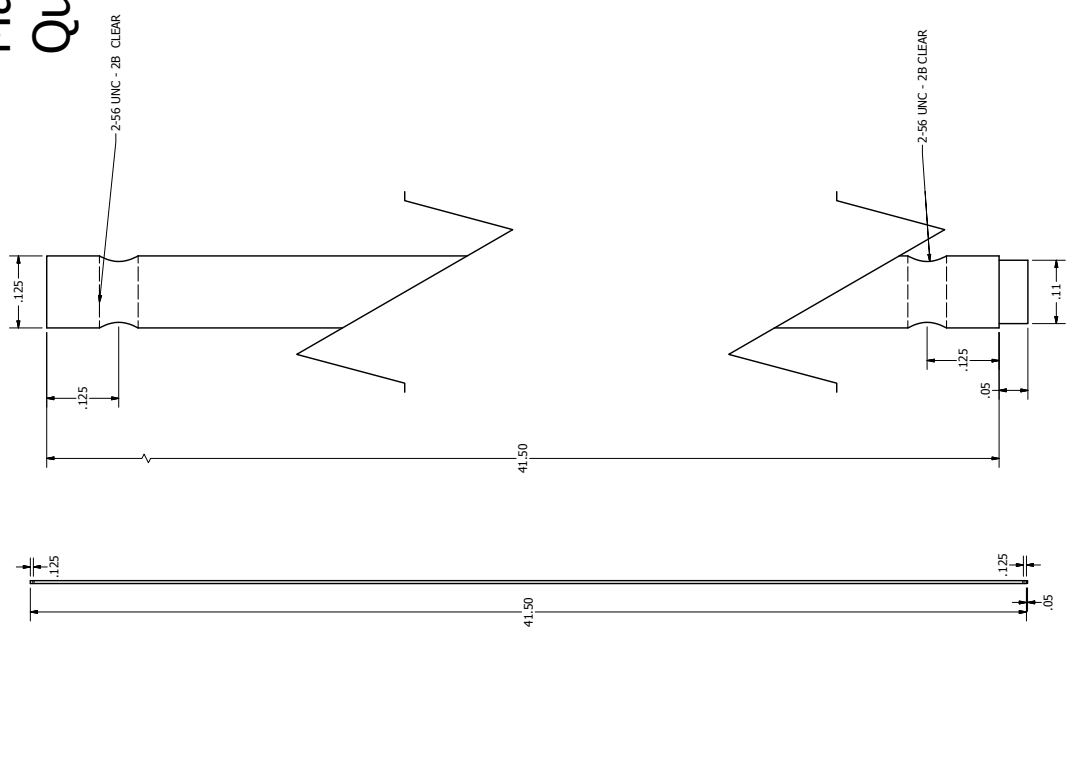
DESIGN	7/14/2014	TITLE	
ISSUED		DATE	
CHECKED		SCALE	
QA		SIZE	C
PHG		DRWG NO	TuningKnob
APPROVED		REV	
		SCALE	
			SHEET 1 OF 1

Material: Copper or Brass
Quantity: 8

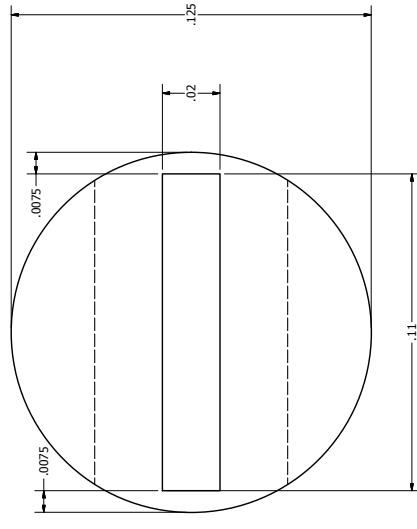


DESIGN	7/4/2014	TITLE	
ISSUED			
CHECKED	QA		
APPROVED	RING		
		SIZE	
		C	
		SCALE	
		DWG NO	
		Couplers	
		REV	
		SHEET 1 OF 1	

Material: G10 fiberglass or similar
 Quantity: 3

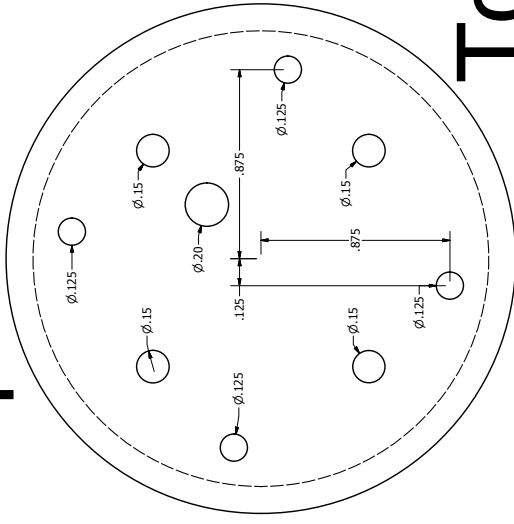


Bottom View



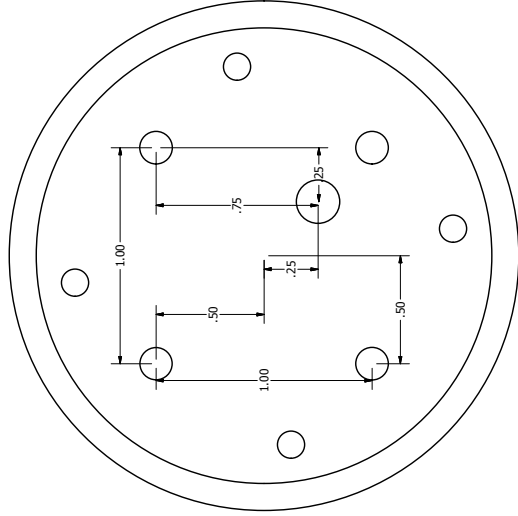
DESIGN	7/4/2014	TITLE	
ISSUED		QA	
CHECKED		PHG	
APPROVED		SCALE	
		SIZE	C
		DWG NO	TuningRodsAlternate
		REV	

Top View

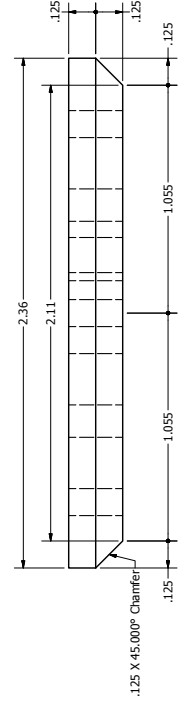
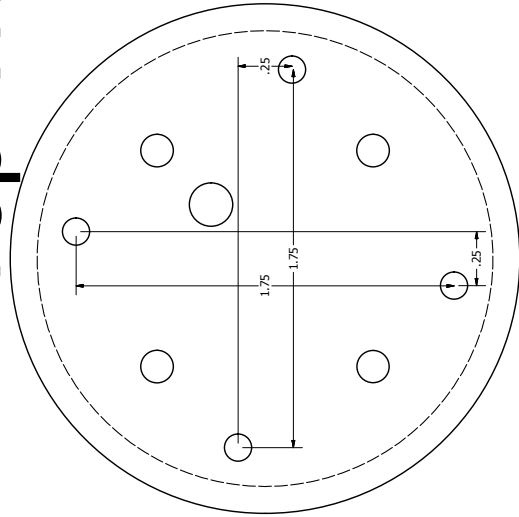


Material: G10 fiberglass or similar
Quantity: 1

Bottom View



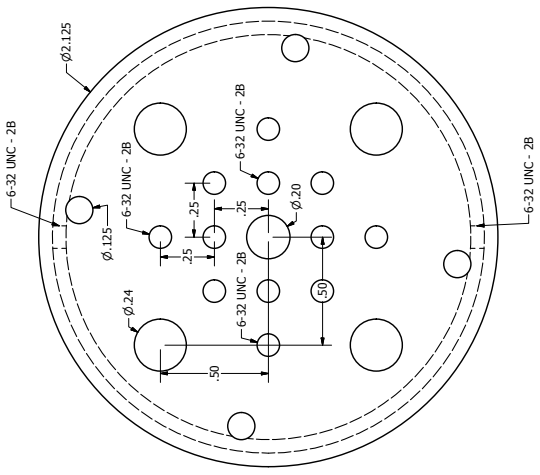
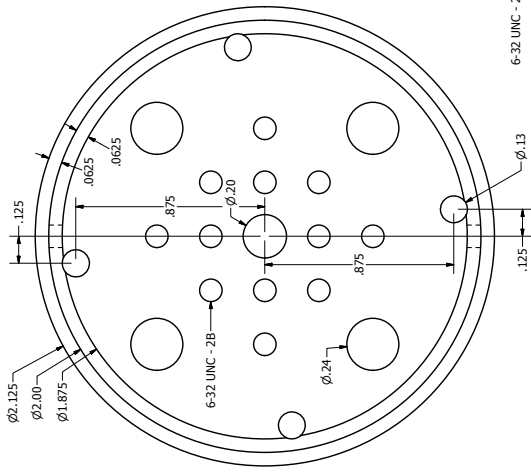
Top View



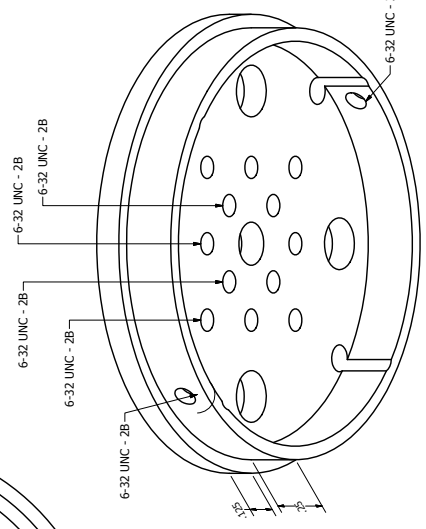
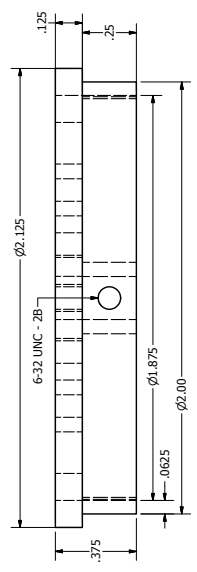
DESIGN	DATE	TITLE	SIZE	DWG NO	REV
MADE	7/4/2014		C	GasG10BaffleUpdated	
CHECKED			SCALE		SHEET 1 OF 1
QA					
PHG					
APPROVED					

Top View Bottom View

Material: Copper
Quantity: 1



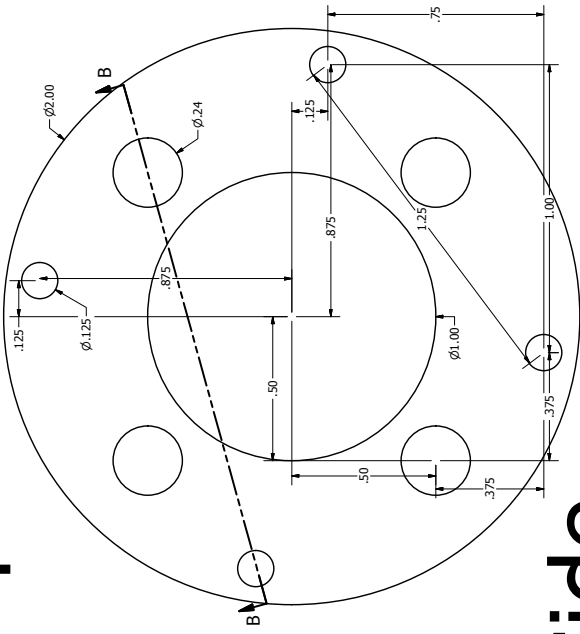
Side View



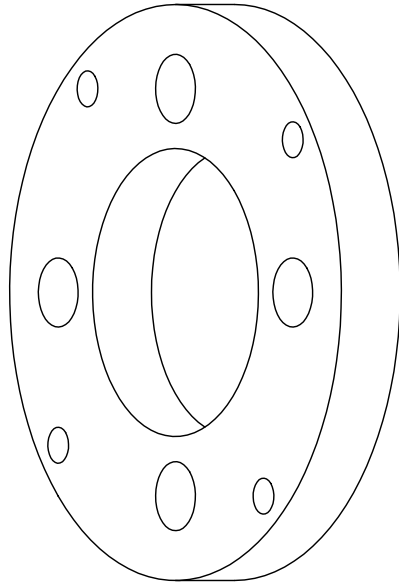
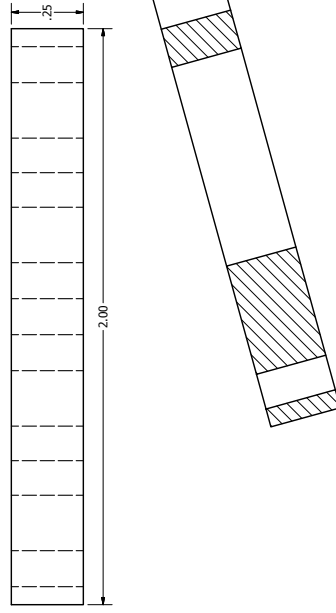
DESIGN	7/4/2014	TITLE	
ISSUED			
CHECKED	QA		
APPROVED	PHG		
		SIZE	C
		SCALE	
		DWG NO	ProbeHeadTop
		REV	

Material: G10 fiberglass or similar
 Quantity: 1

Top

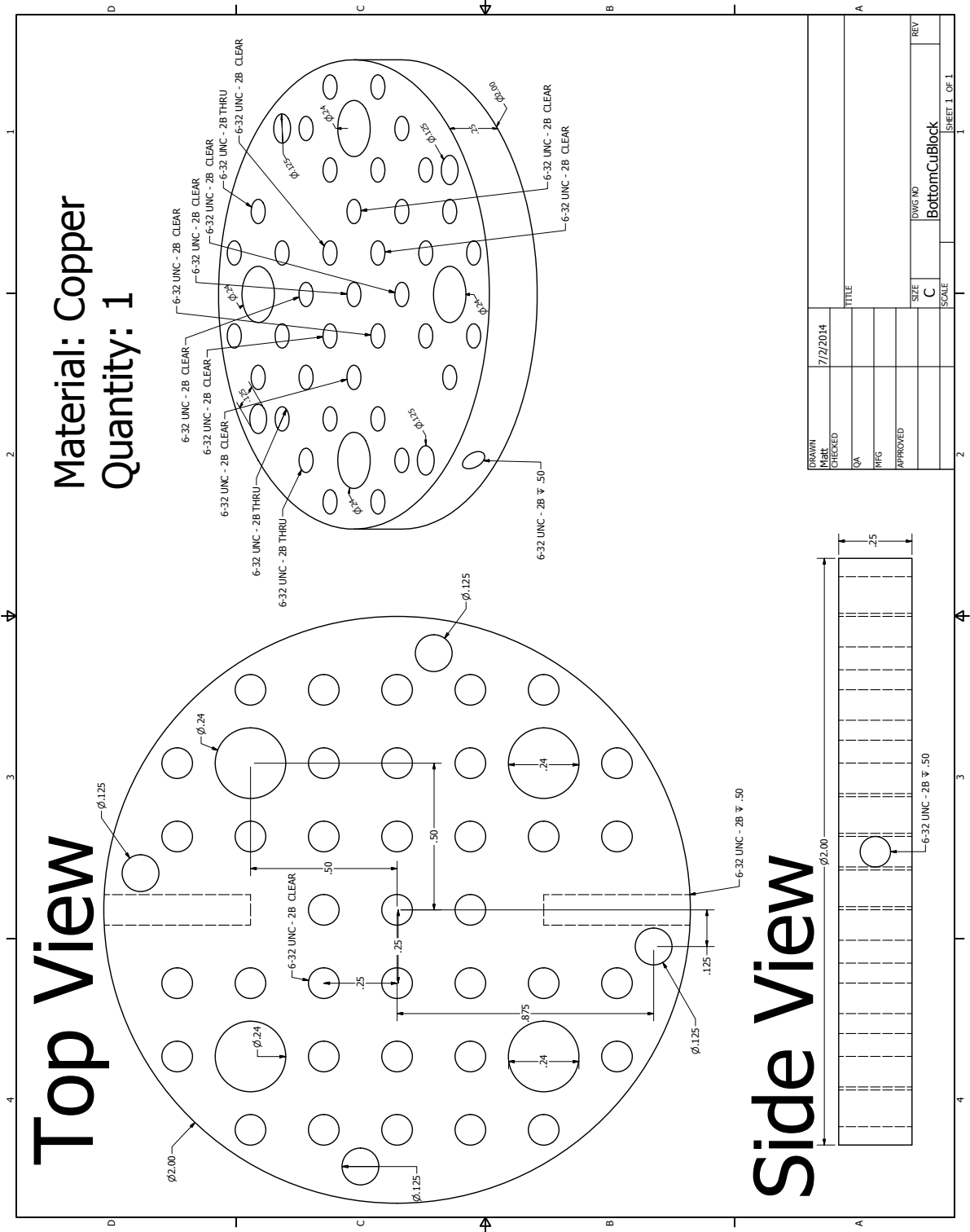


Side

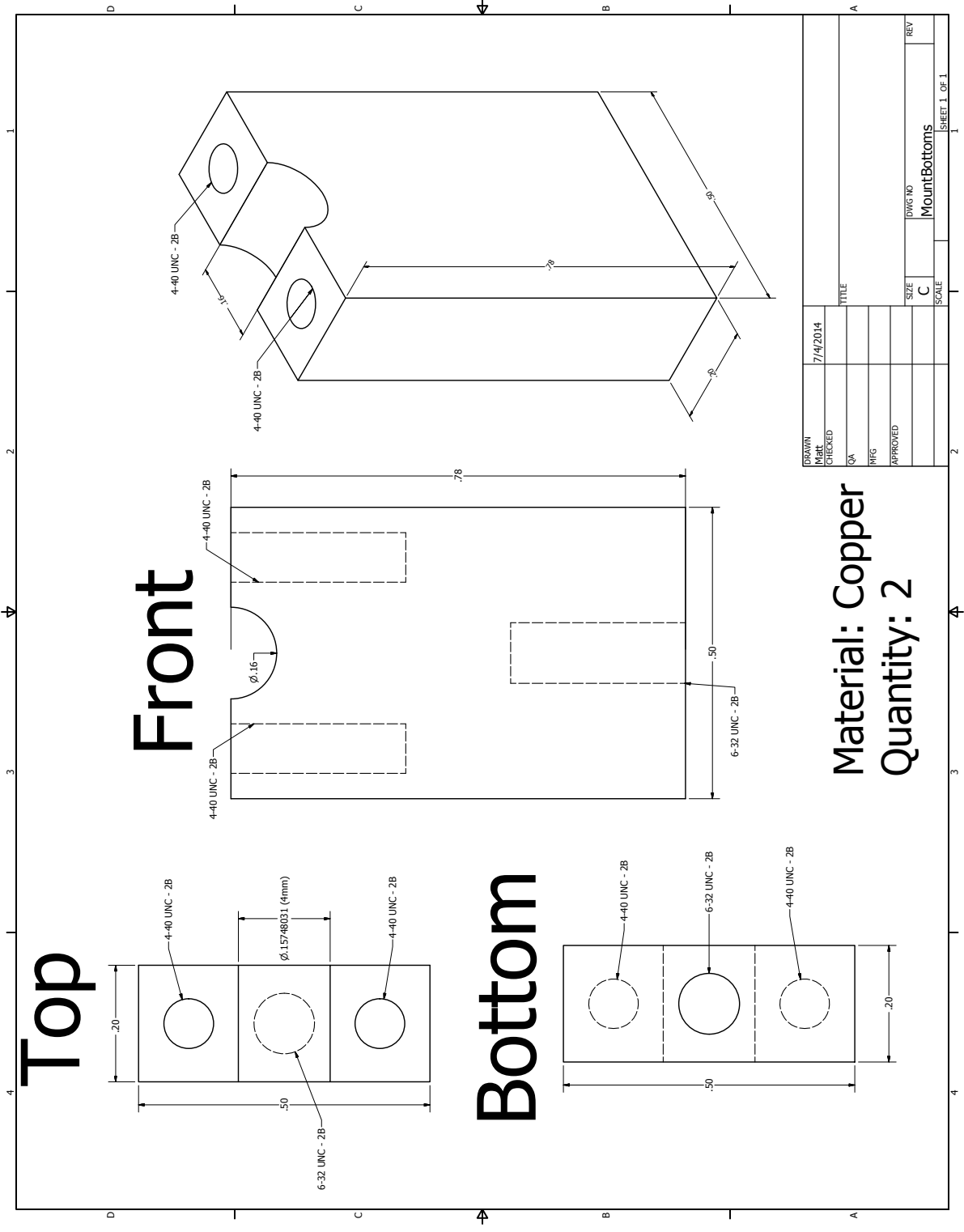


DESIGN	7/4/2014	TITLE	
ISSUED		SIZE	C
CHECKED		SCALE	
QA		DWG NO	G10ProbeHead
APPROVED		REV	
			SHEET 1 OF 1

Top View



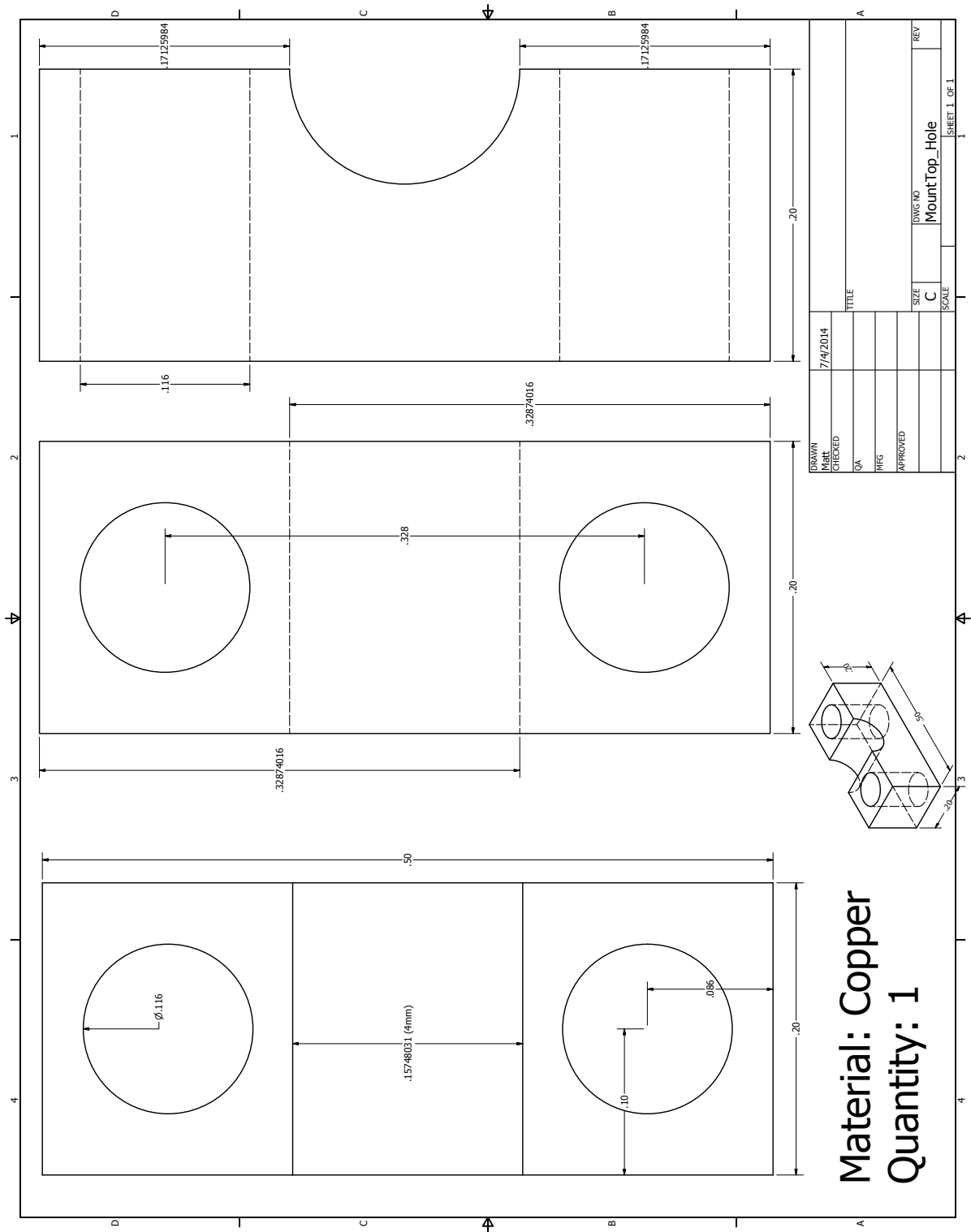
DESIGN	7/2/2014	TITLE	
ISSUED		SIZE	C
CHECKED		SCALE	
QA		DWG NO	BottomCuBlock
PHG		REV	
APPROVED			
			SHEET 1 OF 1

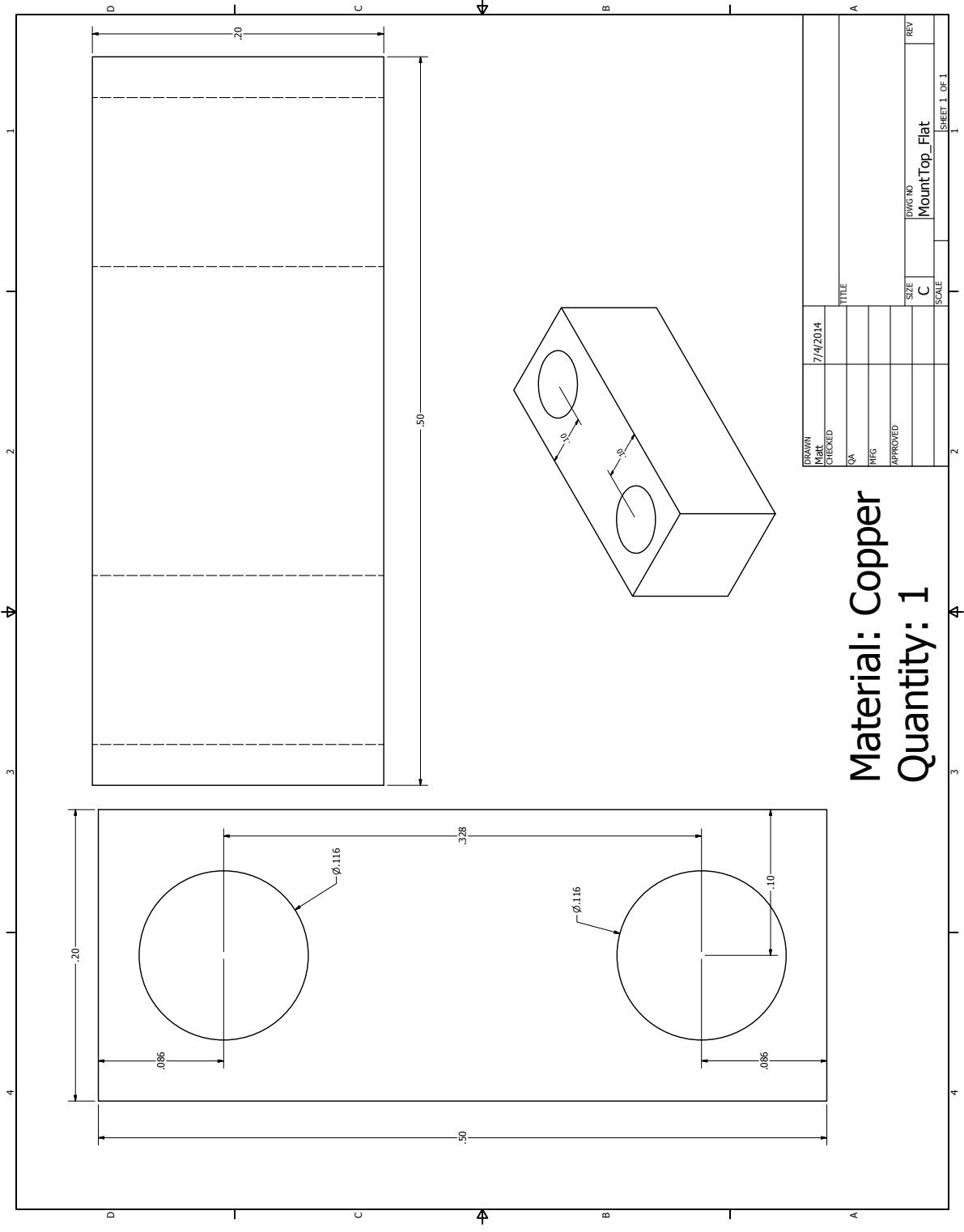


DESIGN	7/14/2014	TITLE	
ISSUED		QA	
CHECKED		PHG	
APPROVED		SCALE	
		SIZE	C
		DWG NO	MountBottoms
		REV	

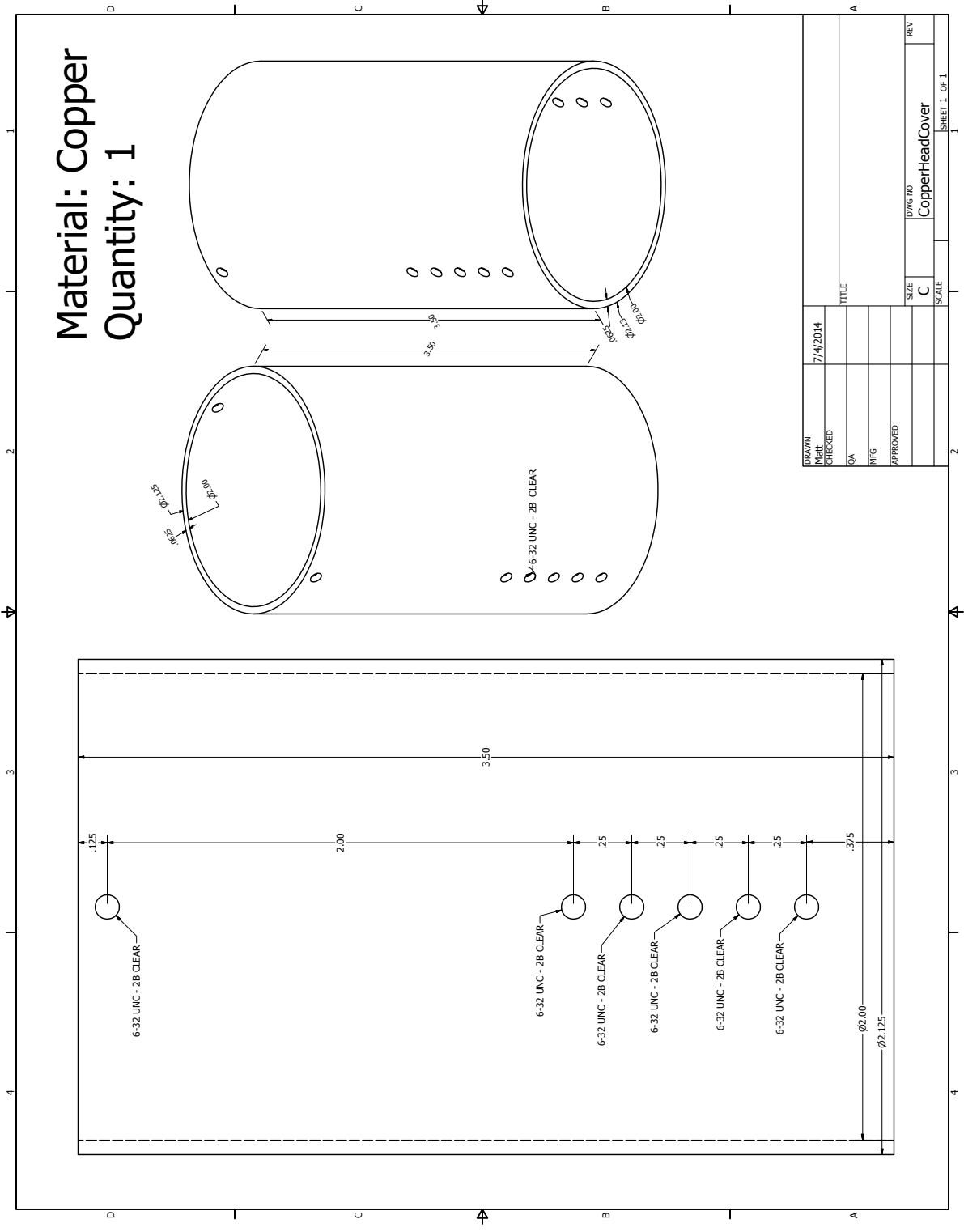
Material: Copper
Quantity: 2

1 2 3 4 1 2 3 4 1 2 3 4





Material: Copper
Quantity: 1



References

- [1] I Rabi, J. Zacharias, S. Millman, and P. Kusch. A New Method of Measuring Nuclear magnetic Moment. *Physical Review*, 53(February):318, 1938.
- [2] Charles P. Slichter. *Principles of magnetic resonance*. Springer-Verlag, third edition, 1990.
- [3] James Keeler. *Understanding NMR Spectroscopy*. John Wiley & Sons, Ltd, West Sussex, second edition, 2012.
- [4] Robert Tycko and Jeffrey A. Reimer. Optical Pumping in Solid State Nuclear Magnetic Resonance. *J. Phys. Chem.*, 3654(95):13240–13250, 1996.
- [5] M.I. Dyakonov and V.I. Perel. *Theory of Optical Spin Orientation of Electrons and Nuclei in Semiconductors*, volume 8. North-Holland Physics Publishing, 1984.
- [6] P. L. Kuhns, A. Kleinhammes, T. Schmiedel, W. G. Moulton, P. Chabrier, S. Sloan, E. Hughes, and C. Russell Bowers. Magnetic-Field Dependence of the Optical Overhauser Effect in GaAs. *Physical Review B*, 55(12):7824–7830, mar 1997.
- [7] C. Russell Bowers. Microscopic Interpretation of Optically Pumped NMR Signals in GaAs. *Solid state nuclear magnetic resonance*, 11(1-2):11–20, mar 1998.
- [8] Robert Tycko. Optical Pumping in Indium Phosphide: ^{31}P NMR Measurements and Potential for Signal Enhancement in Biological Solid State NMR. *Solid state nuclear magnetic resonance*, 11(1-2):1–9, mar 1998.
- [9] Carl A Michal and Robert Tycko. Stray-field NMR imaging and wavelength dependence of optically pumped nuclear spin polarization in InP. *Physical Review B (Condensed Matter and Materials Physics)*, 60(12):8672, 1999.
- [10] Tanja Pietrass and Marco Tomaselli. Optically Pumped NMR in CdS Single Crystals. *Physical Review B*, 59(3):1986–1989, jan 1999.
- [11] Robert Tycko and SE Barrett. Optically Pumped NMR of Semiconductors and Two Dimensional Electron Systems. *eMagRes*, 1:711–719, 2001.
- [12] Sophia E. Hayes, Stacy Mui, and Kannan Ramaswamy. Optically Pumped Nuclear Magnetic Resonance of Semiconductors. *The Journal of Chemical Physics*, 128(5):052203, mar 2008.

- [13] Wei Dong, Bo Li, Qiang Zhang, Maria Tamargo, and Carlos Meriles. Helicity-independent optical pumping of nuclear magnetization in bulk CdTe. *Physical Review B*, 80(4):045211, jul 2009.
- [14] K. Ramaswamy, S. Mui, S. a. Crooker, X. Pan, G. D. Sanders, C. J. Stanton, and S. E. Hayes. Optically pumped NMR: Revealing spin-dependent Landau level transitions in GaAs. *Physical Review B - Condensed Matter and Materials Physics*, 82(8):1–5, 2010.
- [15] Yunpu Li, Jonathan P. King, Le Peng, Maria C. Tamargo, Jeffrey A. Reimer, and Carlos a. Meriles. Helicity independent optically-pumped nuclear magnetic resonance in gallium arsenide. *Applied Physics Letters*, 98(11):1–4, 2011.
- [16] M N Makhonin, K V Kavokin, P Senellart, a Lemaître, a J Ramsay, M S Skolnick, and a I Tartakovskii. Fast control of nuclear spin polarization in an optically pumped single quantum dot. *Nature materials*, 10(11):844–8, nov 2011.
- [17] R. M. Wood, D. Saha, L. a. McCarthy, J. T. Tokarski, G. D. Sanders, P. L. Kuhns, S. a. McGill, a. P. Reyes, J. L. Reno, C. J. Stanton, and C. R. Bowers. Effects of strain and quantum confinement in optically pumped nuclear magnetic resonance in GaAs: Interpretation guided by spin-dependent band structure calculations. *Physical Review B*, 90(15):155317, 2014.
- [18] Erika L Sesti, Wieland Worthoff, Dustin D Wheeler, Dieter Suter, and Sophia Eugenie Hayes. Magnetic Field Dependence of the Light Hole-to-Conduction Band Transition in GaAs/AlGaAs Quantum Wells from Optically-Pumped NMR and Hanle Curve Measurements Article. *Journal of Magnetic Resonance*, 246:130–135, 2014.
- [19] Daniel Henriksen, Tom Kim, and Ionel ifrea. Nuclear spin diffusion effects in optically pumped quantum wells. *The European Physical Journal B*, 87(1):17, jan 2014.
- [20] J. B. Miller, C. A. Klug, K. L. Sauer, and J. P. Yesinowski. Temporal and spatial evolution of nuclear polarization in optically pumped InP. *Physical Review B*, 91(24):245205, 2015.
- [21] Dongyoung Yoon, Murari Soundararajan, and Jean-Philippe Ansermet. Nuclear polarization by optical pumping in InP:Fe above liquid nitrogen temperature. *Solid State Nuclear Magnetic Resonance*, 70:48–52, 2015.
- [22] Dustin D. Wheeler, Matthew M. Willmering, Erika L. Sesti, Xingyuan Pan, Dipta Saha, Christopher J. Stanton, and Sophia E. Hayes. Modelling of OPNMR phenomena using photon energy-dependent $\langle Sz \rangle$ in GaAs and InP. *Journal of Magnetic Resonance*, 273:19–26, 2016.
- [23] K.T. Mueller. Analytic Solutions for the Time Evolution of Dipolar-Dephasing NMR Signals, 1995.

- [24] Juha Vaara, Jukka Jokisaari, Roderick E. Wasylshen, and David L. Bryce. Spin-spin coupling tensors as determined by experiment and computational chemistry. *Progress in Nuclear Magnetic Resonance Spectroscopy*, 41(3-4):233–304, 2002.
- [25] A. Nolle. Direct and Indirect Dipole-Dipole Coupling Between ^{111}Cd , ^{113}Cd , and ^{125}Te in Solid CdTe. *Zeitschrift fur Physik B*, 34(2):175–182, 1979.
- [26] Pascal P Man. Quadrupole Couplings in Nuclear Magnetic Resonance, General. *Encyclopedia of Analytical Chemistry*, pages 12224–12265, 2000.
- [27] Chenming Calvin Hu. Electrons and holes in semiconductors. In *Modern Semiconductor Devices for Integrated Circuits*, chapter 1. Prentice Hall, 2009.
- [28] L.C. Lew Yan Voon and M Willatzen. *The k.p Method: Electronic Properties of Semiconductors*. Springer, 2009.
- [29] I Hernandez-Calderon. Optical properties and electronic structure of wide band gap II-VI semiconductors. In Maria C. Tamargo, editor, *II VI Semiconductor Materials and Their Applications*, chapter 4, pages 113–170. Taylor and Francis, New York, 2002.
- [30] Claudine Hermann and Claude Weisbuch. k*p perturbation theory in II-V compounds and alloys: a reexamination. *Physical Review B*, 15(2):823–833, 1977.
- [31] R Planel. Spin orientation by optical pumping in semiconductors. *Solid-State Electronics*, 21:1437–1444, 1978.
- [32] Georges Lampel. Nuclear Dynamic Polarization By Optical Electronic Saturation and Optical Pumping in Semiconductors. *Physical Review Letters*, 20(10):491–493, 1968.
- [33] N. T. Bagraev and L. S. Vlasenko. Optical Nuclear Polarization in Heavy-Doped Silicon. *Solid State Communications*, 40(4):483–485, 1981.
- [34] Maurice Goldman. Low Spin Temperature NMR. *Encyclopedia of NMR*, 5:2437–2446, 2012.
- [35] Anant Paravastu and Jeffrey Reimer. Nuclear spin temperature and magnetization transport in laser-enhanced NMR of bulk GaAs. *Physical Review B*, 71(4):045215, 2005.
- [36] Claude Weisbuch and Claudine Hermann. Optical Detection of Conduction-Electron Spin Resonance in GaAs, Ga $_{1-x}$ In $_x$ As, and Ga $_{1-x}$ Al $_x$ As. *Physical Review B*, 15(2):816–822, 1977.
- [37] E L Sesti, D Saha, D D Wheeler, G D Sanders, S E Hayes, and C J Stanton. Assignments of Transitions in the OPNMR of GaAs / AlGaAs Quantum Wells on a Bulk GaAs Substrate. *Physical Review B*, 90:125301, 2014.

- [38] Anant Paravastu, Sophia Hayes, Birgit Schwickert, Long Dinh, Mehdi Balooch, and Jeffrey Reimer. Optical polarization of nuclear spins in GaAs. *Physical Review B*, 69(7):075203, feb 2004.
- [39] Isaac J. H. Leung and Carl A. Michal. Optical Enhancement of NMR Signals in CdTe. *Physical Review B*, 035213(70):1–6, 2004.
- [40] Dustin D. Wheeler and Mark S. Conradi. Practical exercises for learning to construct NMR/MRI probe circuits. *Concepts in Magnetic Resonance Part A*, 40A(1):1–13, jan 2012.
- [41] J. Haase, N. J. Curro, and C. P. Slichter. Double resonance probes for close frequencies. *Journal of magnetic resonance*, 135(2):273–279, 1998.
- [42] Atsushi Goto, Shinobu Ohki, Kenjiro Hashi, and Tadashi Shimizu. Optical-pumping double-resonance NMR system for semiconductors. *Review of Scientific Instruments*, 77(9):093904, 2006.
- [43] M. H. Levitt, D. Suter, and R. R. Ernst. Spin dynamics and thermodynamics in solid-state NMR cross polarization. *The Journal of Chemical Physics*, 84(8):4243, 1986.
- [44] E. O. Stejskal and Jacob Schaefer. Removal of artifacts from cross-polarization NMR experiments. *Journal of Magnetic Resonance*, 18(3):560–563, 1975.
- [45] M. Kubisa, L. Bryja, K. Ryczko, J. Misiewicz, C. Bardot, M. Potemski, G. Ortner, M. Bayer, a. Forchel, and C. Sørensen. Photoluminescence investigations of two-dimensional hole Landau levels in p-type single Al_xGa_{1-x}As/GaAs heterostructures. *Physical Review B*, 67(3):035305, jan 2003.
- [46] Da Broido and Lj Sham. Effective masses of holes at GaAs-AlGaAs heterojunctions. *Physical Review B*, 31(2):888–892, may 1985.
- [47] Eric S.-R. Yang, D. A. Broido, and L. J. Sham. Holes at GaAs-Al_xGa_{1-x}As heterojunctions in magnetic fields. *Physical Review B*, 32(10):6630–6633, nov 1985.
- [48] K. Ryczko, M. Kubisa, L. Bryja, J. Misiewicz, R. Stpniewski, M. Byszewski, and M. Potemski. Hole subbands and Landau levels in p-type single Al_xGa_{1-x}As/GaAs heterostructures. *Physica B: Condensed Matter*, 346-347:451–454, apr 2004.
- [49] F. Ancilotto, a. Fasolino, and J.C. Maan. Effect of band mixing of the hole subbands in quantum wells on the optical transition intensities in a magnetic field. *Superlattices and Microstructures*, 3(2):187–191, 1987.
- [50] Yunpu Li, Jonathan P. King, Jeffrey A. Reimer, and Carlos A. Meriles. Near-band-gap photoinduced nuclear spin dynamics in semi-insulating GaAs: Hyperfine- and quadrupolar-driven relaxation. *Physical Review B*, 88(23):235211, dec 2013.

- [51] Stacy Mui, Kannan Ramaswamy, and Sophia E. Hayes. Effects of optical absorption on Ga71 optically polarized NMR in semi-insulating GaAs: Measurements and simulations. *Physical Review B - Condensed Matter and Materials Physics*, 75(19):1–8, 2007.
- [52] Jonathan P King, Yunpu Li, Carlos A Meriles, and Jeffrey A Reimer. Optically rewritable patterns of nuclear magnetization in gallium arsenide. *Nature communications*, 3(May):918, jan 2012.
- [53] Anil Patel, Olivier Pasquet, Jagadeesh Bharatam, E. Hughes, and C. Russell Bowers. Optical Dynamic Nuclear Polarization in InP single crystal: Wavelength and Field Dependence of NMR Enhancement. *Physical Review B*, 60(8):5105–5108, 1999.
- [54] Atsushi Goto, Kenjiro Hashi, Tadashi Shimizu, and Shinobu Ohki. Dynamics of electron-nuclear and heteronuclear polarization transfers in optically oriented semi-insulating InP:Fe. *Physical Review B*, 77(11):115203, mar 2008.
- [55] P. Horodyský and P. Hlídek. Free-exciton absorption in bulk CdTe: temperature dependence. *Physica Status Solidi (B)*, 243(2):494–501, feb 2006.
- [56] Cheryl Barnett Davis, David D. Allred, A. Reyes-Mena, J. Gonzalez-Hernandez, Ovidio Gonzalez, Bret C. Hess, and Worth P. Allred. Photoluminescence and absorption studies of defects in CdTe and $Zn_xCd_{1-x}Te$ Crystals. *Physical Review B*, 47(20):13363–13369, 1993.
- [57] A Nakamura, Daniel Paget, Claudine Hermann, Claude Weisbuch, and Georges Lampel. Optical Detection of Electron Spin Resonance in CdTe. *Solid State Communications*, 30, 1979.
- [58] N. C. Giles-Taylor, R. N. Bicknell, D. K. Blanks, T. H. Myers, and J. F. Schetzina. Photoluminescence of CdTe: A comparison of bulk and epitaxial material. *Journal of Vacuum . . .*, 3(1):76–82, 1985.
- [59] Jaesun Lee, N. C. Giles, D. Rajavel, and C. J. Summers. Room-temperature band-edge photoluminescence from cadmium telluride. *Physical Review B*, 49(3):1668–1676, 1994.
- [60] D P Halliday, M D G Potter, J T Mullins, and A W Brinkman. Photoluminescence study of a bulk vapour grown CdTe crystal. *Journal of Crystal Growth*, 220(February):30–38, 2000.
- [61] E. F. Thenell, M. E. Limes, E. G. Sorte, Z. V. Vardeny, and B. Saam. Nuclear relaxation measurements in organic semiconducting polymers for application to organic spintronics. *Physical Review B*, 91(4):1–8, 2015.

- [62] M Mehring. Decoherence and entanglement of quantum states. In *Quantum Coherence in Solid State Systems*, pages 131–150. IOS Press, 2009.
- [63] M Mehring, J Mende, and W Scherer. Entanglement between an electron and a nuclear spin 1/2. *Physical review letters*, 90(15):153001, 2003.
- [64] J. S. Colton, T. A. Kennedy, A. S. Bracker, J. B. Miller, and D. Gammon. Dependence of Optically Oriented and Detected Electron Spin Resonance on Donor Concentration in n-GaAs. *Solid State Communications*, 132(9):613–616, dec 2004.
- [65] L M Vandersypen, Matthias Steffen, Gregory Breyta, C S Yannoni, M H Sherwood, and I L Chuang. Experimental realization of Shor’s quantum factoring algorithm using nuclear magnetic resonance. *Nature*, 414(6866):883–7, 2001.
- [66] G. B. Furman, V. M. Meerovich, and V. L. Sokolovsky. Entanglement of dipolar coupling spins. *Quantum Information Processing*, 10(3):307–315, 2011.
- [67] Gregory B. Furman, Victor M. Meerovich, and Vladimir L. Sokolovsky. Entanglement under equilibrium establishing in spin systems subjected to radiofrequency field. *Quantum Information Processing*, 13(2):309–321, 2014.
- [68] Atsushi Goto, Shinobu Ohki, Kenjiro Hashi, and Tadashi Shimizu. Optical switching of nuclear spin-spin couplings in semiconductors. *Nature communications*, 2(7):378, jan 2011.
- [69] Anatole Abragam. *The Principles of Nuclear Magnetism*. Oxford, 1985.
- [70] E. L. Hahn and D. E. Maxwell. Spin Echo measurements of Nuclear Spin Coupling in Molecules. *Physical Review*, 88(5):1070–1084, 1952.
- [71] A. Pines, M. G. Gibby, and J. S. Waugh. Proton-enhanced nmr of dilute spins in solids. *The Journal of Chemical Physics*, 59(2):569–590, 1973.
- [72] S. Hartmann and E. Hahn. Nuclear Double Resonance in the Rotating Frame. *Physical Review*, 128(5):2042–2053, dec 1962.
- [73] M. Mehring. *High Resolution NMR Spectroscopy in Solids*. Springer-Verlag, 1976.
- [74] D. A. McArthur, E. L. Hahn, and R. E. Walstedt. Rotating-frame nuclear-double-resonance dynamics: Dipolar fluctuation spectrum in CaF_2 . *Phys. Rev.*, 188:609–638, Dec 1969.
- [75] Geoffrey E. Hawkes, Michael D. Mantle, Kieth D. Sales, Silvio Aime, Robert Gobetto, and Christopher J. Groombridge. Dipolar oscillations in the $^{13}\text{C}^{1}\text{H}$ cross-polarization/magic-angle-spinning spectrum of $\text{H}_2\text{O}_3(\text{CO})_{10}$. *Journal of Magnetic Resonance, Series A*, 116(2):251 – 254, 1995.

- [76] Alexander a. Nevzorov. Ergodicity and efficiency of cross-polarization in NMR of static solids. *Journal of Magnetic Resonance*, 209(2):161–166, 2011.
- [77] Peng Li, Qun Chen, and Shanmin Zhang. Analytical solution of cross polarization dynamics. *Journal of Magnetic Resonance*, 250(0):76 – 79, 2015.
- [78] T Shimizu, A Goto, K Hashi, and S Ohki. An {NMR} quantum computer of the semiconductor cdte. *Superlattices and Microstructures*, 32(46):313 – 316, 2002. Papers from the 8th International Symposium of Advanced Physical Fields on Advanced Materials for Quantum Computing.
- [79] Ken Sakaie, C.P. Slichter, and J.H. Sinfelt. Methods Using the Nuclear Quadrupole Interaction to Determine the Structure of Randomly Oriented Molecules. *Journal of Magnetic Resonance, Series A*, 119(2):235–239, 1996.
- [80] Terry Gullion, David B Baker, and Mark S. Conradi. New, Compensated Carr-Purcell. *Journal of Magnetic Resonance*, 89:479–484, 1990.
- [81] Marco Tomaselli, David DeGraw, Jeffery Yarger, Matthew Augustine, and Alexander Pines. Scalar and anisotropic J interactions in undoped InP: A triple-resonance NMR study. *Physical Review B*, 58(13):8627–8633, oct 1998.
- [82] D.E. Kaplan and E.L. Hahn. Expériences de double irradiation en résonance magnétique par la méthode d’impulsions. *J. Phys. Radium*, 19, 1958.
- [83] Yu V Piskunov, V V Ogloblichev, and S V Verkhovsky. Inhomogeneous State of the Electron System in the Sr(14-x)Ca(x)Cu(24)O(41) Superconducting Cuprate : ⁶³Cu 17O NMR Study. *JETP Letters*, 86(11):740–744, 2007.
- [84] Matthew M. Willmering, Zayd L. Ma, Melanie A. Jenkins, John F. Conley, and Sophia E. Hayes. Enhanced nmr with optical pumping yields 75as signals selectively from a buried gas interface. *Journal of the American Chemical Society*, 139(11):3930–3933, 2017. PMID: 28256125.
- [85] Alfonso Franciosi and Chris G Van de Walle. Heterojunction band offset engineering. *Surface Science Reports*, 25:1–140, 1996.
- [86] M. L. Huang, Y. C. Chang, C. H. Chang, Y. J. Lee, P. Chang, J. Kwo, T. B. Wu, and M. Hong. Surface passivation of III-V compound semiconductors using atomic-layer-deposition-grown Al₂O₃. *Applied Physics Letters*, 87(25):1–3, 2005.
- [87] G.K. Dalapati. Electrical and Interfacial Characterization of Atomic Layer Deposited High- κ Gate Dielectrics on GaAs for Advanced CMOS Devices. *IEEE Transactions on Electron Devices*, 54(8):1831–1837, 2007.

- [88] C. L. Hinkle, A. M. Sonnet, E. M. Vogel, S. McDonnell, G. J. Hughes, M. Milojevic, B. Lee, F. S. Aguirre-Tostado, K. J. Choi, H. C. Kim, J. Kim, and R. M. Wallace. GaAs interfacial self-cleaning by atomic layer deposition. *Applied Physics Letters*, 92(7):071901, 2008.
- [89] Hang Dong Lee, Tian Feng, Lei Yu, Daniel Mastrogiovanni, Alan Wan, Torgny Gustafsson, and Eric Garfunkel. Reduction of native oxides on GaAs during atomic layer growth of Al₂O₃. *Applied Physics Letters*, 94(22):10–13, 2009.
- [90] J. P. Yesinowski. Solid-state NMR of inorganic semiconductors. *Topics in Current Chemistry*, 306:229–312, 2012.
- [91] L Goehring and C A Michal. Nuclear spin polarization transfer across an organic-semiconductor interface. *The Journal of chemical physics*, 119(19):10325, 2003.
- [92] M Goswami, P J Knijn, G J Bauhuis, J W G Janssen, P J M Van Bentum, G A De Wijs, and A P M Kentgens. Stripline ⁷⁵As NMR Study of Epitaxial III–V Semiconductor. *J. Phys. Chem. C*, 118:13394–13405, 2014.
- [93] Dieter Freude. Quadrupolar Nuclei in Solid-state Nuclear Magnetic Resonance. *Encyclopedia of Analytical Chemistry*, pages 12188–12224, 2000.
- [94] Sharon E. Ashbrook. Recent advances in solid-state NMR spectroscopy of quadrupolar nuclei. *Physical Chemistry Chemical Physics*, 11(32):6892–6905, 2009.
- [95] D. J. Guerrier and R. T. Harley. Calibration of strain vs nuclear quadrupole splitting in III-V quantum wells. *Applied Physics Letters*, 70(13):1739, 1997.
- [96] J. W. Zwanziger, U. Werner-Zwanziger, J. L. Shaw, and C. So. Stress, strain, and NMR. *Solid State Nuclear Magnetic Resonance*, 29(1-3):113–118, 2006.
- [97] Marcus Eickhoff, Björn Lenzman, Dieter Suter, Sophia E. Hayes, and Andreas D. Wieck. Mapping of strain and electric fields in GaAs/AlGaAs quantum-well samples by laser-assisted NMR. *Physical Review B*, 67(16):085308, 2003.
- [98] Flemming H. Larsen, Hans J. Jakobsen, Paul D. Ellis, and Niels Chr. Nielsen. Sensitivity-Enhanced Quadrupolar-Echo NMR of Half-Integer Quadrupolar Nuclei. Magnitudes and Relative Orientation of Chemical Shielding and Quadrupolar Coupling Tensors. *The Journal of Physical Chemistry A*, 101(46):8597–8606, 1997.
- [99] Maki Suemitsu and Naoki Nakajo. Charged point defects in GaAs crystals evaluated by nuclear-magnetic-resonance spin echo. *Journal of Applied Physics*, 66(7):3178–3186, 1989.

- [100] Maki Suemitsu, Masaaki Nishijima, and Nobuo Miyamoto. Carbon concentration dependence of charged point-defect density in semi-insulating GaAs as observed by nuclear magnetic resonance. *Applied Physics Letters*, 57(4):398, 1990.
- [101] J. Butterworth. Spin echoes in solids. *Proceedings of the Physical Society*, 86(2):297, 1965.
- [102] P. D. Ye, G. D. Wilk, J. Kwo, B. Yang, H. J L Gossmann, M. Frei, S. N G Chu, J. P. Mannaerts, M. Sergent, M. Hong, K. K. Ng, and J. Bude. GaAs MOSFET with oxide gate dielectric grown by atomic layer deposition. *IEEE Electron Device Letters*, 24(4):209–211, 2003.
- [103] D. V. Vasilenko, N. V. Luk’yanova, and R. P. Seisyan. Fano effect in the magnetoabsorption spectra of gallium arsenide. *Semiconductors*, 33(1):15–19, 1999.
- [104] Jingyun Huang, Zhizhen Ye, Huanming Lu, and Duanlin Que. Calculation of critical layer thickness considering thermal strain in Si(1-x)Ge(x)/Si strained-layer heterostructures. *Journal of Applied Physics*, 83(1):171–173, 1997.
- [105] Deepayan Chakraborti. *Novel Diluted Magnetic Semiconductor Materials based on Zinc Oxide*. PhD thesis, North Carolina State University, Raleigh, North Carolina, 2007.
- [106] Theeradetch Detchprohm, Kazumasa Hiramatsu, Kenji Itoh, and Isamu Akasaki. Relaxation Process of the Thermal Strain in the GaN α -Al₂O₃ Heterostructure and Determination of the Intrinsic Lattice Constants of GaN Free from the Strain. *Jpn. J. Appl. Phys.*, 31(10):1454–1456, 1992.
- [107] Ju Li, Krystyn J Van Vliet, Ting Zhu, Sidney Yip, and Subra Suresh. Atomistic mechanisms governing elastic limit and incipient plasticity in crystals. *Letters to Nature*, 418, 2002.
- [108] H. T. Johnson and L. B. Freund. Mechanics of coherent and dislocated island morphologies in strained epitaxial material systems. *Journal of Applied Physics*, 81(9):6081–6090, 1997.
- [109] Pascal P. Man, Jacek Klinowski, Arlette Trokiner, Hélène Zanni, and Pierre Papon. Selective and non-selective NMR excitation of quadrupolar nuclei in the solid state. *Chemical Physics Letters*, 151(1-2):143–150, 1988.
- [110] W. de Boer, M. Borghini, K. Morimoto, T. O. Niinikoski, and F. Udo. Dynamic polarization of protons, deuterons, and carbon-13 nuclei: Thermal contact between nuclear spins and an electron spin-spin interaction reservoir. *Journal of Low Temperature Physics*, 15(3-4):249–267, 1974.

- [111] Otfried Madelung. *Semiconductors - Basic Data*. Springer-Verlag, Berlin, 2nd revised edition, 1996.
- [112] Jeffrey A. Reimer. Nuclear hyperpolarization in solids and the prospects for nuclear spintronics. *Solid state nuclear magnetic resonance*, 37(1-2):3–12, 2010.
- [113] E. Burstein, G. S. Picus, R. F. Wallis, and F. Blatt. Zeeman-type magneto-optical studies of interband transitions in semiconductors. *Physical Review*, 113(1):15–33, 1959.
- [114] Igor Levin and David Brandon. Metastable Alumina Polymorphs: Crystal Structures and Transition Sequences. *Journal of the American Ceramic Society*, 81(8):1995–2012, 2005.
- [115] P. E. Doherty and R. S. Davis. Direct observation of the oxidation of aluminum single-crystal surfaces. *Journal of Applied Physics*, 34(3):619–628, 1963.
- [116] H. G. F. Wilsdorf. Structure of amorphous aluminum oxide films. *Nature*, 168:600–601, 1951.
- [117] E. A. Gulbransen and W. S. Wysong. Thin Oxide Films on Aluminum. *J. Phys. Chem.*, 51:1087–1103, 1947.
- [118] B.G Segda, M Jacquet, and J.P Besse. Elaboration, characterization and dielectric properties study of amorphous alumina thin films deposited by r.f. magnetron sputtering. *Vacuum*, 62(1):27–38, 2001.
- [119] Diane Samélor, Ana-Maria Lazar, Maëlen Aufray, Claire Tendero, Loïc Lacroix, Jean-Denis Béguin, Brigitte Caussat, Hugues Vergnes, Joël Alexis, Dominique Poquillon, Nadine Pébère, Alain Gleizes, and Constantin Vahlas. Amorphous alumina coatings: processing, structure and remarkable barrier properties. *Journal of nanoscience and nanotechnology*, 11(xx):8387–91, 2011.
- [120] P. Lamparter and R. Kniep. Structure of amorphous Al₂O₃. *Physica B: Condensed Matter*, 234-236:405–406, 1997.
- [121] Sung Keun Lee, Sung Bo Lee, Sun Young Park, Yoo Soo Yi, and Chi Won Ahn. Structure of amorphous aluminum oxide. *Physical Review Letters*, 103(9):4–7, 2009.
- [122] Sung Keun Lee, Sun Young Park, Yoo Soo Yi, and Jaehyun Moon. Structure and disorder in amorphous alumina thin films: Insights from high-resolution solid-state NMR. *Journal of Physical Chemistry C*, 114(32):13890–13894, 2010.

- [123] Lawrie B. Skinner, Adrian C. Barnes, Philip S. Salmon, Louis Hennes, Henry E. Fischer, Chris J. Benmore, Shinji Kohara, J. K. Richard Weber, Aleksei Bytchkov, Martin C. Wilding, John B. Parise, Thomas O. Farmer, Irina Pozdnyakova, Sonia K. Tumber, and Koji Ohara. Joint diffraction and modeling approach to the structure of liquid alumina. *Physical Review B - Condensed Matter and Materials Physics*, 87(2):53–58, 2013.
- [124] G Kunath-Fandrei, TJ Bastow, J. S. Hall, C. Jager, and M. E. Smith. Quantification of aluminum coordinations in amorphous aluminas by combined central and satellite transition magic angle spinning NMR spectroscopy. *The Journal of Physical Chemistry*, 99:15138–15141, 1995.
- [125] R. Dupree, I. Farnan, A. J. Forty, S. El-mashri, and L. Bottyan. A MAS NMR study of the structure of amorphous alumina films. *J. Phys. Colloques*, 46:C8–113 – C8–117, 1985.
- [126] S. M. El-mashri, R. G. Jones, and A. J. Forty. An electron-yield EXAFS study of anodic-oxide and hydrated-oxide films on pure aluminium. *Philosophical Magazine A*, 48(5):665–683, 2006.
- [127] Priya Vashishta, Rajiv K. Kalia, Aiichiro Nakano, and José Pedro Rino. Interaction potentials for alumina and molecular dynamics simulations of amorphous and liquid alumina. *Journal of Applied Physics*, 103(8):083504, 2008.
- [128] Georg Kresse, Michael Schmid, Evelyn Napetschnig, Peter Varga, Maxim Shishkin, and Lukas Ko. Structure of the Ultrathin Aluminum Oxide Film on NiAl(110). *Science*, 308(June):1440–1442, 2005.
- [129] Vo Van Hoang. Molecular dynamics study on structure and properties of liquid and amorphous Al₂O₃. *Physical Review B*, 70(13):134204, 2004.
- [130] Raquel Lizárraga, Erik Holmström, Stephen C. Parker, and Corinne Arrouvel. Structural characterization of amorphous alumina and its polymorphs from first-principles XPS and NMR calculations. *Physical Review B*, 83(9):094201, 2011.
- [131] Hiroyoshi Momida, Tomoyuki Hamada, Yoshiteru Takagi, Takenori Yamamoto, Tsuyoshi Uda, and Takahisa Ohno. Theoretical study on dielectric response of amorphous alumina. *Physical Review B*, 73(5):054108, 2006.
- [132] Gonzalo Gutiérrez and Börje Johansson. Molecular dynamics study of structural properties of amorphous Al₂O₃. *Physical Review B*, 65:104202, 2002.
- [133] Sandro Jahn and Paul A. Madden. Structure and dynamics in liquid alumina: Simulations with an ab initio interaction potential. *Journal of Non-Crystalline Solids*, 353(32-40):3500–3504, 2007.

- [134] Sergio Davis and Gonzalo Gutiérrez. Structural, elastic, vibrational and electronic properties of amorphous Al₂O₃ from ab initio calculations. *Journal of Physics: Condensed Matter*, 23(49):495401, 2011.
- [135] L. A. O’Dell, S. L P Savin, A. V. Chadwick, and M. E. Smith. A ²⁷Al MAS NMR study of a sol-gel produced alumina: Identification of the NMR parameters of the θ -Al₂O₃ transition alumina phase. *Solid State Nuclear Magnetic Resonance*, 31(4):169–173, 2007.
- [136] Ary R. Ferreira, Emine Kucukbenli, Alexandre A. Leitao, and Stefano De Gironcoli. Ab initio ²⁷Al NMR chemical shifts and quadrupolar parameters for Al₂O₃ phases and their precursors. *Physical Review B - Condensed Matter and Materials Physics*, 84(23):1–10, 2011.
- [137] Jean Baptiste d’Espinose de Lacaillerie, Christian Fretigny, and Dominique Massiot. MAS NMR spectra of quadrupolar nuclei in disordered solids: The Czjzek model. *Journal of Magnetic Resonance*, 192(2):244–251, 2008.
- [138] Gérard Le Caër, Bruno Bureau, and Dominique Massiot. An extension of the Czjzek model for the distributions of electric field gradients in disordered solids and an application to NMR spectra of ⁷¹Ga in chalcogenide glasses. *Journal of physics. Condensed matter : an Institute of Physics journal*, 22(6):065402, 2010.
- [139] H. Martinez, R. Andrade, E. G. Birdgin, and J. M. Martinez. Packmol: A package for building initial configurations for molecular dynamics simulations. *Journal of Computational Chemistry*, 30:2157–2164, 2009.
- [140] G Kresse and J Hafner. Ab initio molecular-dynamics simulation of the liquid-metal-amorphous-semiconductor transition in germanium. *Phys. Rev. B*, 49:14251, 1994.
- [141] G Kresse and J Hafner. Ab initio molecular dynamics for liquid metals. *Phys. Rev. B*, 47:558, 1993.
- [142] J P Perdew, K Burke, and M Ernzerhof. Generalized gradient approximation made simple. *Physical review letters*, 77(18):3865–3868, oct 1996.
- [143] Thibault Charpentier. The PAW/GIPAW approach for computing NMR parameters: A new dimension added to NMR study of solids. *Solid State Nuclear Magnetic Resonance*, 40(1):1–20, 2011.
- [144] Dominique Massiot, Franck Fayon, Mickael Capron, Ian King, Stéphanie Le Calvé, Bruno Alonso, Jean Olivier Durand, Bruno Bujoli, Zhehong Gan, and Gina Hoatson. Modelling one- and two-dimensional solid-state NMR spectra. *Magnetic Resonance in Chemistry*, 40(1):70–76, 2002.

- [145] Blake A. Hammann. *Solid-state NMR of Molecular Clusters to Thin Films and NMR Crystallography*. PhD thesis, Washington University in St. Louis, 2016.
- [146] Matthew G. Kast, Elizabeth A. Cochran, Lisa J. Enman, Gavin Mitchson, Jeffrey Ditto, Chris Siefe, Paul N. Plassmeyer, Ann L Greenaway, David C. Johnson, Catherine J Page, and Shannon W. Boettcher. Amorphous mixed-metal oxide thin films from aqueous solution precursors with near atomic smoothness. *Journal of the American Chemical Society*, page jacs.6b11084, 2016.
- [147] C. Landron, L. Hennet, T. E. Jenkins, G. N. Greaves, J. P. Coutures, and A. K. Soper. Liquid alumina: Detailed atomic coordination determined from neutron diffraction data using empirical potential structure refinement. *Physical Review Letters*, 86(21):4839–4842, 2001.
- [148] Filipe Vasconcelos, Sylvain Cristol, Jean-François Paul, Laurent Delevoye, Francesco Mauri, Thibault Charpentier, and Gérard Le Caër. Extended Czjzek model applied to NMR parameter distributions in sodium metaphosphate glass. *Journal of physics. Condensed matter : an Institute of Physics journal*, 25(25):255402, 2013.
- [149] David L. Bryce and Elijah B. Bultz. Alkaline earth chloride hydrates: Chlorine quadrupolar and chemical shift tensors by solid-state NMR spectroscopy and plane wave pseudopotential calculations. *Chemistry - A European Journal*, 13(17):4786–4796, 2007.
- [150] John V. Hanna, Kevin J. Pike, Thibault Charpentier, Thomas F. Kemp, Mark E. Smith, Bryan E G Lucier, Robert W. Schurko, and Lindsay S. Cahill. A ^{93}Nb solid-state NMR and density functional theory study of four- and six-coordinate niobate systems. *Chemistry - A European Journal*, 16(10):3222–3239, 2010.

MATTHEW WILLMERING

5908 Wise Ave., St. Louis, MO 63110 | matt.willmering@gmail.com | (314)229-6806

EDUCATION | WASHINGTON UNIVERSITY IN ST. LOUIS, ST. LOUIS, MO 63130

PH.D. IN CHEMISTRY

August 2012 – April 2017 (Expected); GPA = 3.9/4.0

MISSOURI UNIVERSITY OF SCIENCE AND TECHNOLOGY, ROLLA, MO 65401

B.S. IN CHEMISTRY, ACS CERTIFIED

August 2008 – May 2012; GPA = 3.6/4.0

EXPERIENCE | RESEARCH ASSISTANT WASHINGTON UNIVERSITY IN ST. LOUIS

2012-PRESENT; DR. SOPHIA HAYES

- Designed and fabricated a 2-channel NMR *rf* probe for use at 5 K
- Measured the light-hole-to-conduction-band transition as a function of magnetic fields using optically pumped NMR
- Developed multiple pulse sequences combining 2-channel NMR techniques and optical pumping
- Examined the coupling strength and dephasing time of isolated nuclear spin pairs in CdTe semiconductor
- Determined the nuclear polarization at an Al₂O₃/GaAs interface and studied its dependencies

TEACHING ASSISTANT WASHINGTON UNIVERSITY IN ST. LOUIS

2012-2014; DR. MEGAN DASCHBACH

- Taught the review/recitation sections for both semesters of general chemistry
- Graded weekly quizzes and chaired exam grading sections

RESEARCH ASSISTANT MISSOURI UNIVERSITY OF SCIENCE AND TECHNOLOGY

2010-2012; DR. JAY SWITZER

- Explored different conditions to electro-chemically deposit metal oxide thin films
- Analyzed thin films with SEM, XRD, and through the use of a Physical Properties Measurement System

AWARDS | 2017 Washington University Dean's Dissertation Fellowship

2015 ENC Travel Stipend Award

2014 Washington University Chemistry Department Teaching Assistant Award

PUBLICATIONS | Evidence for Photon Energy Dependent $\langle Sz \rangle$ Under Optical Pumping of

Semiconductors, *Dustin D. Wheeler, Matthew M. Willmering, Erika L. Sesti, Xingyuan Pan, Dipta Saha, Christopher J. Stanton, and Sophia E. Hayes, Journal of Magnetic Resonance, 2016 273, 19-26*

Enhanced NMR with Optical Pumping Yields ⁷⁵As Signal Selectively from a Buried GaAs Interface, *Matthew M. Willmering, Zayd L. Ma, Melanie A. Jenkins, John F. Conley, and Sophia E. Hayes, Journal of the American Chemical Society, 2017 139 (11), 3930-3933*

A Combined Experimental Setup for OP and ODNMR, *Erika L. Sesti, Matthew M. Willmering, Zayd L. Ma, Dustin D. Wheeler, Mark S. Conradi, and Sophia E. Hayes, Under Review by Journal of Magnetic Resonance*

Observation of Nuclear Hyperpolarization at a Semiconductor Interface via OPNMR, *Matthew M. Willmering, Ike West, Zayd L. Ma, Parag Banerjee and Sophia E. Hayes*, To Be Submitted

Characterization of Isolated Nuclear Spin Pairs in CdTe Using Optical Pumping, *Zayd L. Ma, Matthew M. Willmering, and Sophia E. Hayes*, To Be Submitted

Probing the Magnetic Field Dependence of the Light Hole Transition in GaAs/AlGaAs Quantum Wells Using Optically Pumped NMR, *Matthew M. Willmering, Erika L. Sesti, Sophia E. Hayes, Ryan M. Wood, Clifford R. Bowers, Christopher J. Stanton, Arneil P. Reyes, Philip Kuhns, and Stephen McGill*, To Be Submitted

Local Atomic Structure and NMR Parameters in Amorphous Alumina, *Murat Aykol, Matthew M. Willmering, Kristin Persson, and Sophia E. Hayes*, To Be Submitted

Electrochemical Synthesis and Nonvolatile Resistance Switching of Mn₃O₄ Thin Films, *Jakub A. Koza, Ian P. Schroen, Matthew M. Willmering, and Jay A. Switzer*, *Chemistry of Materials* **2014** 26 (15), 4425-4432

PRESENTATIONS

EXPERIMENTAL NMR CONFERENCE, TALK AND POSTER

PITTSBURGH, PA; 2016

Direct Excitation and Observation of Isolated Nuclear Spin Pairs in CdTe via Optically Pumped NMR

EXPERIMENTAL NMR CONFERENCE, POSTER

ASILOMAR, CA; 2015

Optical Alignment of Spins: OPNMR Signal Dependence on Excitation Energy in GaAs QWell and Bulk CdTe

CONFERENCE ON THE PHYSICS & CHEMISTRY OF SURFACES & INTERFACES, POSTER

SALT LAKE CITY, UT; 2015

Optically Enhanced NMR Studies of Semiconductors: Optically-pumped NMR (OPNMR) of Semiconductor Quantum Wells and Bulk Direct-gap Semiconductors, GaAs and CdTe

ROCKY MOUNTAIN CONFERENCE POSTER

COPPER MOUNTAIN, CO; 2014

Optical Pumping NMR Investigations of CdTe Semiconductor

Optical Pumping of Semiconductors, Willmering, Ph.D. 2017